Exploring New Directions in Terahertz and X-ray Spectroscopy

By

I-chih Shih

A dissertation submitted in partial satisfaction of the

requirements for the degree of

Doctor of Philosophy

in

Chemistry

in the

Graduate Division

of the

University of California, Berkeley

Committee in charge:

Professor Richard J. Saykally, Chair
Professor Daniel M. Neumark
Professor David B. Graves

Spring 2013

Abstract

Exploring New Directions in Terahertz and X-ray Spectroscopy

by

I-chih Shih

Doctor of Philosophy in Chemistry

University of California, Berkeley

Professor Richard J. Saykally, Chair

The terahertz region (30-200 cm^{-1}) of the electromagnetic spectrum has historically been extremely difficult to work in due to the lack of suitable powerful light sources and limited detector sensitivity. Since the development of modern synchrotron light sources, soft X-ray spectroscopy (100-1000 eV) has no such issues regarding intensity of the light sources, but the fact that nearly all materials absorb soft X-rays has severely limited the application of spectroscopy to liquid samples in this region. In this dissertation, I describe a several new technical developments in both terahertz and X-ray spectroscopy, and their application for the study of water clusters and ion-pairing in aqueous electrolytes.

In Chapter 2, the compatibility of two new terahertz sources, Schottky diode frequency multiplier chains and quantum cascade lasers, with the Berkeley Thz spectrometer, is investigated. With the multiplier chain source, new transitions of the methane-D_2O dimer have been measured and compared with calculations. The goal of this work is to ultimately develop a more accurate potential surface for modeling of methane clathrates.

Chapter 3 presents a study of ion pairing by Near Edge X-ray Absorption Fine Structure (NEXAFS) spectroscopy and DFT calculations, starting with a comparison between ammonium chloride and ammonium sulfate solutions. A spectral fingerprint with sensitivity to the cation-anion distance and orientations is identified based on the electronic structure analysis. The resulting ion-pairing tendency is in accord with the “Law of Matching Water Affinities”. Subsequently, the counterintuitive formation of like-charge guanidinium-guanidinium contact ion pairs in water is evidenced and characterized.

The difference in escape depths of ions and electrons from condensed phase samples could ideally yield surface-bulk contrast via the total ion yield (TIY) versus total electron yield (TEY) detection of X-ray absorption spectra. To examine this potential surface sensitivity, the TIY and TEY spectra of aqueous salt solutions with different known surface affinities have been recorded and are discussed in detail in Chapter 4. Two new detection schemes, “downstream” and “upstream” detection, have been tested, aiming for the elimination of vapor signal interferences and possibly another surface-sensitive probe.

Acknowledgements

I would like first to thank my advisor, Richard Saykally, for giving me this chance to work in his research group, for his never-ending passion for science, and for the patience he has for international students — I know my bad usage of prepositions, conjunctions, articles, etc. always drives him crazy. I also want to thank David Prendergast, our theory collaborator. David led me into the world of theoretical chemistry, helped me navigate through the calculations and always had new perspectives to discuss. My gratitude to the entire Saykally group, especially the X-ray subgroup (Andrew, Alice, Greg, Jacob, Kaitlin, Alex, and Royce) for sharing the weariness during beamtime and the FIR side (Jiaxiang, Kevin, Rene, Keevin, Frank, Ralph, Nik, and Anamika), special thanks to Peter Siegel from Caltech, who was brave enough to leave his multiplier source in our lab. I would like to thank our former administrative assistant, Ethel. I always remember that after I got the signature from Rich for accepting me into the group, Ethel told me “You are not homeless anymore.” It was such a comfort for a student who was thousands of miles away from her real home.

More thanks goes to my BATS volleyball teammates, a Sunday without you guys without volleyball practices wouldn’t be called Sunday at all. Thanks for all the passes you guys gave to me (good and bad ones), every ball I set out was full of my thankfulness. Finally, thanks to my family for the unconditional love and supports. For people await me in Taiwan, Alexis and I will be back soon…!

This dissertation was supported by the Office of Basic Energy Science, Office of Science, U.S. Department of Energy (DOE) through the Lawrence Berkeley National Laboratory Chemical Sciences Division. Computational resources were provided by the National Energy Research Scientific Computing Center and the Molecular Graphics and Computation Facility (College of Chemistry, University of California, Berkeley) under NSF grant CHE-0840505.

Table of Contents

Chapter 1 : Introduction

Terahertz laser vibration-rotation-tunneling (VRT) spectroscopy is a highly sensitive (10^{-6} fractional absorption), high resolution (10^{-6}) direct absorption technique used to study intermolecular forces by directly probing the intermolecular vibrations in weakly bound complexes. Our group has mainly developed this method for the study of water clusters. The first terahertz (Thz) spectra of gaseous water clusters were measured near 22 cm^{-1} by Busarow *et al.* in 1989.[1] Following some technical developments that extended the operating range of the spectrometer to higher frequencies, Pugliano *et al.*[2] measured the first intermolecular VRT spectrum of a water cluster in 1992 near 89.5 cm^{-1}, observing a distinctive quartet pattern that results from quantum tunneling via two different hydrogen bond pathways connecting 48 degenerate minima on the 12-D intermolecular potential surface of the D_2O trimer. Subsequent work in our group produced more extensive trimer spectra and the first detailed assignment of the transitions[3], followed by the discovery of VRT spectra of the tetramer,[4] pentamer,[5] hexamer[6] and a highly detailed characterization of the dimer, as well as greatly expanded data for the other clusters.[7,8,9] However, over the past decade, disappearing commercial support for key components of our far-IR laser sideband Thz spectrometer – e.g. the Schottky barrier diode mixer, has prompted us to search new technical directions for terahertz light sources. Two emerging terahertz technologies have been explored and tested with our spectrometer, and details will be described in Chapter 2 of this dissertation. First, the applications of solid state Schottky diode frequency multiplier chains, developed by Prof. Peter Siegel at Caltech and JPL, for the study of water clusters and the water/methane dimer are described. These multiplier chains source provides convenient and stable power over a broad range of frequencies, resulting in the observation of 28 new transitions of the methane-D_2O complex near 1.4 THz. However, these sources are currently limited by a relatively low power output and a low frequency operating range. Second, a relatively new and complimentary terahertz technology — quantum cascade lasers- developed by Faist *et al.*[10] were tested to expand the frequency coverage of the Berkeley FIR spectrometer to higher frequencies.

On the other side of the electromagnetic spectrum, the development of "third generation" synchrotron radiation facilities, with improved resolution, intensity and flexibility, has attracted many scientists to investigate the details of the electronic and geometric structure of ions and molecules in condensed phase samples. Near edge x-ray absorption fine structure (NEXAFS) spectroscopy involves the promotion of a core level electron to low lying anti-bonding and continuum states.[11] It is capable of providing atom-resolved structure information and due to the diffuse character of the antibonding orbitals; NEXAFS spectra are also very sensitive to environmental effects (e.g. solvation). Because most materials strongly absorb soft (ca. 100-1000ev) X-rays, application to liquids was generally not possible until Wilson *et al.*[12] introduced Faubel's liquid microjet technology[13] into the intrinsically high vacuum soft X-ray experiment in 2001. Over the last decade, X-ray spectroscopy has become more widely accessible to liquid systems through newly developed silicon nitride liquid cells.[14,15] The advantages of such liquid cells are that it is possible to measure the liquid sample in ambient conditions and it is easy to change the sample solutions. However, the reduced flux imposed by the window or membrane attenuation and the radiation damage problems intrinsic to the use

of a near-stationary sample impose limitations on the measurements. The use of liquid microjets not only allows the convenient injection of liquid into a high vacuum environment, and windowless coupling with the x-ray beam, but also provides a continuously replenished sample, thus minimizing the severe problems of surface contamination and radiation damage. The Saykally research group has employed the combination of liquid jets with NEXAFS to study pure water[12] and its surface behavior,[16] aqueous salt solutions,[17] boron-containing energy storage systems,[18,19] the aqueous carbonate system[20] and various bio-related molecules.[21,22] Important new developments in the theoretical calculations of NEXAFS spectra are exploited via collaboration with David Prendergast of The Molecular Foundry. Using the Excited Core Hole (XCH) method developed by him and Giulia Galli[23], a DFT-based calculation using an SCF method to model the electronic structure of the lowest-energy core-level excited state with explicit inclusion of the excited electron, we have achieved new and detailed insights into the nature of a variety of aqueous systems containing boron, carbon, nitrogen, and oxygen.[18-22] The Chapter 3 of this thesis describes the novel application of NEXAFS and XCH method to the study of ion pairing in aqueous solution.

Ion pairing describes the association of charged ions in electrolyte solutions to form distinct chemical species. Ion pair formation is invoked as the most plausible explanation either of certain types of direct experimental evidence (e.g., the appearance of a new band in the vibrational spectrum) or of deviations observed at moderate concentrations from predictions of electrolyte theories that accurately describe the properties of very dilute electrolyte solutions. If the ion association is reasonably strong (roughly with an association constant, K_a, of ~1000 M^{-1} in water), there is usually little difficulty in separating the properties of the ion pair from the long-range nonspecific ion-ion interactions that exist in all electrolyte solutions. However, when the ion association is weaker, there remains a strong correlation between these non-specific ion-ion interactions (characterized in terms of activity coefficients) and ion pair formation (characterized in terms of an association constant). The development of experimental methods for studying ion pairing is a key to developing a valid general description of this concept. Historically, conductivity measurements of electrolyte solutions have provided the oldest experimental evidence for the existence of ion pairs in solution,[24] and were followed by potentiometry and measurements of electrolyte thermodynamic properties, mainly activity and osmotic coefficients.[25,26] Relaxation methods, mainly dielectric relaxation spectroscopy, have also provided valuable insights into the nature and kinetics of ion pairs.[27,28] Spectroscopic measurements (mostly UV-Vis, IR, Raman, and NMR) on electrolyte solutions have similarly played a significant role in the elucidation of ion-pairing phenomena. Such techniques typically rely on the observation of a new spectral feature corresponding to each new species formed in solution. Ideally, such features should be unique well-separated peaks, but in most cases, they may occur only as subtle modifications of the features corresponding to the ions themselves. An advantage of spectroscopic methods is that they are applicable to most solute/solvent combinations without the need for significant theoretical developments, which are very difficult for concentrated electrolyte systems.

Here, the advantage of NEXAFS to study ion pairing is that it can simultaneously probe both the localized ionic interactions and the delocalized solvation environmental changes. The investigation described in Chapter 3 started with the comparison between

ammonium chloride and ammonium sulfate solutions. The concentration dependent features in the spectra reveal stronger pairing between ammonium/chloride pair, supporting the "Law of Matching Water Affinities," proposed by K. D. Collins and relating relative hydration strength of ions to their tendencies to from contact ion pairs.[29,30] Building on the success in interpreting the spectra of the "normal" ion pairing, I have expanded my study to the interesting and electrostatics-defying pairing between guanidinium-guanidinium like-charge contact pairing. The observed concentration-induced nitrogen K-edge resonance shifts result from π^* state mixing and the release of water-water interactions as two solvated guanidinium cations associate into a stacked pair configuration. Possible biological implications of this counter-intuitive cation-cation pairing are discussed.

In the last chapter, the investigation of two new detection techniques for liquid NEXAFS spectroscopy, "downstream" and "upstream" detection, is described. The major goals sought in the exploration of these two detection schemes are to obtain spectra of high vapor pressure liquids and low dielectric liquids without incurring the complication of a high vapor spectrum background, and to explore their potential for surface-sensitive detection. The comparison of electron yield (TEY) and ion yield (TIY) detection of surface active and inactive salt solutions demonstrated the enhanced surface sensitivity of TIY over TEY measurements.

References:

[1] Busarow, K. L.; Cohen, R. C.; Blake, G. A.; Laughlin, K. B.; Lee, Y. T.; Saykally, R. J. *J. Chem. Phys.* **1989**, *90*, 3937.

[2] Pugliano, N.; Saykally, R. J. *Science* **1992**, *257*, 1937.

[3] Liu, K.; Elrod, M. J.; Loeser, J. G.; Cruzan, J. D.; Pugliano, N.; Rzepiela, J. A.; Brown, M. G.; Saykally, R. J. *Durham, U. K., Faraday Discuss.* **1994**, *97*, 35-41.

[4] Cruzan, J. D.; Braly, L. B.; Liu, K.; Brown, M. G.; Loeser, J. G.; Saykally, R. J. *Science* **1996**, *271*, 59.

[5] Liu, K.; Brown, M. G.; Cruzan, J. D.; Saykally, R. J. *Science* **1996**, *271*, 62.

[6] Liu, K.; Brown, M. G.; Carter, C.; Saykally, R. J.; Gregory, J. K.; Clary, D. C. *Nature*, **1996**, *381*, 501.

[7] Braly, L. B.; Cruzan, J. D.; Liu, K.; Fellers, R. S.; Saykally, R. J. *J. Chem. Phys.* **2000**, *112*, 10293-10313

[8] Braly, L. B.; Liu, K.; Brown, M. G.; Keutsch, F. N.; Fellers, R. S. Saykally, R. J. *J. Chem. Phys.* **2000**, *112*, 10314-10326.

[9] Viant, M. R.; Cruzan, J. D.; Lucas, D. D.; Brown, M. G.; Liu, K.; Saykally, R. J. *J. Phys. Chem A* **1997**, *101*, 9032.

[10] Faist, J.; Capasso, F.; Sivco, D. L.; Sirtori, C.; Hutchinson, A. L.; Cho, A. Y. *Science* **1994**, *264*, 553.

[11] Stöhr, J. *NEXAFS Spectroscopy*; Springer: Berlin, 1992.

[12] Wilson, K. R.; Rude, B. S.; Catalano, T.; Schaller, R. D.; Tobin, J. G.; Co, D. T.; Saykally, R. J. *J. Phys. Chem. B* **2001**, *105*, 3346-3349.

[13] Faubel, M.; Schlemmer, S.; Toennies, J. P. *Zeitschrift fur Physik D (Atoms, Molecules and Clusters)* **1988**, *10*, 269-277.

[14] Fuchs, O.; Maier, F.; Weinhardt, L.; Weigand, M.; Blum, M.; Zharnikov, M.; Denlinger,

J.; Grunze, M.; Heske, C.; Umbach, E. *Nucl. Instrum. Meth. A* **2008**, *585*, 172-177.
[15] Tokushima, T.; Harada, Y.; Takahashi, O.; Senba, Y.; Ohashi, H.; Pettersson, L. G. M.; Nilsson, A.; Shin, S. *Chem. Phys. Lett.* **2008**, *460*, 387-400.
[16] Wilson, K. R.; Rude, B. S.; Smith, J.; Cappa, C. D.; Co, D. T.; Schaller, R. D.; Larsson, M.; Catalano, T.; Saykally, R. J. *Rev. Sci. Instrum.* **2004**, *75*, 725-736.
[17] Schwartz, C. P.; Uejio, J. S.; Duffin, A. M.; Drisdell, W. S.; Smith, J. D.; Saykally, R. J. *Chem. Phys. Lett.* **2010**, *493*, 94-96.
[18] Duffin, A. M.; Schwartz, C. P.; England, A. H.; Uejio, J. S.; Prendergast, D.; Saykally, R. J. *J. Chem. Phys.* **2011**, *134*, 154503.
[19] Duffin, A. M.; England, A. H.; Schwartz, C. P.; Uejio, J. S.; Dallinger, G. C.; Shih, O.; Prendergast, D.; Saykally, R. J. *Phys, Chem. Chem. Phys.* **2011**, *13*, 17077-17083.
[20] England, A. H.; Duffin, A. M.; Schwartz, C. P.; Uejio, J. S.; Prendergast, D.; Saykally, R. J. *Chem. Phys. Letters* **2011**, *514*, 187-195.
[21] Uejio, J. S.; Schwartz, C. P.; Duffin, A. M.; England, A. H.; Prendergast, D.; Saykally, R. J. *J. Phys. Chem. B* **2010**, *114*, 4702-4709.
[22] Uejio, J. S.; Schwartz, C. P.; Saykally, R. J.; Prendergast, D. *Chem. Phys. Lett.* **2008**, *467*, 195-199.
[23] Prendergast, D.; Galli, G. *Physical Review Letters* **2006**, *96*, 215502.
[24] Arrhenius, S. Z. *Phys. Chem.* **1887**, *1*, 631.
[25] Hanna, E. M.; Pethybridge, A. D.; Prue, J. E. *Electrochim. Acta* **1971**, *16*, 677.
[26] Robinson, R. A.; Duer, W. C.; Bates, R. G. *Anal. Chem.* **1971**, *43*, 1862.
[27] Barthel, J.; Neueder, R.; Poepke, H.; Wittmann, H. *J. Solution Chem.* **1998**, *27*, 1055.
[28] Buchner, R.; Sipos, P.; Hefter, G.; May, P. M. *J. Phys. Chem. A* **2002**, *106*, 6527.
[29] Collins, K. D. *Biophys J.* **1997**, *72*, 65-76.
[30] Collins, K. D. *Methods* **2004**, *34*, 300-311.

Chapter 2 : Terahertz VRT Spectroscopy of the Methane-Water Complex

2.1 Introduction

A quantitative description of the interaction of methane with water is important for the modeling of methane clathrates, as well as for general studies of hydrophobic interactions, viz., the tendency of nonpolar molecules to form aggregates in water and the principal factor determining the conformation of nucleic acids, the formation of micelles and protein folding.[1,2,3] Methane-water is one of the simplest systems exhibiting such interactions. In nature, methane-water clathrates are non-stoichiometric mixtures of the two molecules, with water forming a cage around a methane molecule[4,5] About 6.4 trillion tones of methane are trapped in deposits of methane clathrate on the deep ocean floor, containing about twice the amount of carbon in conventional fossil fuels in world reserves. These natural gas hydrates are seen as a potentially vast energy resource, but there is no economically viable extraction method known so far.[6] Also, methane is a more efficient greenhouse gas than CO_2.[4] , and the sudden release of large amount of methane from methane clathrate has been hypothesized as a cause of past and possibly future climate changes.[7] The ultimate goal of the present study is to construct a predictive full-dimensional anisotropic intermolecular potential surface (IPS) describing the intricacies of the interaction between methane and water as well as the structural and dynamic properties of methane-water complexes. This IPS would serve as the ultimate guideline for study of new clathrate structures and would also facilitate a better modeling of the kinetics of clathrates formation and dissociation at the microscopic level.

Previous studies in the Saykally group of the prototypical system Ar-H_2O[8,9] represent the first stage of still-ongoing efforts to obtain accurate experimental potentials for describing hydrophobic interactions. Vibration-rotation-tunneling (VRT) transitions of the Ar-H_2O clusters formed in a cw planar supersonic expansion were recorded by tunable far infrared (Thz) spectroscopy. Those data were then used in a direct nonlinear least-squares fit to determine the IPS. The success with the Ar-H_2O system provides the framework to understand the spectra and dynamics of more complicated systems, like methane-water. Since the octopole is the lowest nonvanishing multipole moment in methane, only high order terms in the multipole expansion of the electrostatic interaction (octopole-dipole, hexadecapole-dipole) are present in CH_4-H_2O. So the spectra of this complex probe the importance of these higher order terms in the IPS, whereas they are usually neglected when the more typical low order terms are present. Other than the higher-order electrostatic interaction, the dispersion interaction and short range repulsion force are also notoriously hard to model from theorists' point of view.

Only two previous experimental studies of gas phase methane-water clusters have been reported. Suenram *et al*[10]measured microwave spectra of various isotopomers of the methane-water dimer. They indicated that methane acts as a proton acceptor. However, the microwave experiment probes only the average structure in one given VRT state and

does not provide direct information on the intermolecular forces in the system. Utilizing the rotational constant from that work, Dore *et al*[11] measured and assigned thirteen VRT bands from 18-35.5 cm^{-1} using terahertz laser spectroscopy. They suggested that both methane and water molecules undergo nearly free internal rotations within the dimer, and therefore the VRT energy levels of the dimer will correlate strongly with the rotational levels of each monomer.

A number of *ab initio* pair potentials that incorporate electron correlation at different levels exist for the methane-water dimer. The IPS by Harrison[12] was obtained from calculations at 95 different intermolecular geometries using the supermolecular method with the MBPT2 level treatment of the electron correlation and a small. 6-31G basis set. Another IPS was developed by Bolis *et al*.[13] These authors calculated the interaction energy at the HF level using a minimal basis. Both of the IPS predict that the global minimum occurs at the C---H-O contact. However, Woon *et al*.[14] used the MBPT2 level of theory and a larger basis set, and suggested that the minimum occurs at the C-H---O contact. These authors obtained a site-site fit involving exponential in r_{ab} and sixth and first power of $1/r_{ab}$. Later results based on lager basis sets and higher orders of powers of $1/r_{ab}$ have been introduced.[15,16]

The most direct way to test or refine a calculated IPS is to fit the parameters to experimental data. However, the spectral range from previous work samples only a very small portion of the IPS. In order to construct a full-dimensional IPS, a much wider spectral range is essential. Because of the many large amplitude motions of the water and methane molecules, the complex exhibits a rich spectrum in the terahertz region. In this chapter, some newly discovered transitions of the methane-water complexes near 2.52 THz will be discussed and compared with new spectral predictions based on the SAPT (DFT) approach by Prof. Claude Leforestier. Then follows an account of a trial of new technology for terahertz generation and its application for high-resolution spectroscopy. In collaboration with Prof. Peter Siegel from JPL, we have tested the compatibility of their frequency multiplier chain (LO source) with our system and searched of new water-methane bands. Finally, I end this chapter by describing a trial of a promising new terahertz source – a quantum cascade laser (QCL).

2.2 Experimental Methods

Berkeley Terahertz Spectrometer

A schematic of the Berkeley Terahertz Spectrometer[17,18] is shown in Figure1. The radiation of a line tunable CO_2 laser is used to pump a fixed frequency THz gas laser (output power ~ 10mW). The fixed frequency THz radiation is emitted from the rotational levels of small vibrationally excited molecular gases. Methanol is the primary gas used in this work, yielding 118 micron light. Tunable terahertz sidebands are then generated through nonlinear mixing of the THz radiation with tunable microwave radiation in a Schottky barrier diode. Microwaves are generated using the HP8367B synthesizer, providing approximately 10 mW of microwave radiation from 2-25GHz. The sidebands have frequencies of ν(laser) ± ν(microwave), which results in an effective tuning range of 2-100 GHz centered on each FIR laser with fixed-tuned millimeter wave multipliers. These sidebands are then separated from the unmixed THz radiation by the diplexer and etalon, and then directed to the sample chamber. The chamber is pumped by a high throughput Roots blower (1345 L/s) that is backed by two rotary mechanical

pumps. Inside the vacuum chamber, the sideband is multipassed through a pulsed planar supersonic expansion of methane and argon that has been bubbled thrugh water. The sidebands probe the 101.6 mm-long slit expansion, where the gaseous clusters form, along 18-22 paths leading to an effective path length of ~2m. The sidebands then exit the vacuum chamber and are directed to a liquid He cooled Ga-doped Ge photoconductor, where the absorption intensity is measured as a decrease to the sideband power. The frequency-modulated (FM) signal is first recovered by a digital lock-in amplifier at 2f (100 kHz) reference frequency and a time constant of 100 μs, then gated at the pulse repetition rate at 38 Hz and averaged using two boxcars – one for sampling the absorption peak, the other one for the baseline. The difference between the two boxcars was obtained with LabView program and displayed as a function of the microwave frequency. The detailed design and construction of the tunable FIR laser system have been described previously.[17,18]

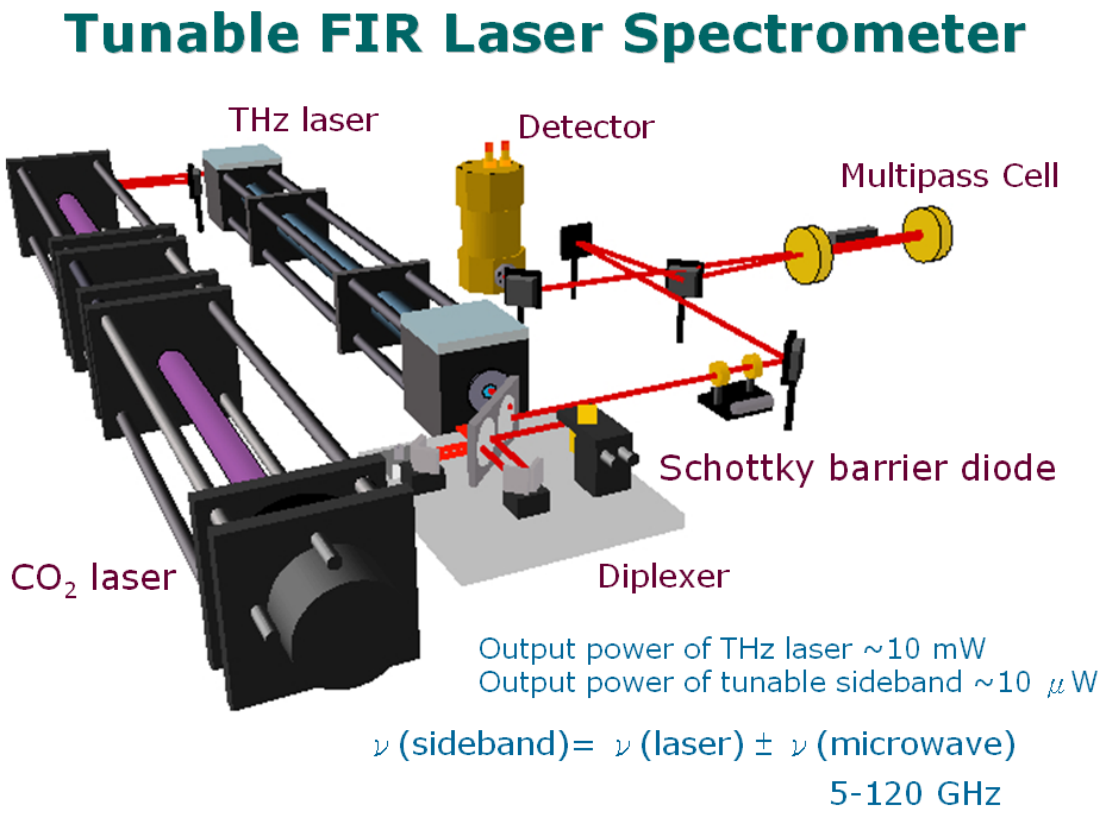

Figure 1. Schematic of the tunable terahertz laser spectrometer. The tuning range is determined by the microwave source and the use of a frequency doubler.

Specifically, the clusters of methane-water were generated by flowing 5% methane balanced with argon pre-mixed gas mixture over water. For each observed peak two background scans were performed: First, we flowed pure argon over water to make sure the peak is originated neither from Ar-water complex nor pure water clusters. Second, we expanded only the methane/Ar gas mixture without water. In this way, only spectral features requiring both methane and water have been recorded. We have scanned 48GHz

centered at the methanol 118 micron line (2522.78 GHz) and observed 39 new transitions.

At this time, we are the only group in the world carrying out terahertz spectroscopy with the use of optically pumped FIR lasers and sideband generation via point contact Schottky diode mixers. Over the past few years, the commercial technical support for these essential components of our experiment has disappeared, mainly due to the lack of users. This forces us to explore new technical directions, as described below.

New Technical Directions A: Frequency Multiplier Chain

In collaboration with Prof. Peter Siegel (Head of Electrical Engineering groups at Caltech and JPL), we have tested a high frequency multiplier/amplifier source's compatibility with our spectrometer, in the hope to replace the point-contact Schottky sideband generator. The source is a 1300-1450 GHz GaAs and GaN Schottky multiplier chain based on a x2x3x3 scheme. The original use was acting as the local oscillator for heterodyne detectors for CASIMIR on SOFIA.[19] It consists of a Millitech sextupler (13-78 GHz), a three stage power amplifier, and three multipliers (x2x3x3). The first stage doubler for this chain is built on a 30-40 micron membrane in order to get a better thermal sink for the chip heating. The second stage tripler is based on a 4-anode design. This is an improvement over the old HIFI design wherein a simpler tripler was based on 2-anodes. With a microwave input in mW range, this chain of multipliers yielded a factor of two enhancement in output power, compared with the old HIFI multipliers and a better output stability. The chain and the components used to build it are shown in Figure 2 with the output power plot. The dip at 1410 GHz is an atmospheric water feature since the measurements were done in air.[19]

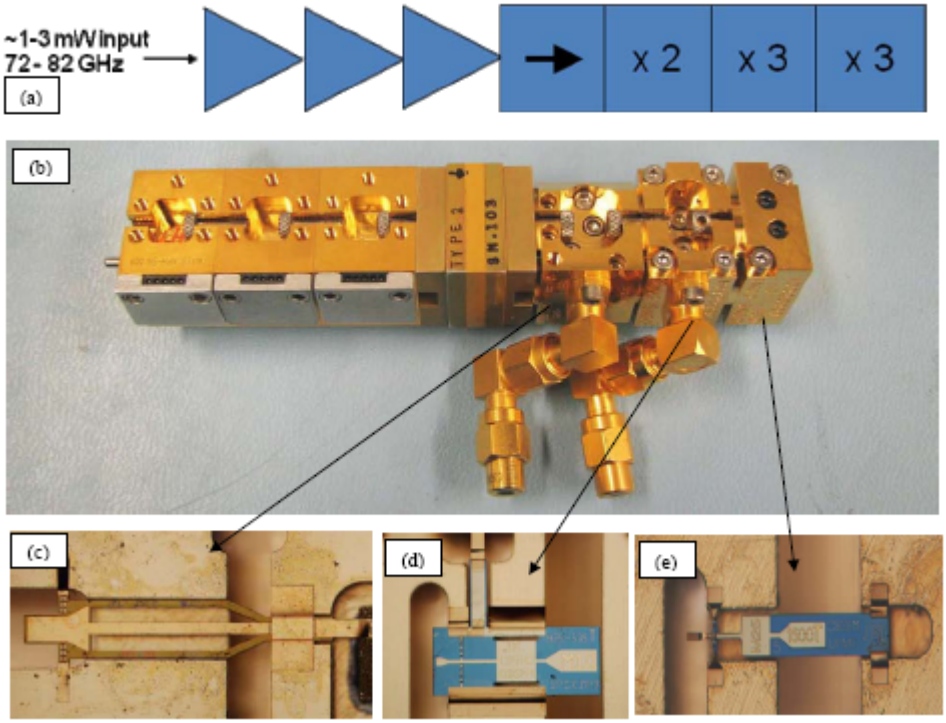

(f)

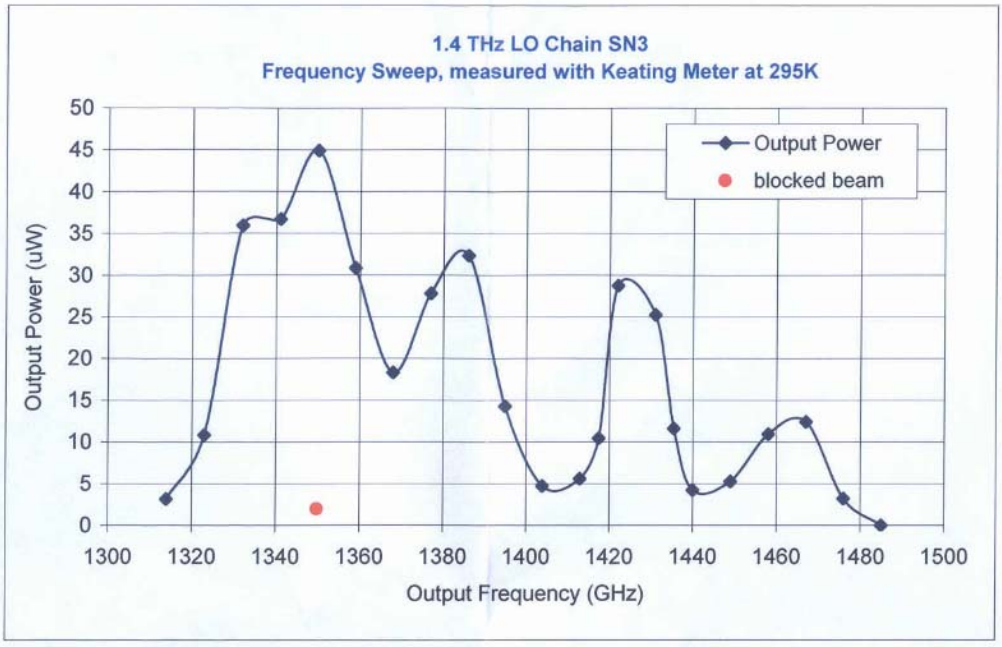

Figure 2. (a) The Caltech/JPL multiplier scheme for the 1.4 THz chain: the output from a Millitech frequency sextupler is sent into one three stage power amplifier then followed by an isolator and 3 multipliers (x2x3x3). The picture of actual chain is shown in (b). Multiplier chip M1, M2 and M3 chips are shown in (c-e). M2 utilizes multiple anodes for higher input power handling. (f) The frequency dependence on the power output from the chain; red dot shows the detector response for no beam.

The experimental setup used for this test is shown in Figure 3. The output of the multiplier chain is collimated and directed to the vacuum chamber with a double-pass configuration as a first trial, since it is difficult to collimate and focus the beam with the off-axis parabolas (OAP) only. Clusters are generated from a planar pulsed-supersonic expansion of argon or methane 5%/argon saturated with H_2O or H_2O/D_2O mixture on demand. After a double-pass through the expansion, the beam then exits the chamber and is directed onto a variable field Putley detector, where the direct absorption signal is measured used the same 2f detection scheme described above. In order to achieve better sensitivity, the new alignment scheme for larger number of passes is shown in Figure 4. The HeNe laser is aligned with OAP1 and flat mirror1 to guide the beam into the vacuum chamber as a tracing beam while the light path length between OAP1 and the entrance of multipass cell equals to the focal length of OAP1. The position of flat mirror1 also determines the number of passes in the chamber, and it was set to 14 passes. After the multipass cell, the beam is directed to the detector using flat mirror2 and OAP2. Then the source is placed on a xyz stage, in order to match the position where the HeNe beam propagates. The major problem was collimating the beam with only OAPs, and it was mitigated by incorporating two specially made Zeonor-plano convex lenses. We placed the lenses before OAPs to collimate the point source. Zeonor is a cyclo olefin polymer which has much higher terahertz transparency than polyethylene; we've also switched the window material to Zeonor to insure minimum power loss. A set of irises and a pyroelectric detector are used to trace the beam, but the signal after the multipass cell is so weak that we can only see it on the He-cooled detector.

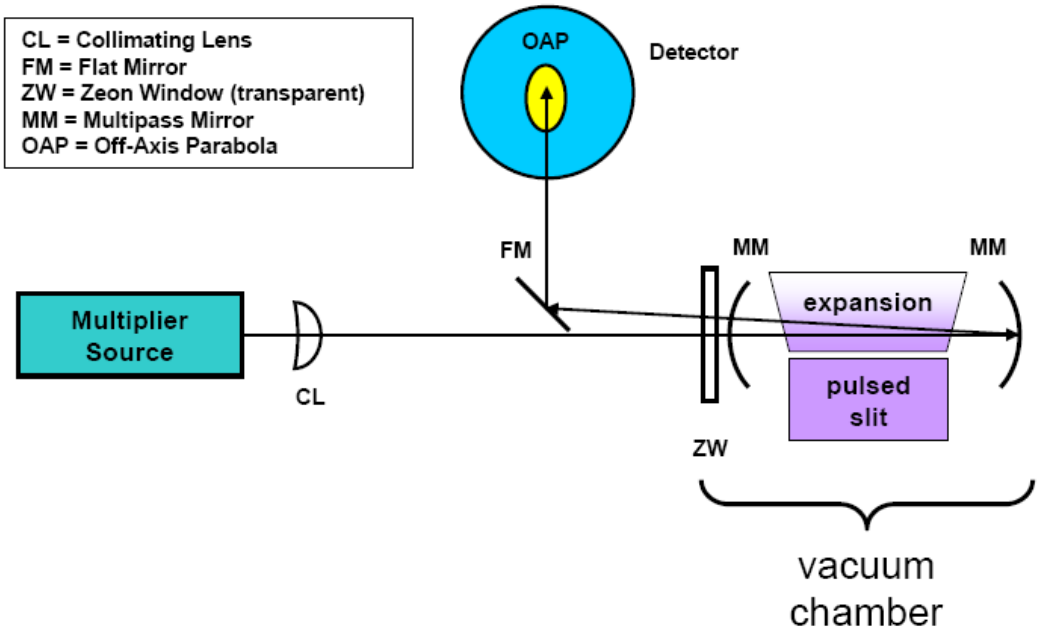

Figure 3. The initial experimental setup used to test the multiplier chain source with the Berkeley cluster spectrometer using a double pass configuration. The source is fed by an HP microwave synthesizer (12.0-13.9 GHz, the range the multiplier chips can tolerate), and outputs radiation multiplied by a factor of 108 in the frequency range 1.3-1.5 THz. Due to the limited time testing with the detector, only a double pass scheme could be achieved.

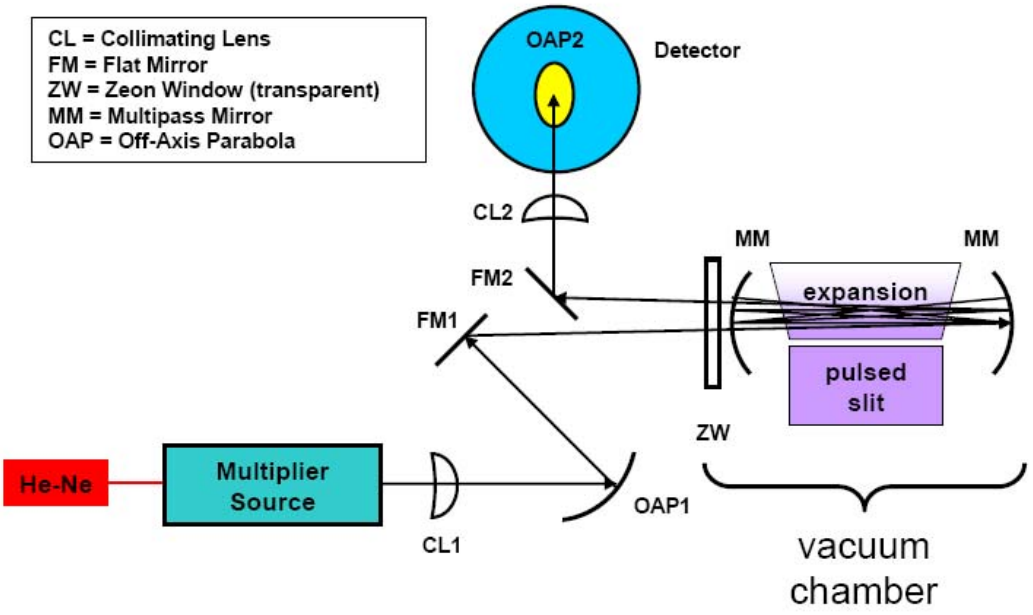

Figure 4. The "improved" experimental setup featuring the incorporation of two collimating lenses, two OAPS and a 14 passes cell.

Since the output frequency of the multiplier chain (~1.4 THz) is far lower than that of the methanol gas laser (2.52 THz) we used in the previous section, a different detector is used. There are two types of Thz detectors, those which depend upon heating effects produced by the absorbed radiation (thermal detectors) and those which make use of photoconductive effects. Typical thermal detectors like thermocouples, bolometers, Golay detectors and pyroelectric detectors are widely used over the whole IR spectrum and most of them can operate at room temperature. However, photoconductive devices have two advantages over the thermal detectors. First, their response time is much shorter, typically of the order of 1 psec rather than 1 msec. Second, since they do not respond to such a wide band of the spectrum, the limiting background noise will be smaller. Figure 5 shows three types of electronic transitions which are utilized in photoconductive devices**.** In the first one, the incident photons excite electrons from the valence band of a semiconductor into the conduction band, producing a free hole and a free electron. These will eventually recombine, but until they do so the conductivity is increased. For the excitation to occur, the photons must be greater than the intrinsic energy gap which determines the long-wave threshold of the device. From the known materials, it has not been possible to use this intrinsic effect at wavelengths longer than 10 μm. For wavelengths between 10 and 100 μm the second process shown in Figure 5 is employed. Since semiconductors may contain impurity states located in the band gap, the energy required to ionize these states must be smaller than the intrinsic energy. By making use of appropriately doped Ge, photoconductive devices have been developed for use beyond 100 μm, as shown in Figure 6. We used the un-stressed Ge:Ga photoconductor for the methanol 118um line and stressed Ge:Ga for the multiplier chain, although the spectral cover range of the chain is right on the responsivity tail. At even longer wavelengths, the third process must be used. The incident radiation is absorbed by electrons in the conduction band of a high mobility semiconductor such as InSb or Ge. Free carrier absorption occurs at room temperature but this does not lead to any change in conductivity. At helium temperature, the absorbed radiation produces a significant change in the electron distribution within the conduction band, thus changes the electron mobility. When a sufficiently large magnetic field is applied to the detector chip, the conduction band will be split into a series of sub-bands. The motion of electrons will be in orbits described with the cyclotron resonance frequency (narrow band detector). Changing the magnetic field strength will alter the cyclotron resonance frequency and will thus shift the photoconductive responsivity of the detector element. The variable field Putley (VFP) detector we used was designed for the detection in the frequency range of 10-100 cm^{-1}. The InSb chip is immersed in liquid He and placed in the magnetic field generated from a niobium-titanium superconducting solenoid. Since the magnitude of the field can be set by changing the current in the solenoid, the detection range of the instrument can be set before scanning. The responsivity profiles for various magnetic field settings are shown in Figure 7. We set the magnet to 8 KG (38.4A) for the detection on multiplier chain system at the first time, but there were some damage on the InSb chip found later so we had to switch to stressed Ge:Ga photoconductor.

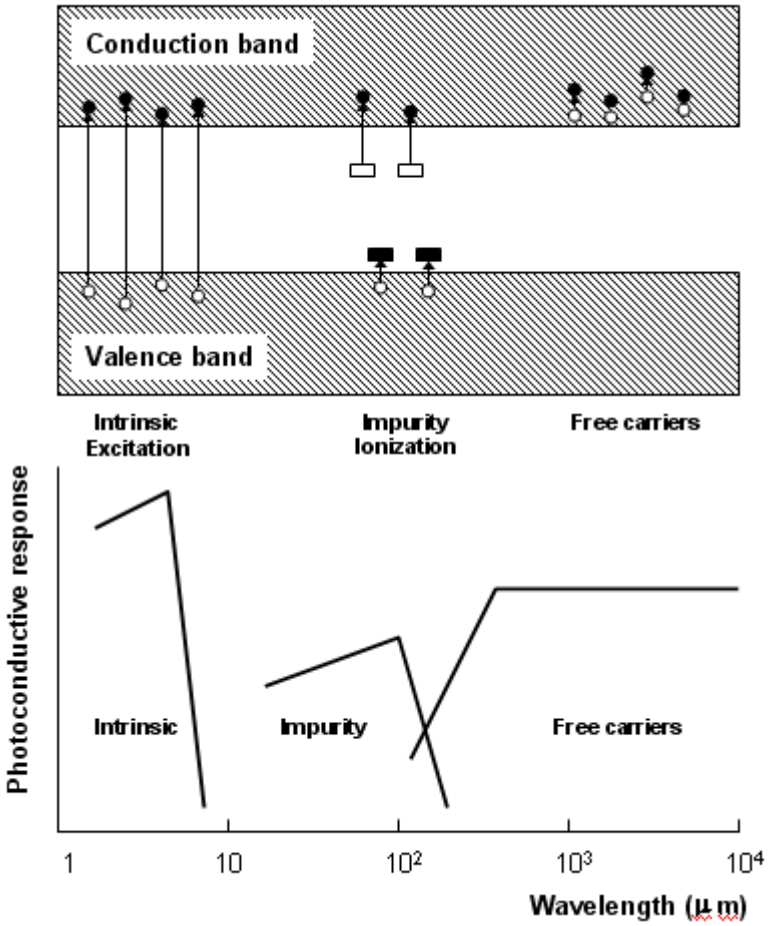

Figure 5. Illustration of the different types of photoconductive processes: intrinsic photoconductivity, extrinsic photoionization and free electron photoconductivity, showing their response dependence on the wavelength.

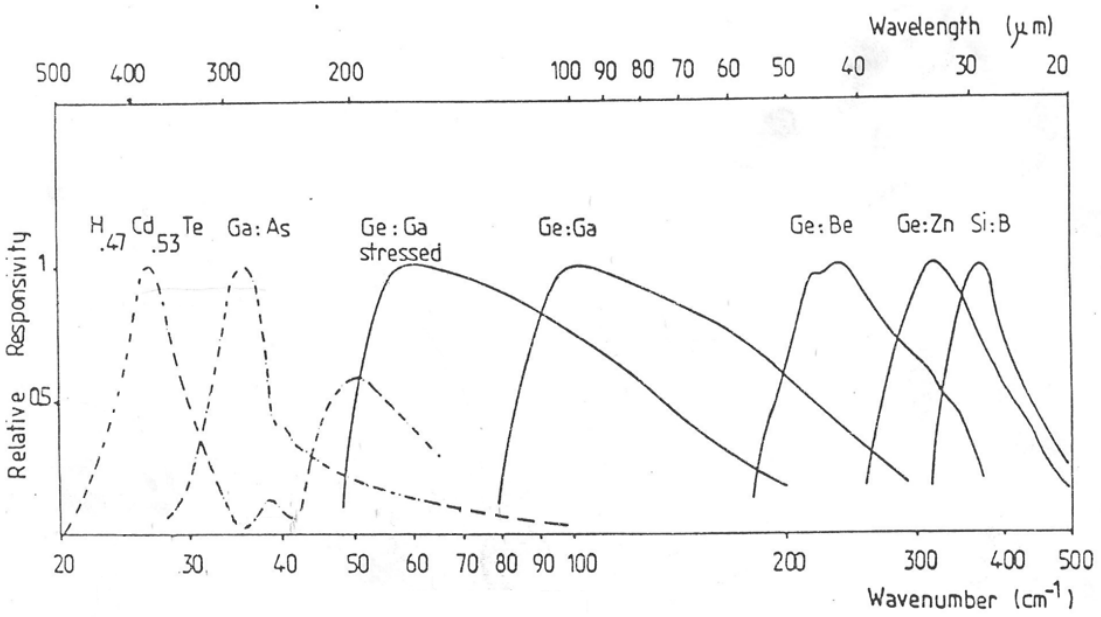

Figure 6. Spectral coverage of various types of photoconductive detectors

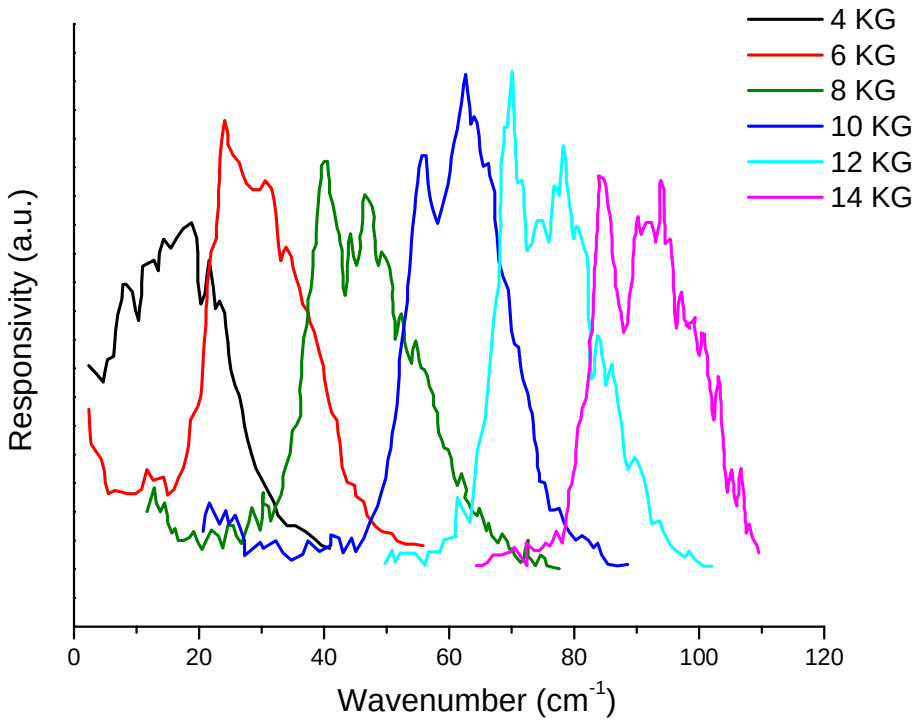

Figure 7. Spectral responsivity of variable field Putley detector on different magnetic field settings under the same liquid He temperature, 4K.

New Technical Directions B: Quantum Cascade Laser (QCL)

QCLs are semiconductor lasers that emit light in the mid and far IR. Conventional semiconductor laser diodes generate light by simple electron-hole recombination, thus the emission wavelength is determined by the band gap of the material used. But a QCL employs a periodic series of thin layers of materials, like AlInAs/GaInAs or GaAs/AlGaAs. By choice of materials, layer thickness and applied electric field, electrons in a QCL propagate through a potential energy staircase of coupled quantum wells, where the conduction band is split by quantum confinement into a number of distinct sub-bands. The lifetimes, tunneling probabilities of each level are engineered in order to obtain population inversion between two sub-bands in a series of identical repeat units. Once an electron has undergone an intersubband transition and emitted a photon in one period of the superlattice, it can tunnel into the next period of the structure where another photon can be emitted, and so on. This process of a single electron causing the emission of multiple photons as it traverses through the QCL structure gives rise to the name *cascade* and makes a quantum efficiency of greater than unity possible, which leads to higher output powers than from semiconductor laser diodes.

The first QCL was demonstrated at Bell Labs in 1994 (75 THz).[20] Since then QC lasers have become the dominant mid-infrared semiconductor laser source, with spectral coverage of 400-3300 cm^{-1}. When extended to the terahertz region, it is more difficult to operate QC lasers than in the mid-infrared for two reasons. First, because terahertz photon energies are smaller ($h\nu \sim 4-20$ meV), it is difficult to selectively inject and remove electrons, either by tunneling or scattering, from such closely spaced sub-bands so as to achieve the required population inversion. Second, the losses due to free carrier absorption increase proportionally to λ^2. There are several possible active region designs to achieve the population inversion in terahertz energy: First, coupling of several quantum wells together to create minibands, in which case, the scattering of electrons between the tightly coupled states within the minibands is favored over inter-miniband scattering. Thus, electrons tend to relax to the bottom of minibands, leaving the lower states relatively empty. Second, bringing the lower radiative state into a broad tunneling resonance with the excited state in the adjacent quantum wells. In this case, the lower radiative state maintains a strong overlap with the injector states and experiences LO-phonon scattering while the upper state remains localized. The first design scheme is called "Chirped superlattice" and the second called "Resonant-phonon", some hybrid structures of the two have been used as well.

The QCL we worked with was brought to Berkeley for a demonstration by Dr. Alan Lee, the president of LongWave Photonics LLC. The integrated QCL system contains 19 devices on one diode array. The frequency cover range for each device is shown in Figure 8; overall, this chip has a spectral coverage of 4.6 THz to 5.0 THz with averaged output power of 1mW. The chip sits on one Stirling Cycle cooler for cryogen-free operation. Figure 9 demonstrates the temperature tuning of the spectral coverage (note on the timeline that it needs about 20 minutes for the system to reach equilibrium). The temperature tuning range is 8.2 GHz from 50K to 77K, or ~300 MHz/K. Because of the temperature sensitivity of the diode band structure, frequency calibration with a gas cell is needed. The experiment setup is shown in Figure 10(a); the QCL itself is very compact, designed with a dimension of 426mm x 316mm. The diode array sits on the vacuum cold head in one user-interchangeable mount, as shown in Figure 10(b). The

back side of QCL is equipped with one compact mechanical pump for the occasional vacuum purge (10^{-3}mbar) on the cold head. The array is biased by a programmable DC power supply so no optical alignment inside the QCL system is required. The signal from the DC supply is separated by a bias-tee, one terminal connects to the lock-in amplifier and the other one to a 1:20 demultiplexer to select among the 19 different devices. The beam was focused with 1" f/1 HRSi lens and directed into the unstressed Ga-doped Ge photoconductor for the initial detector test. Then we used the same 14-pass pattern alignment through the sample cell as discussed in the previous section to do the spectroscopy.

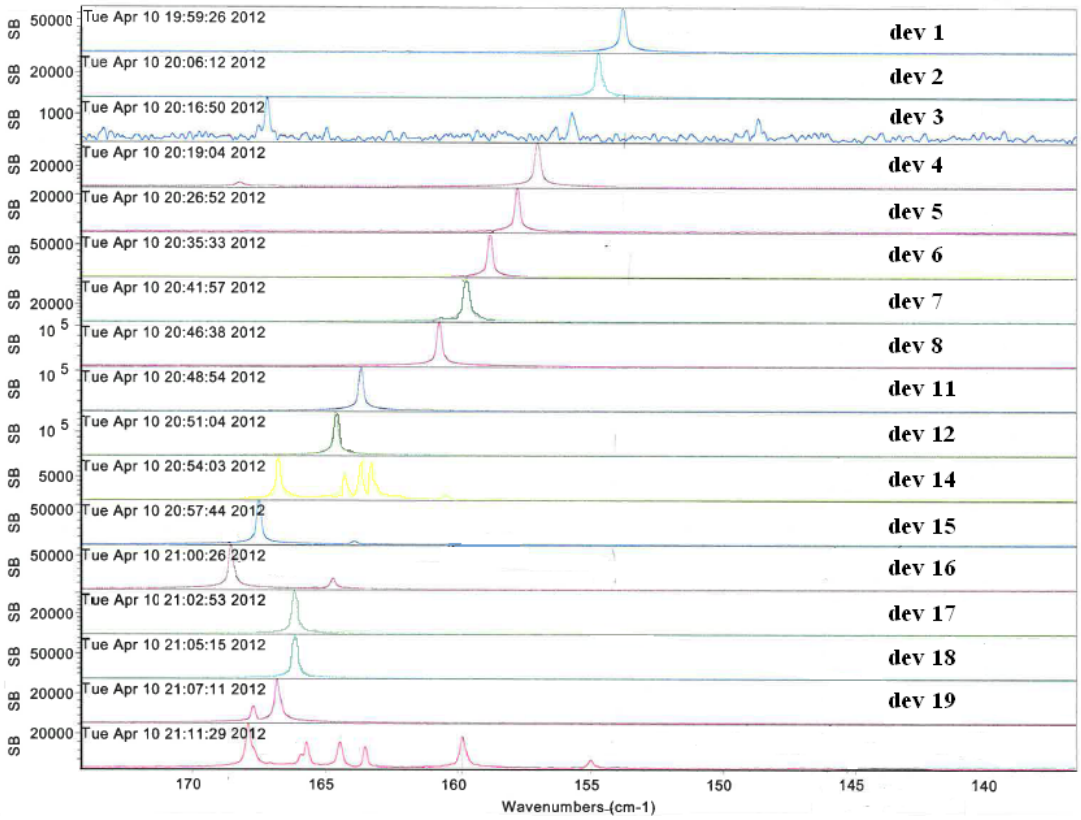

Figure 8. The spectral coverage profile of the 19 individual devices on the diode array in the quantum cascade laser, overall tuning range is 4.6 THz to 5.0 THz. Device number 6 has the strongest output.

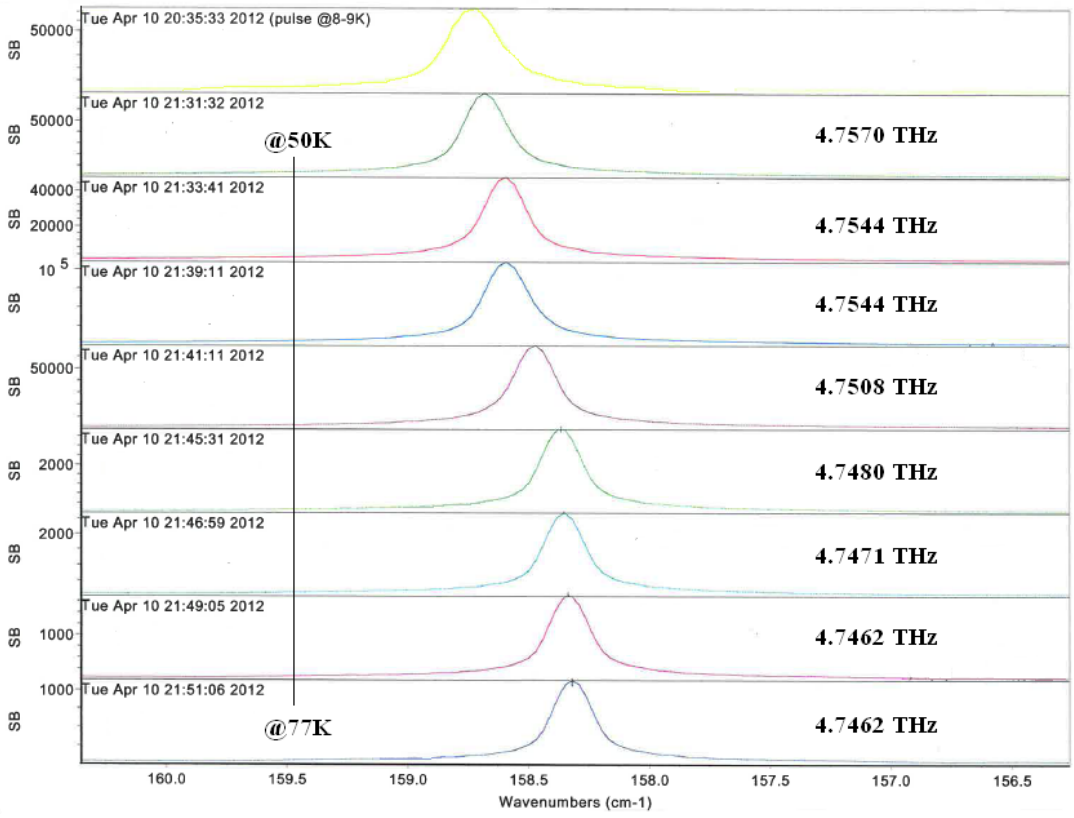

Figure 9. Temperature tuning on device number 6 in the QCL, showing the spectral drift from 50K to 77K, equal to roughly 300MHz/K

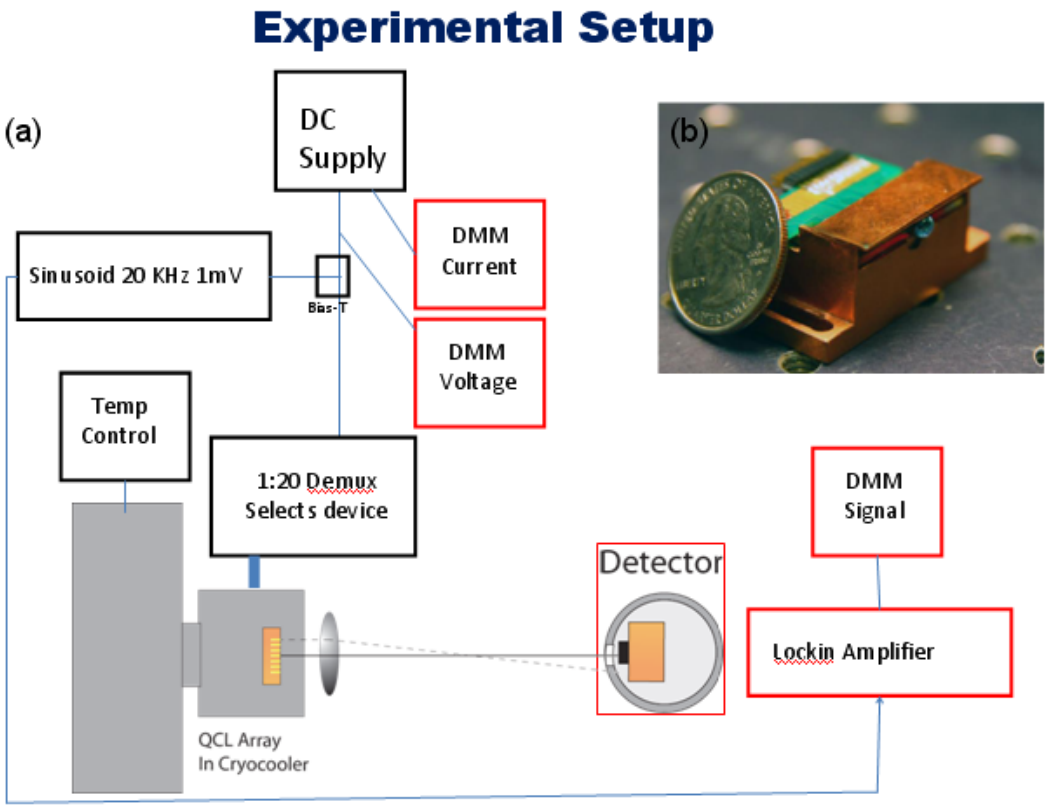

Figure 10.(a) Experimental setup for the QCL test (Inset) picture of the diode array in a user-interchangeable mount.

2.3 Calculations

A global intermolecular potential energy surface for the methane-water complex is available from *ab initio* calculations for a large numbers of geometries, combined with analytical fitting of the computed data points. The *ab initio* method used was SAPT(DFT): symmetry-adapted perturbation theory based on monomer wave functions, orbital energies, and response properties obtained from time-dependent DFT calculations.[21] This method is able to provide a reasonable initial description for this van der Waals system. Also, there exists a physically-based representation of the potential in terms of a London dispersion expansion (site-site potential). This functional form can be subsequently refined by fitting its parameters, thus refining the potential energy surface.[21,22]

If methane and water are assumed to be nearly free internal rotors within the complex, the molecular symmetry group for the cluster is the direct product of the nuclear permutation groups of the two monomers and a group formed by identity and space-fixed inversion operations. The resulting molecular symmetry group is G_{48} and its character table is given by Bunke[23], shown in Table 1. The numbers 1-4 represent CH_4 hydrogens and a-b represent H_2O hydrogens. The letters A, E, and F indicate the degeneracy of the state as well as the symmetry of the CH_4 wave functions. The superscript ± refer to the symmetric or antisymmetric property of H_2O internal rotation functions with respect to interchange of the hydrogens. Last, the subscripts 1 and 2 indicate the symmetry of the

state with respect to the parity operator. Electrically allowed transitions occur between states with the same methane and water symmetry but with opposite overall parity, because of the antisymmetric behavior of the dipole operator with respect to the space-fixed inversion. In all, the transition can only take place between A_1^+ <-> A_2^+, E^+<->E^+, F_1^+<->F_2^+, A_1^- <-> A_2^-, E^-<->E^-, and F_1^-<->F_2^-.

G_{48}	E 1	(123) 8	(14)(23) 3	(1423)(ab)* 6	(23)(ab)* 6	(ab) 1	(123)(ab) 8	(14)(23)(ab) 3	(1423)* 6	(23)* 6
A_1^+	1	1	1	1	1	1	1	1	1	1
A_2^+	1	1	1	−1	−1	1	1	1	−1	−1
E^+	2	−1	2	0	0	2	−1	2	0	0
F_1^+	3	0	−1	1	−1	3	0	−1	1	−1
F_2^+	3	0	−1	−1	1	3	0	−1	−1	1
A_1^-	1	1	1	1	1	−1	−1	−1	−1	−1
A_2^-	1	1	1	−1	−1	−1	−1	−1	1	1
E^-	2	−1	2	0	0	−2	1	−2	0	0
F_1^-	3	0	−1	1	−1	−3	0	1	−1	1
F_2^-	3	0	−1	−1	1	−3	0	1	1	−1

Table 1. Character table of G48, the molecular symmetry group of methane-water dimer.[23]

2.4 Results and Discussion

Figure 11 displays the 39 new transitions for methane-water complex observed with the "traditional" Thz sideband spectrometer using methanol as the lasing gas. The optimum Ar expansion backing pressure is 900 Torr. Although there is no clear absorption branch pattern that we can easily assign the observed spectra to, we can compare with the initial results from SAPT (DFT) (no experimental data fitting, only the transitions calculated from the *ab initio* PES). The computed J=0,1 energy levels up to 100 cm^{-1} , assuming a symmetric top structure are shown in Figure 12. The first quantum number n indicates that it is the nth energy level of the irreducible representation with these J, K values. Although K is not a good quantum number here, since the calculation scheme includes Coriolis coupling, this value corresponds to the most probable component. This preliminary results show a correct ordering of J=0, 1 transitions if compared with Fig.3 of the paper of Suenram et al. for the microwave spectrum of methane-water dimer. Figure 13 shows the predicted spectra at various expansion temperatures in the methanol 118 μm line region based on their Boltzmann probability, which includes nuclear spin weights. At 5 K, the spectrum is dominated by part of one R branch group of transitions at 2500.219, 2510.741, 2520.994, 2530.857 and 2540.271 MHz, as one can tell from the fixed gap between the transitions. There is also one weaker partial Q branch present. As the expansion temperature increases, the Q branch becomes stronger but at the same time more and more hot transitions emerge, makes the spectrum much more complicated. The high density of peaks in the experimental spectrum makes it appear like the cluster exists in a high temperature expansion. However, from the assignment of previous data of methane/water clusters or pure water clusters generated from similar expansion conditions, we knew the expansion temperature was near 4K, even lower than the

calculated spectrum with the least density of peaks. We will definitely need more transitions to be able to fit the parameters that describe the 6 dimensional *ab initio* PES (or 15 dimensional if the monomers are not rigid). Unfortunately, the key component of this experiment – Schottky barrier diode, is very fragile and has recently become commercially unavailable, thus we started to test other possible new technologies for terahertz generation and its application to high resolution spectroscopy, as described above.

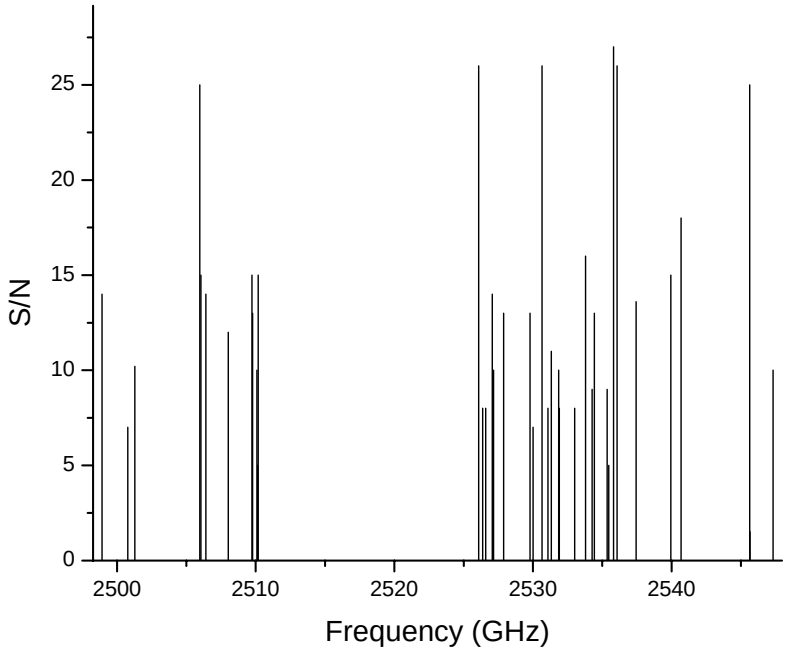

Figure 11. Stick spectrum of the 39 newly discovered VRT transitions of methane-water complexes centered at the methanol FIR laser line at 2522.78 GHz. Each transition has been tested with the control experiments which using Ar/water as the expansion gases to ensure the transition originates from the methane-water complexes but not interferences from pure water clusters or Ar-water clusters.

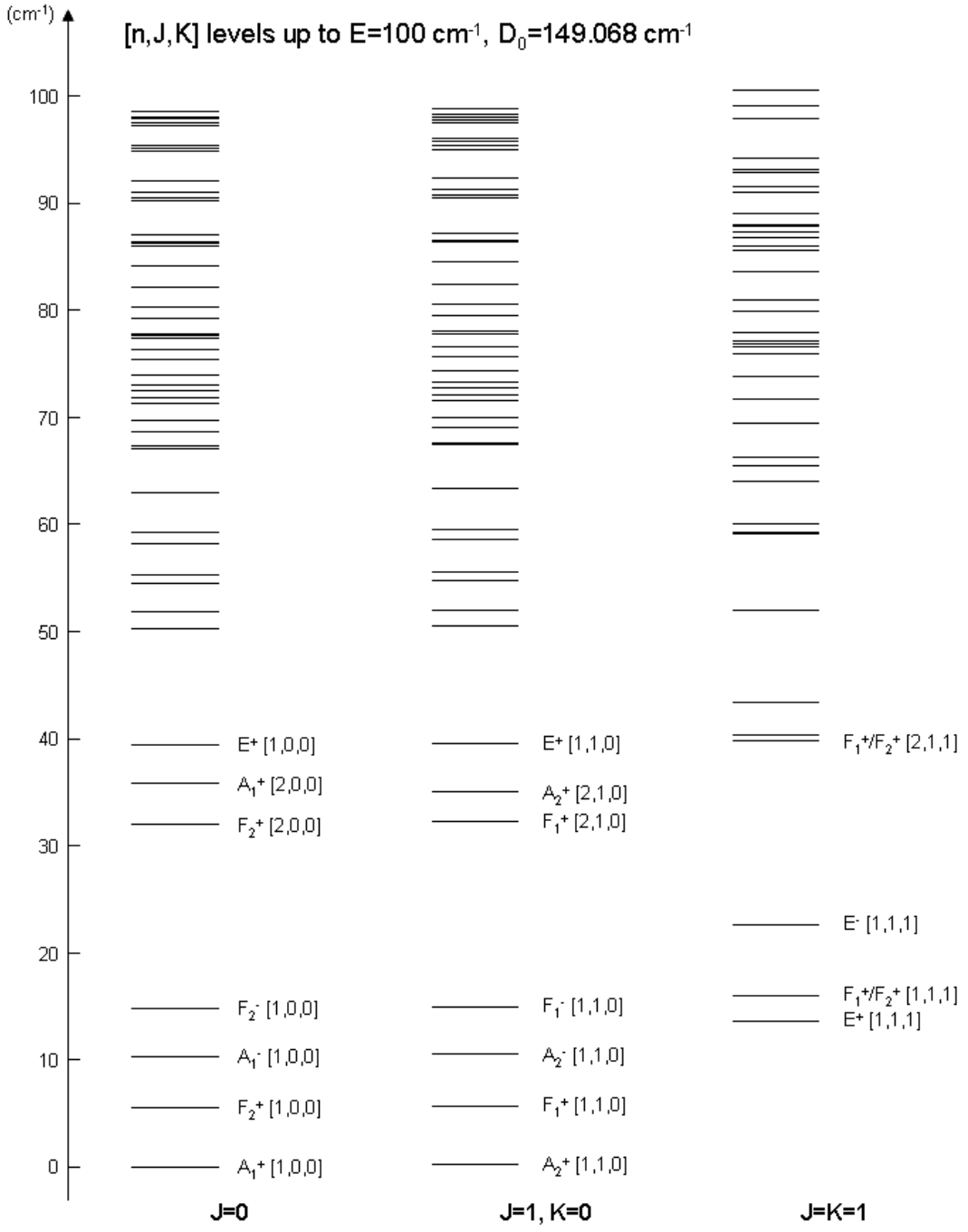

Figure 12. Calculated energy level diagram of the methane-water dimer (assuming a symmetric top structure). For simplicity, only the states lower than 40 cm^{-1} are marked with the corresponding symmetry and quantum numbers [n, J, K].[24]

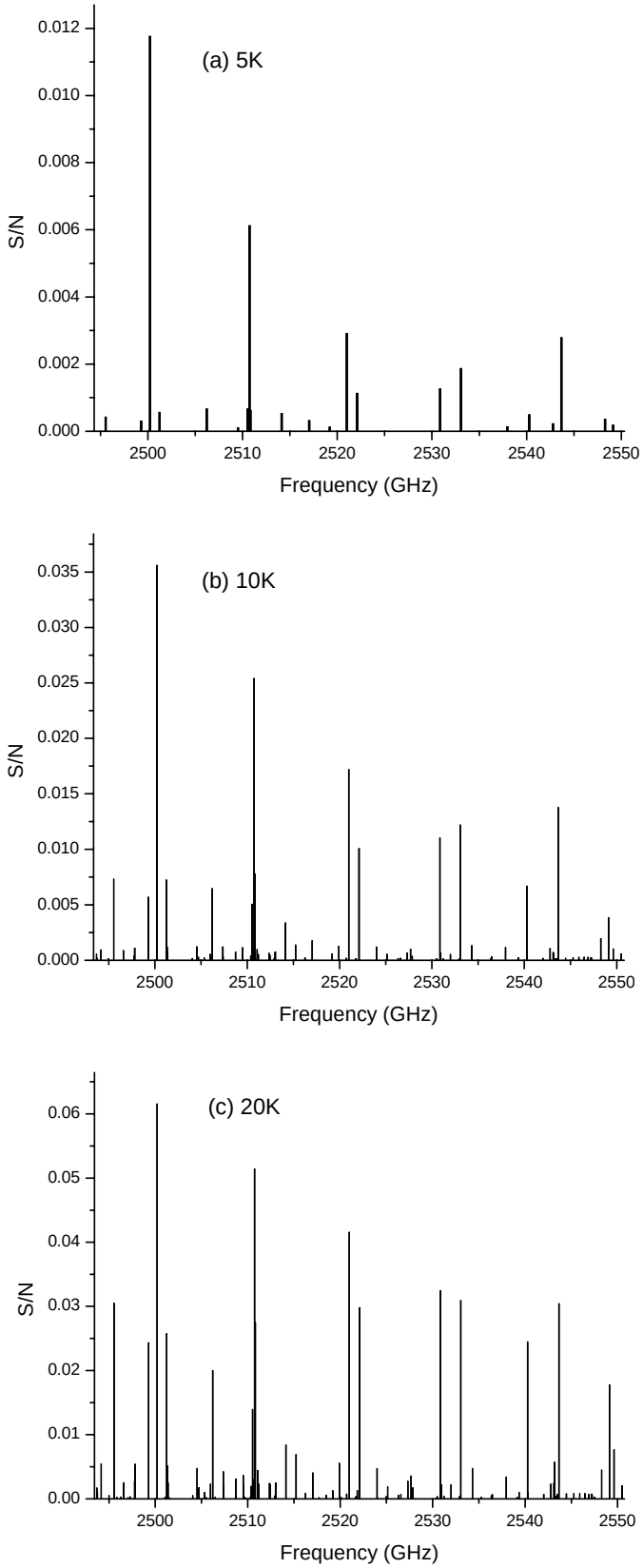

Figure 13. Calculated VRT spectra for the methane-water dimer at (a) 5K (b) 10K (c) 20K in the region of the methanol line at 2522.78 GHz

Initial results obtained for the D_2O monomer using the Caltech 1.4THz frequency multiplier chain shows rigorous 2f detection line shapes, as shown in Figure 14(a). The second target system was the H_2O/D_2O mixed trimer, which has strong transitions around 1.4THz and enabled us to test the instrumental sensitivity for cluster systems. The spectrum is shown in Figure 14(b). When compared with those obtained with the Berkeley Thz sideband spectrometer, the multiplier chain spectra reveal a lower signal-to-noise ratio and inability to resolve hydrogen tunneling splittings, which contain important structural and dynamic information. There are three reasons for those problems: First, the Berkeley sideband spectrometer used curved multi-pass mirrors to achieve 22 passes in the vacuum chamber, but the trial setup for the multiplier chain could only make 2 passes due to the large divergence of the beam. Second, the frequency increment is limited by the design of microwave generator and the multiplying factor of the source. The HP microwave generator has a minimum increment of 2 kHz, which when multiplied by 108 equals to 0.216 MHz, which is the frequency increment of the measured spectrum. Typical tunneling splittings in this range are about 0.8 MHz, i.e. there are only 4 data points to describe each set of tunneling features, so they could not resolve the splitting patterns clearly. Finally, due to the non-optimized collimating lenses used, the light-collection after the expansion was not optimized, compromising the signal/noise ratio. Figure 14(c) shows the possible detection of the pentamer Q branch peak documented previously[25] after averaging 8 scans, apparently the sensitivity needs to be improved. We've also searched for previously observed water octamer transitions but couldn't detect the peaks.

In short, in the first 3-day test of concept with Prof. Peter Siegel, we were able to successfully incorporate the JPL multiplier chain source into our FIR spectrometer and observe transitions from D_2O monomer, H_2O/D_2O mixed trimer, and even the D_2O pentamer peak if we averaged multiple scans with double-pass alignment scheme using the variable field Putley detector. Subsequently, we have designed new alignment methods and lens systems, as described in the experimental methods section.

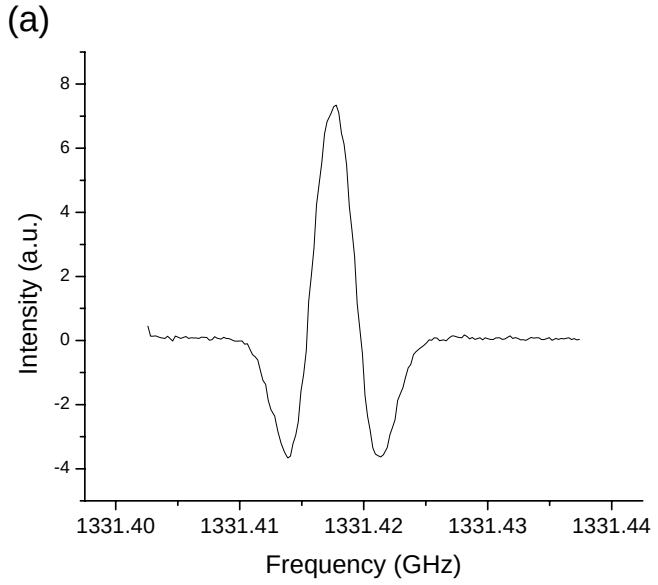

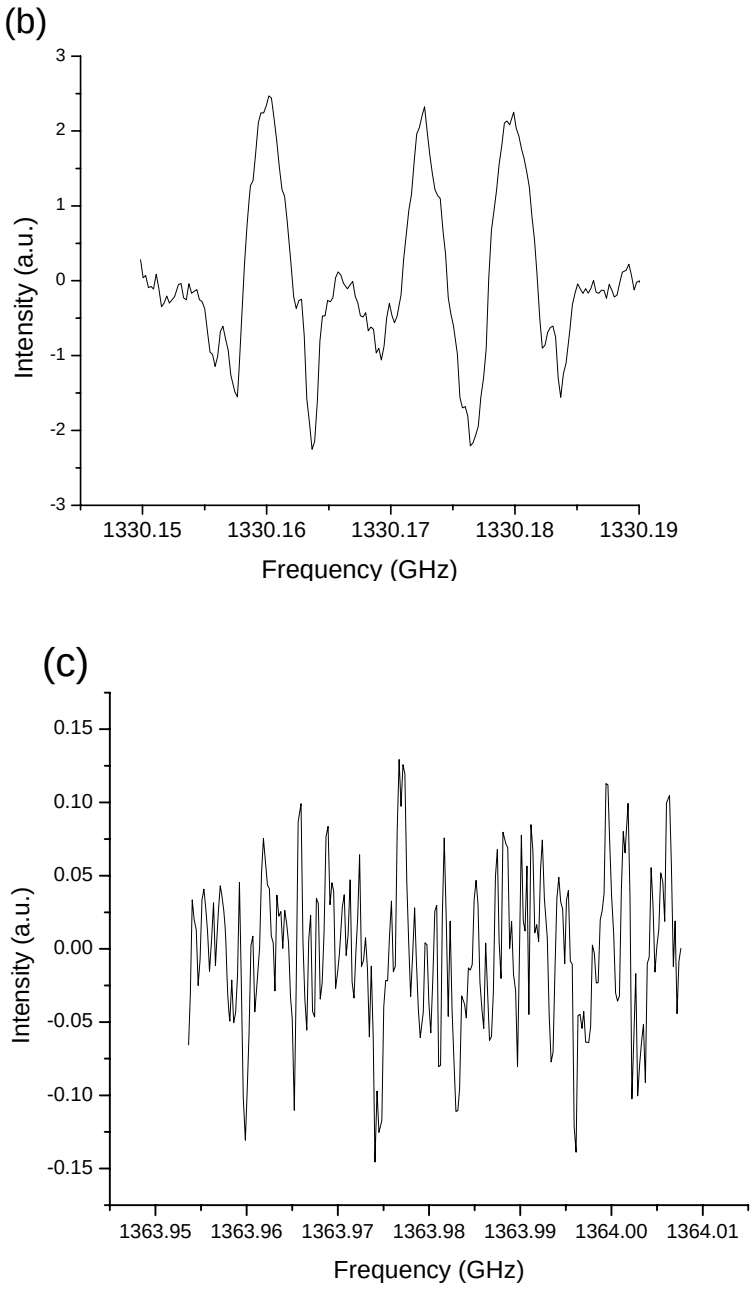

Figure 14. Terahertz spectra measured with the Caltech/JPL multiplier source for (a) D_2O monomer at 1331.412 GHz (b) H_2O/D_2O mixed trimer and (c) D_2O pentamer. The use of 2f detection yields a second-derivative lineshape.

For the second trial of the multiplier source, we successfully incorporated Zeonor lenses with OAPs to guide the source beam through the chamber with a 14 pass configuration. The important tip on the alignment is after using two irises to trace the HeNe light path, one should use a pyro-electric detector and tune on the xyz-stage where the source sits to ensure that the beam go through the irises perfectly. Then check the outgoing beam from the multipass cell using the detector. Since the output light is so

weak, it is easy to capture the reflection beam from the mirror/window instead of the real signal. One quick way to test this would be put one beam blocker inside chamber and examine if the signal vanishes or not.

Given the unfortunate VFP chip damage problem, we could only use the stressed Ge:Ga photoconductor during the second trial. The frequency region the multiplier chain can cover is right on the reponsivity tail of the Ge:Ga photoconductor (see Figrue 6) so initially we didn't expect to see strong transitions. But with the improvements in the alignment scheme and lens setup, the resulting spectrum from second trial on mixed trimer is shown in Figure 15. Compared with what we had for first trial on Figure 14(b), the bifurcation tunneling pattern is resolved clearly It turns out that the tunneling splitting for trimer is slightly larger than 1 MHz so a step size of 0.2MHz is not too big to resolve the pattern with a better S/N ratio. Thus we can declare that even with worse detector responsivity, the increase on light path and better focusing can overcome the drawbacks. During the scanning process, we found that there are artifact peaks resulting from etalon fringes occurring between multipass mirrors, as we can tell from the gap between the fake peaks that it's a 3m etalon, which is the length of the light path in a 14 pass cell. These etalons could very possibly distort or obscure weak transitions. They can be attenuated by tuning the angle of multipass mirrors and the position of the slit.

After optimization on the trimer signal, we started a search for new peaks of methane/water clusters. Since deuterated species exhibit deeper wells on the IPS, the tunneling splittings would be smaller and make the patterns easier to recognize. Considering the limited time period available with the borrowed source; we started the scan for D_2O-CH_4 complexes. We have been able to obtain VRT spectra of D_2O-CH_4 from 1.3-1.4 THz. One sample spectrum is shown in Figure 16(a), along with the blank spectrum where we expand only Ar-water but no methane gas. The FWHM is 1 MHz and no tunneling splitting has been observed, probably due to the shallower well of methane/water complex compared to water mixed trimer. Preliminary scans reveal 28 new VRT spectral lines associated with D_2O-CH_4 as shown in Figure 16(b). Although these new data don't exhibit particularly intense spectral bands, the dense band near the high energy limit (~1424 GHz) showed great promise for exploration of higher frequencies. Pursuing even higher frequencies (i.e. >2 THz) is of enormous interest in the search of spectral features associated with the D_2O-CH_4 intermolecular vdW stretching mode. This is also a major reason why we then tested the possibilities for incorporating QCL into our system.

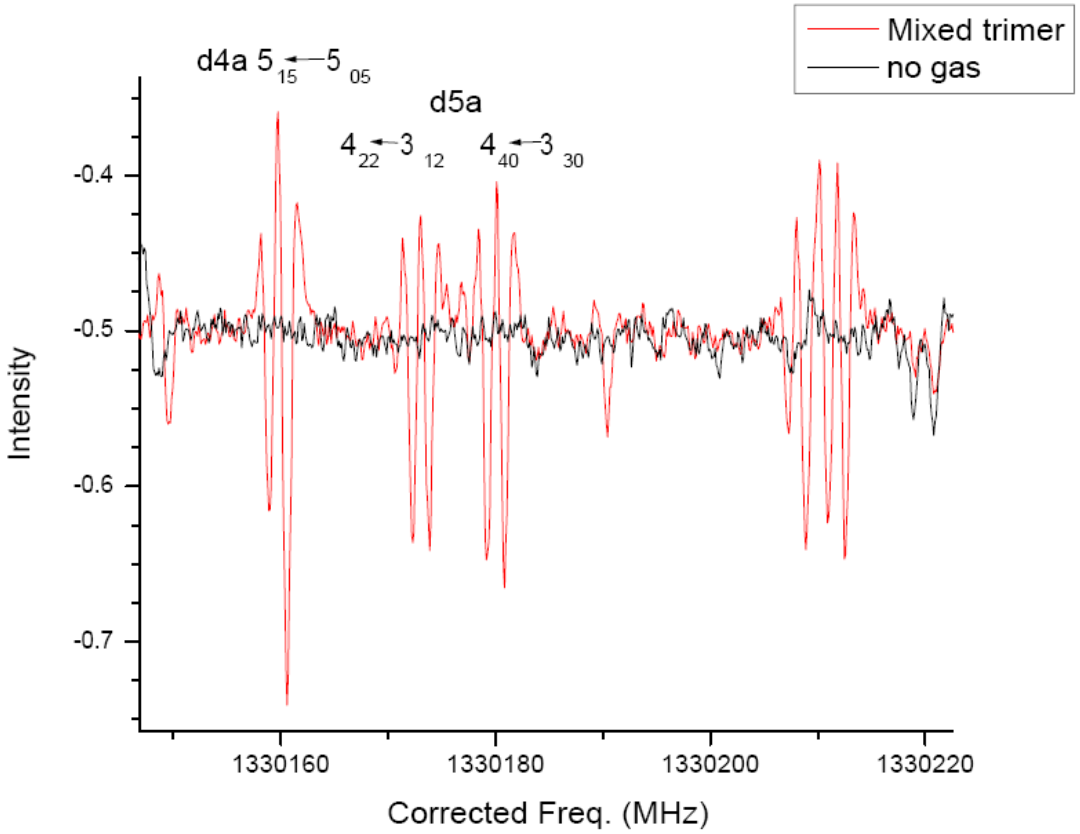

Figure 15. Spectra measured with the JPL multiplier source using the 14 pass cell configuration for the D_2O/H_2O mixed trimer

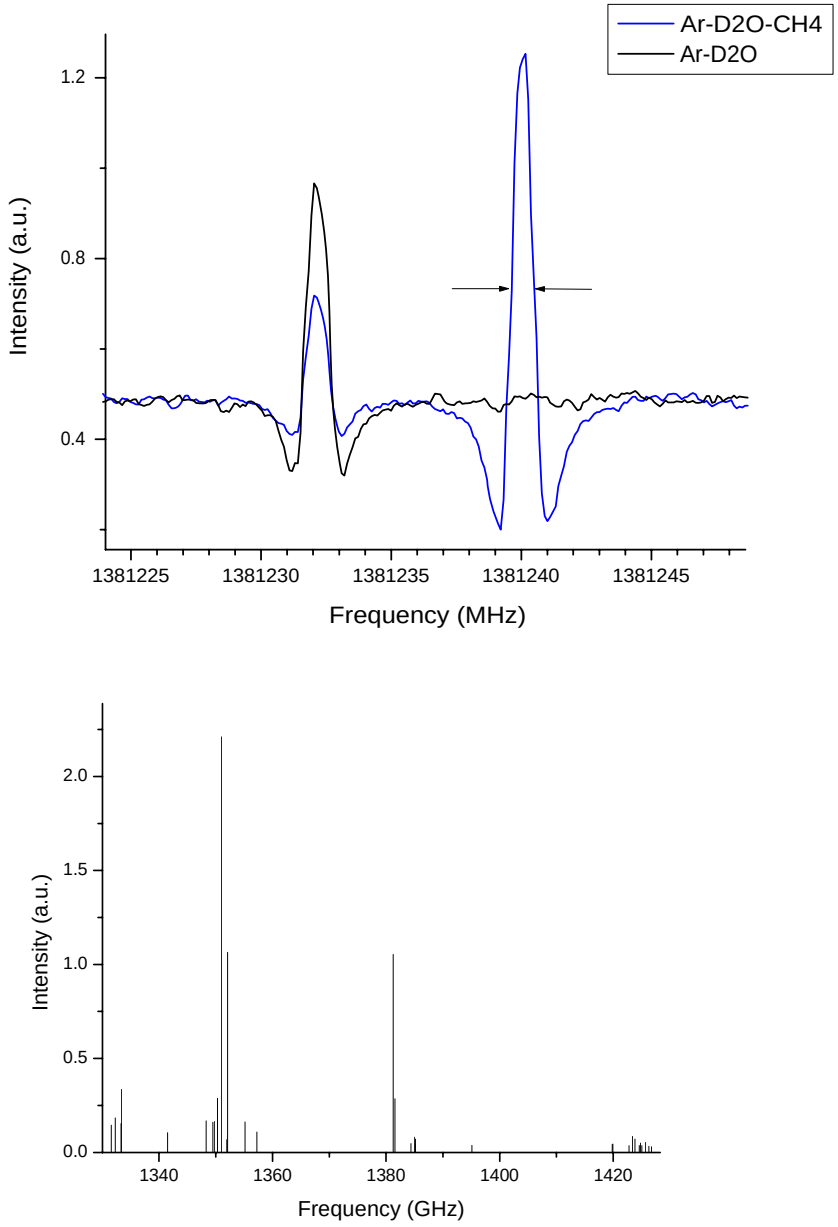

Figure 16. (a) Representative VRT spectra observed for the D_2O-CH_4 complexes compared with the blank test spectrum which no methane gas is used for the expansion (b) Stick spectrum of the 28 newly discovered transitions for D_2O-CH_4 using the 1.4 THz Caltech source

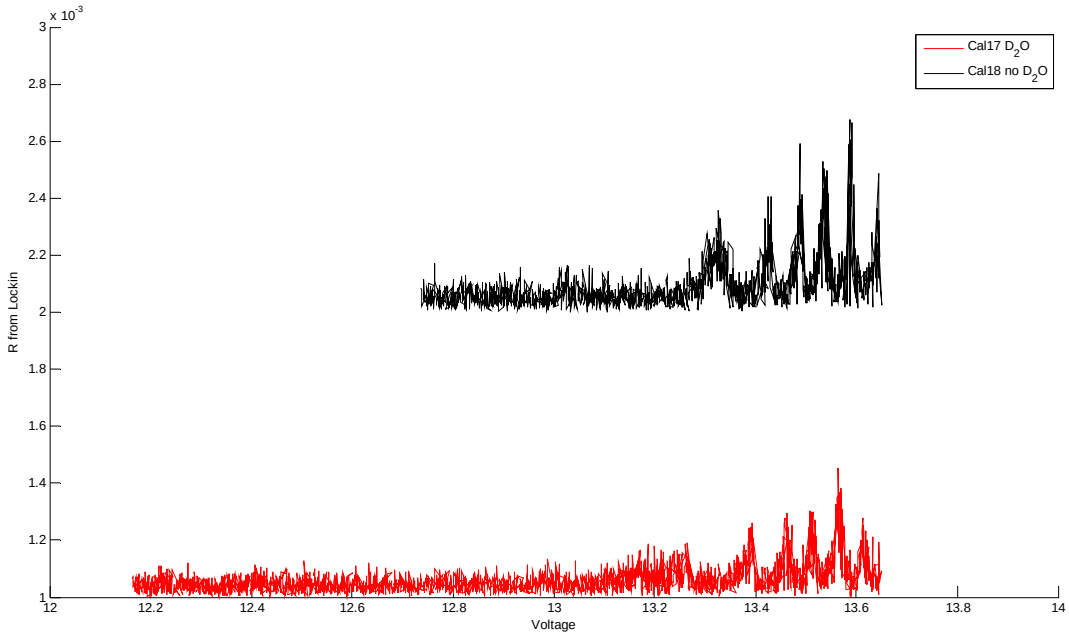

Figure 17. Spectra of pure D_2O clusters measured with the QCL system.

Figure 17 shows the spectra of D2O clusters observed with device number 6 of the QCL system and under the same 14 pass alignment scheme and detector we used for the frequency multiplier chain. X-axis is voltage but not frequency because the diode needs to be calibrated by a standard gas like methanol. The voltage tuning ratio is about 3.6 GHz/V but it is not a linear relationship; if we use this number as an estimate, the spectral range of the D_2O scan in Figure 17 (red) is 5000 MHz, which is a very long scan without the complications of tuning on the etalon positions. (We have to adjust it every 200MHz in scans using the whisker-contact Schottky barrier diode in the sideband Thz system) The instrumental resolution is 0.25 mV, or roughly 0.8 MHz, which is on the same order of the width of some of the tunneling splittings. There are strong spurious signals observed with the higher voltage biases. Those features are too wide to be real peaks, plus they show up on scans both with and without gas expansions. These might be due to the diode electronic structure design that has some instability near the frequency cutoff. Unfortunately, we didn't see a feature with the characteristic second derivative shape in this region where the QCL system has the maximum power. This can be attributed to several reasons. First of all, we are not sure about the temperature stability of the system, but we know that the diode is very sensitive to the temperature with a tuning ratio of 300MHz/K, such that even a 0.01K drift can skew the frequency by 3MHz. Hence, it is very possible that the real transitions were covered up by this drift. Second, the presence of those strong fake peaks at higher biases introduces some concerns on whether the signal we saw was mainly the reflection from the chamber window or other mirrors. Finally, the lenses we used for the multiplier chain don't work in this frequency region, so we only utilized one 1" f/1 HRSi lense after the source and one OAP in front of the detector to capture the radiation. It would be better to have one more focusing lens after the expansion.

2.5 Conclusions and Future Work

39 new transitions of the methane-H_2O complex in the 2.5 THz region were recorded via the Thz laser sideband spectrometer. However, more transitions must be measured in this frequency region in order to to resolve and assign the complicated spectral pattern. In collaboration with Prof. Claude Leforestier, the experimental data will ultimately help to determine and refine the 6-dimensional first principles potential for the methane-water dimer, as for the previously studied case of the water dimer.[26]

We successfully replaced the Thz sideband laser with the JPL multiplier chain source and obtained good signal/noise ratio increase upon the change of alignment scheme and the use of Zeonor focusing lenses. 28 new transitions of the methane-D_2O complex have been discovered near 1.4 THz. Future searches for the new band will definitely rely on having access to the JPL new solid state multiplier device. Professor Peter Siegel has two other sources on hand, at 1.9 THz and 2.4 THz., and ther higher frequency systems are under development. With the new terahertz generation technology and improvements on detector sensitivity, the remaining piece of the spectrum for this interesting cluster will hopefully be measured soon. Moving to even higher frequency, the test with 4.7 THz QCL didn't yield any cluster spectra due to alignment and reflection issues. Future work with QCLs will involve a new design to focus the beam and a more precise temperature control. On the theory side, the higher order terms in the series expansion of the methane-water potential are important, and will ultimately be required to accurately describe the forces in all six dimensions. Our high resolution Thz spectroscopic data will provide the most direct way to achieve a detailed description of such high order terms and thus the full dimensional IPS.

2.6 References

[1] Ben-Naim, A. *Hydrophobic Interactions*; Plenum: New York, 1980.

[2] Privelov, P. L.; Gill, S. I.; Murphy, K. P. *Science* **1990**, *250*, 297.

[3] Ben-Naim, A. *J. Chem. Phys.* **1989**, *90*, 7412.

[4] Sloan, Jr. E. D. *Clathrate Hydrates of Natural Gases*, 2nd ed; Marcel Dekker: New York, 1998.

[5] Sloan, Jr. E. D. *Energy Fuels* **1998**, *12*, 192.

[6] Kvenvolden, K. A. *Ann. N. Y. Acad. Sci*. **2000**, *912*, 17.

[7] Renssen, H.; Beets, C. J.; Fichefet, T.; Goosse, H.; Kroon, D. *Paleoceanography* **2004**, *19*, PA2010.

[8] Cohen, R. C.; Busarow, K. L.; Laughlin, K. B.; Blake, G. A.; Havenith, M.; Lee, Y. T.; Saykally, R. J. *J. Chem. Phys*. **1988**, *89*, 4494.

[9] Cohen, R. C.; Busarow, K. L.; Lee, Y. T.; Saykally, R. J. *J. Chem Phys*. **1990**, *92*, 169.

[10] Suenram, R. D.; Fraser, G. T.; Lovas, F. J.; Kawashima, Y. *J. Chem. Phys*. **1994**, *101*, 7230.

[11] Dore, L.; Cohen, R. C.; Schmuttenmaer, C. A.; Busarow, K. L.; Elrod, M. J.; Loeser, L. G.; Saykally, R. J. *J. Chem. Phys.* **1994**, *100*, 863.

[12] Harrison, S. W.; Swaminathan, S.; Beveridge, D. L. *Int. J. Quantum Chem.* **1978**, *14*,

319.
[13] Bolis, G.; Clementi, E.; Wertz, D. H.; Scheraga, H. A.; Tosi, C. *J. Am. Chem. Soc.* **1981**, *105*, 355.
[14] Woon, D. E.; Zeng, P.; Beck, R. R. *J. Chem. Phys.* **1990**, *93*, 7808.
[15] Szczesniak, M. M.; Chalasinski, G.; Cybulski, S. M.; Cieplak, P. *J. Chem. Phys.* **1993**, *98*, 3078.
[16] Cao, Z.; Tester, J. W.; Trout, B. L. *J. Chem Phys.* **2001**, *115*, 2550.
[17] Blake, G. A.; Laughlin, K. B.; Cohen, R. C.; Busarow, K. L.; Schmuttenmaer, C. A.; Steyert, D. W.; Saykally, R. J. *Rev. Sci. Instrum.* **1991**, *62*, 1701.
[18] Busarow, K. L.; Blake, G. A.; Laughlin, K. B.; Cohen, R. C.; Lee, Y. T.; Saykally, R. J. *J. Chem. Phys.* **1988**, *89*, 1268.
[19] Mehdi, I.; Thomas, B.; Lin, R.; Maestrini, A.; Ward, J.; Schlecht, E.; Gill, J.; Lee, C.; Chattopadhyay, G.; Maiwald, F. *Millimeter, Submilimeter and Far Infrared Detectors and Instrumentation V, Proc. of SPIE* **2010**, *7741*, 774112.
[20] Faist, J.; Capasso, F.; Sivco, D. L.; Sirtori, C.; Hutchinson, A. L.; Cho, A. Y. *Science* **1994**, *264*, 553.
[21] Szalewicz, K.; Leforestier, C.; Avoird, A.; *Chem. Phys. Lett.* **2009**, *482*, 1.
[22] Leforestier, C.; Tekin, A.; Jansen, G.; Herman, M. *J. Chem. Phys.* **2011**, *135*, 234306.
[23] Bunker, P. R. *Molecular Symmetry and Spectroscopy*; Academic, San Diego: 1979.
[24] Leforestier, C. (private communication).
[25] Harker, H. A.; Viant, M. R.; Keutsch, F. N.; Michael, E. A.; McLaughlin, R. P.; Saykally, R. J. *J. Phys. Chem. A* **2005**, *109*, 6483.
[26] Goldman, N.; Fellers, R. S.; Brown, M. G.; Braly, L. B.; Keoshian, C. J.; Leforestier, C.; Saykally, R. J. *J. Chem. Phys.* **2002**, *116*, 10148.

Chapter 3 : Investigation of Ion Pairing in Aqueous Solutions by X-ray Absorption Spectroscopy

3.1 Introduction

Hydrated ions are ubiquitous in all biological systems as essential components of intra- and extracellular fluids. The discovery of selective interactions between ions and proteins originates from Hofmeister's studies with chicken egg lysozyme, viz the amount of salt needed to "salt out" the protein depends directly on the ion identities.[1] Such ion-specific effects influence important biological phenomena like the enzymatic activity in different ionic solutions, concentration gradients across membranes, protein folding and unfolding.[2] To rationalize biological ion specificity, such as the preferential binding of sodium versus potassium with proteins, the Law of Matching Water Affinities was proposed by Collins:[3,4] The oppositely charged ions in solution spontaneously form the most stable ion pair when they have equal hydration free energies. From the electrostatic point of view, the small ions of opposite charge will tend to associate because the point charges at their centers can get closer to each other than with the point charges at water. Large ions of opposite charge act the same because the released water molecules after association can form stronger water-water interactions compared with the interactions between the large ion and water. On the contrary, kosmotropic (small) ions will not spontaneously dehydrate to form ion pair with an chaotropic ion because the point charge at the small ion can get closer to water than to the point charge at the large chaotrope. In this chapter, we begin an investigation of ion pairing in aqueous solution by examining the electronic structure and ion-pairing preferences of simple bio-related ammonium salts; we then extend our study to the origin of the counterintuitive like-charge pairing of guanidinium moieties within or between protein sub-units.

Guanidinium ($C(NH_2)_3^+$, Gdm^+) salts are widely used for denaturing protein in solutions.[5] Studies have shown that it promotes protein unfolding by interacting strongly with neutral (both hydrophobic and polar) as well as negatively charged groups.[6] Recently, like-charge ion pairing of Gdm^+, a counterintuitive analogue of ion-specific effects, has received considerable attention. Various computational methods, including ab initio,[7,8] Monte Carlo,[9] molecular dynamics (MD) simulations,[8,10,11] and quantum chemical calculations[12,13] have all indicatd the existence of contact ion pairing between Gdm^+ ions in water. However, the direct experimental detection of this ion pairing remains elusive: neutron diffraction with isotopic substitution (NDIS) experiments and MD simulations by Mason *et al.* indicated significant ion pairing for the Gdm^+ ions in a stacked geometry.[10] but subsequent investigation using broadband dielectric relaxation spectroscopy revealed only weak pairing in $Gdm_2CO_{3(aq)}$ and no signs of ion-pairing with $GdmCl_{(aq).}$[14] Recently the measurement of electrophoretic mobilities of oligoarginines indicated an affinity of Gdm^+ for the very similar charged arginine side chains,[15] indirectly implying that the like-charged Gdm^+ pair itself may be stable in water. Gdm^+

has been shown by neutron diffraction to be weakly hydrated[16] and the flat surface of the guanidinium group is large enough that its dehydration releases about two interfacial water molecules from each side to become strongly interacting bulk water. It is the same statement to explain why two chaotrope ions associate in water, but here the repulsive electrostatic force needs to be considered. Ab initio simulation conducted by Vondrasek *et al.*[8] showed the most important factor for stabilization of the Gdm^+-Gdm^+ pair in water compared with other cation pairs such as NH_4^+-NH_4^+ and Na^+-Na^+ is the reduction in electrostatic repulsion upon moving from quasi-spherical ions to ions possessing flat geometry with a very nonhomogeneous distribution of charge. The flat dendritic structure minimizes the Coulomb repulsion by assuming a staggered geometry, which optimizes the quadrupole-quadrupole interactions. Additional two factors which bring two Gdm^+ ions together are appreciable gains in cavitation (solvent exclusion) energy and dispersion interactions between the two ions upon association. Recent quantum mechanical cluster study[12] showed the Gdm^+-Gdm^+ pair with 12 water molecules represents a weakly stable (0.91 kcal/mol) minimal structure, while in an aqueous bulk continuum, this ion pair was calculated to be stabilized by 2.10 kcal/mol.[8]

In this chapter, we investigate the electronic structure of electrolyte solutions using X-ray absorption spectroscopy (XAS) of liquid microjets.[17] Since the unoccupied orbitals probed in the experiment extend beyond the Gdm^+ ion itself, the XAS spectrum is generally sensitive to the changes in the local solvation environment, including potential effect of ion-pairing. Similar experiments conducted for NaCl solutions by Aziz *et al.* using a liquid cell produced XAS spectra at the Na K edge for NaCl solutions as a function of concentration and revealed spectral fingerprints of Na^+-Cl^-contact ion pairs.[18] Later studies by Uejio *et al.* evidenced selective interactions of alkali cations with the carboxylate groups at the Carbon K edge.[19] Since the chemical information that can be extracted from such experimental data alone is limited, here we interpret our experimental nitrogen K edge spectra with a combination of molecular dynamics simulations and a first principles density functional theory method.[20]

3.2 Experimental Methods

NEXAFS Spectroscopy

Near Edge X-ray Absorption Fine Structure (NEXAFS) spectroscopy is an atom specific probe ideally suited for studies of the local electronic structure of disordered media. The 1s electron of selected atoms can be excited into unoccupied molecular orbitals, Rydberg states, or the continuum. The LUMO is usually centered on the molecule being excited and thus provides information about conformational change and ionic interactions in the system. For higher unoccupied states which have large spatial extents, the resonance energy and oscillating strength are very sensitive to the surrounding environment or hydrogen-bonding networks if in aqueous solutions. Typical elements probed in the soft x-ray region are boron (1s electron binding energy ~188 eV), carbon (~285 eV), nitrogen (~400 eV), and oxygen (~535eV).

Processes involved in NEXAFS are shown in Figure 1. When the system absorbs an x-ray of sufficient energy it will results in a photoelectron and a core hole. The hole is filled by an electron from a higher shell, either radiatively by emission of a fluorescent

photon, or nonradiatively by emission of an Auger electron. Figure 1 suggests that the most direct method to measure the X-ray absorption cross section is to monitor the intensity of the photoelectrons which constitute the primary excitation channel. However, to do so all structure below the ionization potential corresponding to bound state excitations would be disappeared since only free photoelectrons are measured in photoemission. This leads to the measurement of Auger electrons or fluorescent photons associated with the secondary processes of core-hole annihilation. For the K-shell excitation of low-Z atoms and for the L-shell excitations of all atoms with Z<90 the Auger decay is faster and hence dominates. When in condensed phases, the inelastically scattering of the primary photoelectrons and Auger electrons creates an electron cascade. Although the penetration depth of 532 eV photons is ~ 5 microns, the secondary electrons can only escape from an average depth of 20 Å, determined by the average kinetic energy. Since Auger electrons are produced directly via the decay of the core hole, they have much higher kinetic energies than the average secondary electron. One can measure the Auger electron yield (AEY) NEXAFS spectrum by applying a suitable high pass filter. In this chapter we used total electron yield (TEY) detection scheme to probe the bulk properties with higher current reading compared to AEY. Detailed discussion on different escaping length of electrons, ions, neutrals, fluorescent photons and their impact on surface sensitivity detection will be covered in next chapter.

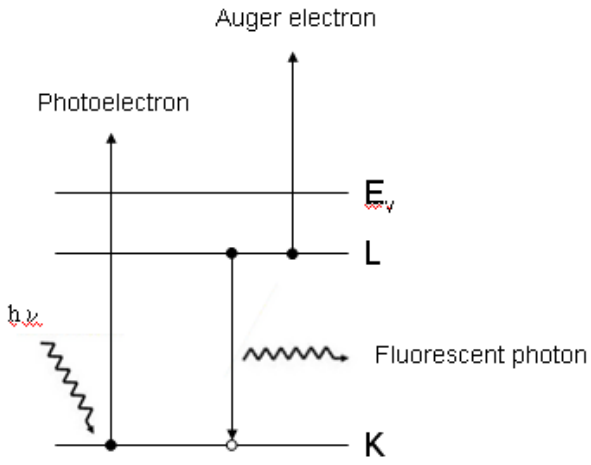

Figure 1. Excitation and relaxation processes in X-ray absorption spectroscopy: absorption of an incident x-ray causes a core electron to be ejected from the atom. The core hole is then filled by an electron in a higher orbital, results in either the emission of a fluorescent photon or an Auger electron.

Experimental Details

Ammonium chloride, ammonium sulfate and guanidine hydrochloride with a purity >99% was purchased from Sigma-Aldrich and used without further purification. Various concentrated solutions were prepared with Millipore water, which has a resistivity of 18 MΩ/cm. Nitrogen K-edge total electron yield spectra were measured at Beamline 8.0.1 at

the Advanced Light Source at Lawrence Berkeley National Laboratory. The undulator at Beamline 8 generates intense beam with a maximum flux of 6×10^{15} photons/second and a resolving power of 6000 E/ΔE. Nitrogen K-edge was accessed by using the first harmonic of the middle energy grating (220-700 eV). The entrance and exit slit widths were set at 50 microns achieving a resolution of about 0.1 eV. The spot size of the beam is 100 (horizontal) × 50 (vertical) μm, aligned onto a 30 μm continuous liquid jet. The soft x-rays intersect the liquid just as it emerges from the tip, yielding room temperature absorption spectra. The jet itself is produced using a syringe pump (Teledyne-ISCO) to pressurize the liquid behind a fused silica cylindrical nozzle (30 micron ID × 375 micron OD). Under constant flow rate operating condition, the backing pressure is around 80 atm with 0.8 mL/min flow rate. There are two major advantages of using a liquid jet. First, the continuous flowing jet prevents the sample contamination and the radiation damage from the incident X-ray beam. Second, the small surface area and high velocity of the jet in combination with the differential pumping sections make the chamber pressure low enough so that the jet can be windowlessly coupled to the X-ray beam, no need to use a flux-reducing window or Si_3N_4 membrane.

Figure 2 shows a diagram of the experimental setup, the liquid jet feedthrough on the xyz stage allows us to selectively measure the gas phase signal or liquid signal by tuning on the position. A positive biased (2.1 kV) copper electrode is used to collect both primary and secondary electrons. The jet subsequently enters a skimmer and condenses on a cryogenic trap. With the turbo pump (Turbotronik NT-20) and one more liquid nitrogen trap placed besides the jet the main chamber pressure is maintained at ~1.5×10^{-4} torr. It is sufficiently low to allow for sensitive charged particle detection. In order to couple to the upper stream beamline where the pressure is kept at 10^{-9}-10-^{10} torr we use a differential pumping section with three small turbo pumps (Varian Turbo V-70). One pressure-sensitive shutter is placed in between the chamber and the differential pumping section to protect beamline from any pressure backflow.

The XAS spectra were collected with a photon energy increment of 0.2 eV. The current measured from the copper electrode was amplified, convert to a voltage, and then send to a voltage to frequency converter (+/- 10 VDC). Spectra are normalized to the signal from a high transmission gold grid located 2m upstream from the chamber. Note that at carbon K-edge, this normalization can be problematic since the incoming x-ray beam is significantly attenuated due to residual hydrocarbon deposit of the x-ray optics. The x-ray energy was calibrated to the energy of 1s→ π* resonance of residual nitrogen gas present in the off-jet scan. This vapor signal was then subtracted from the normalized on-jet scan as background subtraction. Multiple spectra for each sample were averaged. The resulting spectra were finally peak normalized in order to compare the spectra of solutions with different concentrations. (Details in Results and Discussion)

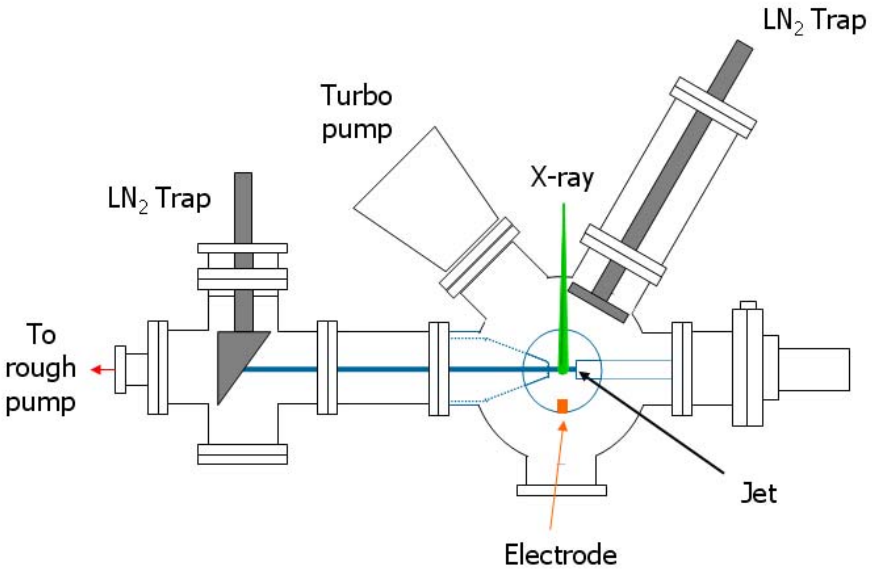

Figure 2. Schematic diagram of the liquid jet NEXAFS endstation. A liquid microjet is introduced to the vacuum at Beamline 8.0.1 of the Advanced Light Source. The tunable x-ray beam intersects the liquid sample and the electrons results from X-ray absorption and relaxation processes are detected by TEY with a biased copper electrode.

3.3 Calculations

X-ray induced core level excitations are very fast compared to nuclear motion, so the experimental spectra essentially probe molecules in frozen structural configurations, thermodynamically sampled from the vibrational degrees of freedom and solvent structure. To accurately simulate the experimental spectra, transition energies and intensities from multiple molecular dynamics snapshots need to be calculated and averaged.[21,22] For GdmCl solutions, Amber 11 was used to perform classical MD simulations, starting with a neutral periodic cubic system containing 10 GdmCl in ionic form and 272 TIP3P water molecules, equivalent to a 1.8M GdmCl solution. The simulations employed the default ff99SB force field with atomic partial charges assigned symmetrically (C 0.64, N -0.80, H 0.46). After initial energy minimization, the system was heated to 300K and then equilibrated for 100ps to a final density under constant pressure condition. A constant volume simulation was then run for 4ns, with the molecular configuration collected every 1ps. Note that there is a special atom type for the carbon on Gdm^+ ion called "cz" in the general AMBER force field (GAFF). It will modify the force field parameters such as force constant for the bond, harmonic force constants for the angle and dihedral angle barrier height. The most crucial number affecting the ion-pairing behavior between Gdm^+ ions is the dihedral angle barrier of dihedral angle (N-C-N-H) since it determines how rigid the Gdm^+ plane is. We use the same number of the torsional barrier height of N-C2(sp2 carbon)-N-H, 4.75 kcal/mol. A lower number can't keep the planarity of Gdm^+ and shows no sign of pairing in between

Gdm^+ ions. The solutions of ammonium salts are modeled through the same procedure with different concentrations.

Using atomic positions from the snapshots, X-ray absorption spectra were calculated with the XCH density functional theory approach. PWSCF, a part of the Quantum-ESPRESSO package, is used to calculate the electronic structure.[23] We use the Perdew-Burke-Ernzehof (PBE) form of the generalized gradient approximation to the exchange-correlation potential.[24] A plane wave basis set with periodic boundary conditions was employed to accurately model both localized and delocalized states. The lowest energy core-hole excited state is modeled by inclusion of the core hole and the excited electron (XCH) through the use of a suitably modified pseudopotential. The resulting self-consistent field was used to generate higher excited states non-self consistently. Transition amplitudes for the calculated spectra were calculated within the single particle and dipole approximations. All calculated transitions are numerically broadened by Gaussian convolution of 0.2 eV full width at half maximum. The energy axis is aligned using an atomic alignment scheme introduced previously,[25] designed for comparison between chemically different systems. Only the computed spectrum of isolated nitrogen was aligned to the experimental gas-phase data and all other simulated spectra were aligned relative to that. No empirical alignment was needed.

Isosurfaces of electronic states were calculated with Quantum-ESPRESSO and compared with the results from maximum overlap method (MOM) developed by Gilbert *et al.*[26,27] The MOM has been implemented within the Q-Chem 4.0 package.[28] It works by modifying the orbital selection step in the SCF procedure. By choosing orbitals that most resemble those from the previous cycle, rather than those with the lowest eignvalues, excited SCF determinants can be obtained, and this prevents variational collapse to the ground state. The success of MOM relies on the quality of the initial guess for the calculation. If the virtual orbitals are of poor quality then the calculation may relax to a lower energy state of the same symmetry. Often the calculation starts with the ground state orbitals. However, for core excitations from the core orbitals that are not symmetrically unique (Gdm^+ N 1s orbitals), using the ground state orbitals will result in a core excited state with a delocalized core hole. In order to obtain a localized core hole, the symmetry of the wave function needs to be broken. We use the orbitals from the isoelectronic ion in which the nuclear charge of the atom where the local core hole localized is increased to Z+1 (N→O). Also, because excited state electron densities can be much more diffuse than their ground state analogues, it is important to use basis sets with added diffuse functions. A 6-311(2+,2+)G(d,p) basis set, derived from the 6-331G(d,p) basis set with additional sets of polarization and diffuse functions, is used here. A quadrature grid that is large enough to integrate all diffuse densities is also necessary. All the DFT results in the following sections have employed the large EML-(100,194) grid for calculating exchange-correlation component of the energy with an unrestricted HF formalism and various exchange-correlation functionals.

3.4 Results and Discussion

Ammonium Chloride and Ammonium Sulfate

Nitrogen K-edge core level spectra of ammonium chloride at concentrations from

0.2M to 3M are shown in Figure 3. All spectra are normalized to the same peak height at 405.6 eV instead of using area normalization because a reference intensity point is necessary in order to compare the spectra of various concentrations. The spectra show a broad and strong resonance at 405.6 eV with a small pre-edge feature at 403.6 eV and a shoulder at 409 eV. The shoulder resonance exhibits a clear increase in the intensity with increasing concentration, revealing some electronic structure changes along with the variation of concentration. To help rationalize this change, the potential of mean force (PMF) can be calculated from the MD trajectory of the 0.5 M ammonium chloride solution using

$$W(r) = -k_B T \ln g(r), \quad (1)$$

where k_B is the Boltzmann constant, T is the temperature, and $g(r)$ is the radial distribution function obtained from MD calculations. Figure 4 shows the PMF along the axis joining the ammonium nitrogen and chloride. The first minimum at 3.28Å indicates the presence of a contact ion pair (CIP) (ion diameter matches with the distance) and the second minimum of a shallower well at 5.50 Å represents a more weakly bound solvent shared ion pair (SIP). Compared with the infinite distance limit between ammonium and Cl^-, the CIP is stabilized by 1.55 kcal/mol, compared to 0.42 kcal/mol for the SIP. Since the population distribution between the two species will depend on the starting configuration of the MD simulation, it's difficult to track the spectral features of different species if we sample the whole trajectory of the real solution randomly. Therefore, by fixing the distance between ammonium and chloride in AMBER we sample a hundred snapshots of each ion pair species for XAS calculation. The calculated spectra for both the CIP and SIP are plotted in Figure 5. Although the differences are subtle, there is a small pre-edge feature at 403.9 eV for the CIP, while this is not obvious for the SIP. Also the CIP spectrum exhibits a shoulder at 406.5 eV, whereas a more uniform peak is evident for the SIP. In order to more clearly illustrate the spectral effects of direct association between the oppositely charged ammonium and chloride ions, the spectra of bare ions with different orientations were calculated. Figure 6 shows the simulated spectra for one chloride at the corner of the tetrahedron of the ammonium ion (top panel) and one chloride at the edge (lower panel); for both cases, the carbon-nitrogen distance is set to 3.28 Å, the position of the CIP minimum on the PMF curve displayed in Figure 4. The calculated spectrum for the bare (unsolvated) NH_4^+ and Cl^- ion pair shows two major group of resonances, (Energy scale relative to LUMO energy): 1s → sσ* (LUMO, exhibits weak transition dipole due to its s character) and 1s → pσ* (LUMO+1, LUMO+2 and LUMO+3, strong resonances located 1-3 eV higher than LUMO), just like the 1s →σ*a1 and 1s →σ*t2 transitions for the isolated NH_4^+ but with broken orbital symmetry. The upper panel shows the states and splittings of pσ* peaks resulting from close approach between H and Cl^-. As Cl^- approaches the H, electron density is transferred to the N-H bond, thus strengthening it. Consequently, the overlap between N and H is increased, shifting the antibonding orbital to a higher energy. In this case, $p_z\sigma^*$ is raised 1.14 eV higher than $p_x\sigma^*$ and $p_y\sigma^*$ since $p_z\sigma^*$ electron density is pointed directly at the chloride ion, while for $p_x\sigma^*$ and $p_y\sigma^*$, the chloride is positioned at about the same distance away so the state degeneracy remains, yielding a resonance two times stronger than the $p_z\sigma^*$ resonance. As for the lower panel, chloride keeps the same distance relative to the nitrogen, but moves to the edge position. Compared with "corner" spectrum shown in red, the 1s→ sσ* (LUMO) transition becomes weaker due to the distortion of spherical

symmetry induced by chloride being smaller at edge position. The electron density of LUMO+2 and LUMO+3 are symmetrical with respect to the chloride ion, and again the degeneracy is preserved, yielding a 2x stronger resonance relative to the 1s→LUMO+1 resonance in the edge spectrum. LUMO+2 and LUMO+3 have smaller electron density along the H-Cl^- axis compared to that of 1s→ $p_x\sigma^*$ and $p_y\sigma^*$ in the corner spectrum (red); hence, the resonance is blue shifted. The electron cloud on LUMO+1 has the greatest distance from the chloride so its transition energy would be the lowest, as shown in Figure 6. In summary, the close contact between chloride and hydrogen on ammonium will split the degeneracy of the original ammonium 1s → σ*t2 resonances, and the shorter the H-Cl distance, the higher the resonance energy.

Since the structural difference in between CIP and SIP at the first solvation shell level is that the chloride association is switched from ammonium to water, before discussing the origin of the spectral difference of CIP and SIP, we should first examine the spectrum of the ammonium ion interacting with a single water. The top panel of Figure 7 displays isosurfaces for the calculated spectrum of water at the edge of ammonium tetrahedron. The nitrogen-oxygen distance is 2.80 Å, the first peak of the radial distribution function. Similar to what we have shown in Figure 6, the resonances can be divided into two groups: 1s → sσ* (LUMO) and 1s → pσ* (LUMO+1, LUMO+2 and LUMO+3, the interaction of water with the isolated ammonium will break the degeneracy of pσ* orbitals depends on the mutual orientation of the molecules). The spectrum of the edge-bonded dimer (red) in Figure 7 shows a very weak 1s → sσ* resonance because the partial negative charge on water does not provide much distortion of the spherical state. The same reasoning holds for the small splitting of 1s → pσ* resonance groups: the pσ* splitting is 0.4 eV in the black edge spectrum in Figure 6, but in Figure 7, for the same configuration with even closer distance, the splitting is not discernible, producing only a side shoulder at lower energy. The lower part of Figure 7 shows the "corner-bonded" spectrum, for which the oxygen is located on the corner of the ammonium tetrahedron and acts as a hydrogen bond acceptor. Now that the oxygen is in much closer contact with a single hydrogen (in comparison with the edge case), the symmetry can more effectively be broken; hence, the LUMO adopts more p character and pσ* splitting is increased to 0.8 eV. Therefore, we can conclude that for ammonium, the spectral effects upon association with chloride and water are similar, but since the oxygen on water carries only a partial negative charge, the stabilization effect from symmetry breaking will be smaller, leading to weaker 1s→LUMO resonance and smaller pσ* splitting. These two features are also evident in the calculated fully hydrated CIP and SIP spectra shown in Figure 5: although the overall spectral shape is broadened by mixing with water states, CIP spectrum exhibits a stronger pre-edge feature at 403.9 eV and a side shoulder at a relatively high energy compared to the main resonance (see Figure 5). This indicates that even in a fully hydrated chemical environment, the spectral effects from chloride can outweigh those from water solvation.

The spatial distribution function from MD trajectory suggests that the water and chloride compete for the corner H-coordinate sites, i.e. water and chloride preferentially associate with ammonium ion on the tetrahedral corners. Hence the fully solvated CIP spectrum exhibits a side shoulder at higher energy resulting from the coordinated pσ* resonance, as shown in Figure 6; if the chloride is preferentially bound at the tetrahedral edge, the shoulder would either show up at the lower energy or no visible shoulder would

be present, since the splitting is too small and/or obscured by water states. In our experiment, the small pre-edge feature at 403.9 eV represents the 1s → sσ* transition and is followed by stronger pσ* resonances with a more prominent shoulder at higher energy as concentration increases. This observation matches with the calculations; thus, in real solutions, both chloride and water are preferentially bound on the corner site and the rise of the pσ* shoulder resonance with increasing concentration can serve as a direct probe of the ammonium-anion interactions in aqueous systems, which are difficult to access by other methods.

The Law of Matching Water Affinities proposed by Collins[3,4] suggests that ions with similar hydration free energies form the most stable contact ion pairs. Both NH_4^+ and Cl^- are chaotropes (water structure breakers) with similar hydration energies so it is expected that they can form stable CIPs. For comparison, the spectra of $(NH_4)_2SO_{4(aq)}$ (chaotrope + kosmotrope) with various concentrations were measured, and are displayed in Figure 8. There are no concentration-dependent features, so the solvation environment stays the same regardless of the concentration change. No ion-pairing signature is evident as concentration increases, as for the case of ammonium chloride solutions. However, the shoulder at 407.5 eV is always present, even in low concentration solutions, since the energy of shoulder is higher than the shoulder resonance observed in NH_4Cl spectra, it can't result from the preferential binding of water. Therefore, a reasonable inference is that the splitting results from the double negative charge on sulfate ion, wherein the high charge perturbs the delocalized water states.

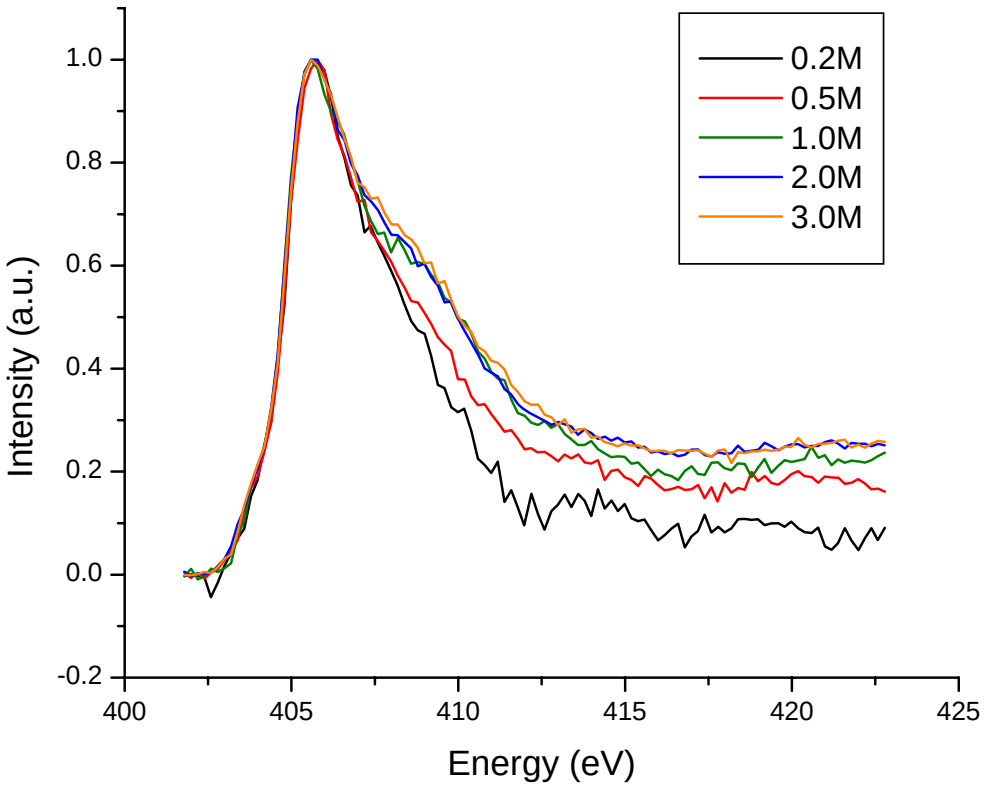

Figure 3. Nitrogen 1s NEXAFS spectra for different concentration of NH_4Cl solutions. All spectra are peak normalized at 405.6 eV

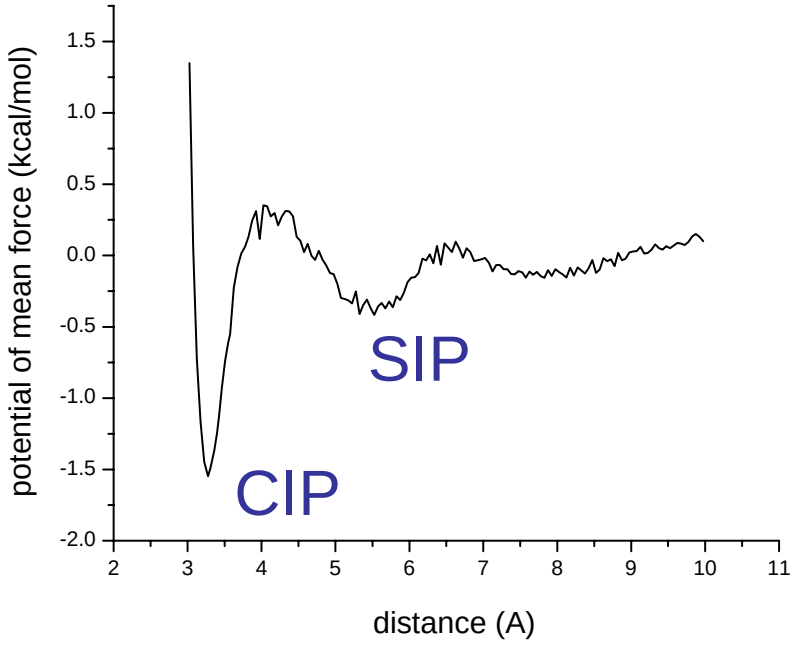

Figure 4. Potential of mean force for NH_4^+-Cl^- along the nitrogen-carbon distance. The minimum at 3.28 Å presents the stable contact ion pair (CIP) and the second minimum at 5.50 Å marks the solvent shared ion pair (SIP) which has one layer of solvent in between the cation and anion.

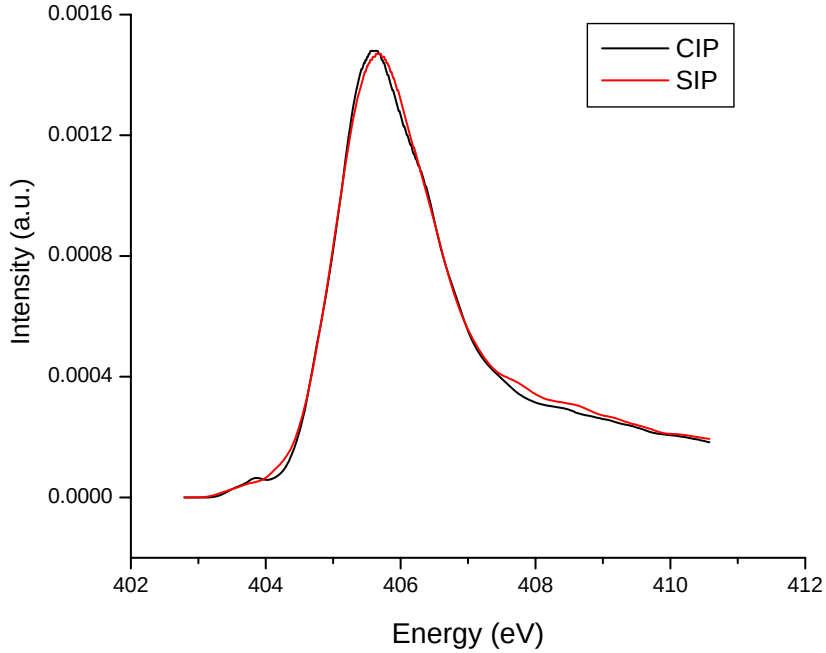

Figure 5. Average calculated spectra for NH_4^+-Cl^- contact ion pair (CIP) and solvent shared ion pair (SIP) at Nitrogen K edge.

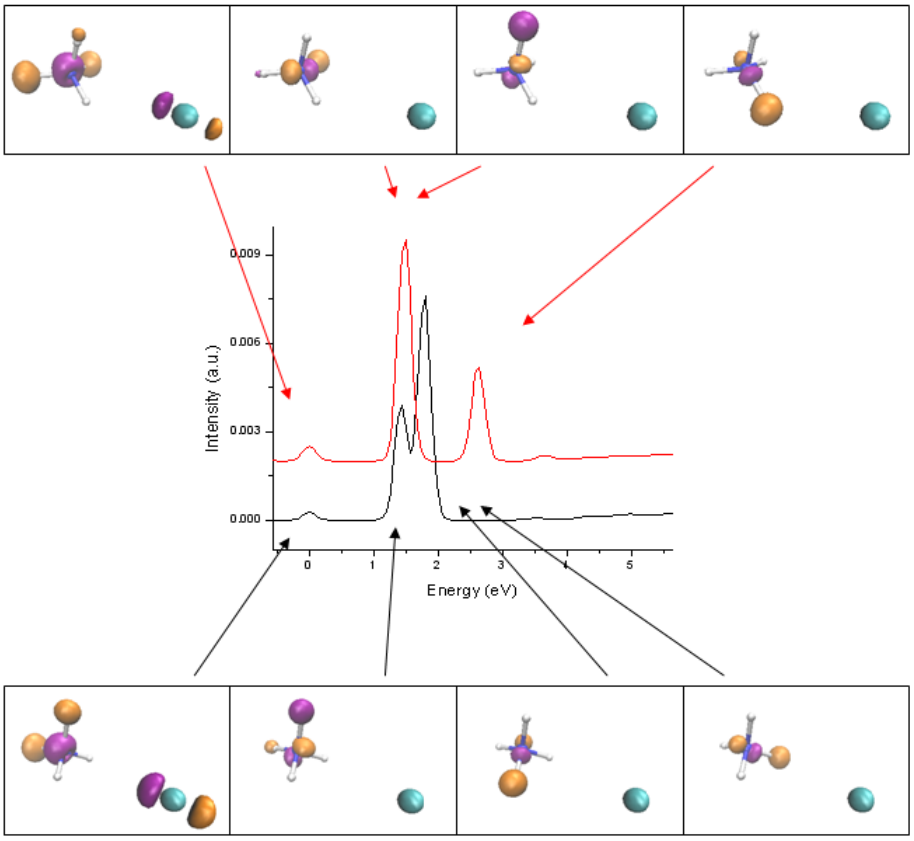

Figure 6. The simulated spectra of bare ammonium and chloride. Top panel with the red spectrum: chloride at the corner of ammonium. Lower panel with the black spectrum: chloride at the edge of ammonium. The nitrogen-chloride distance for both cases are the same, d=3.28 Å. The positions of the arrows in the figure don't represent the energy but indicate which resonance the respective isosurface belongs to.

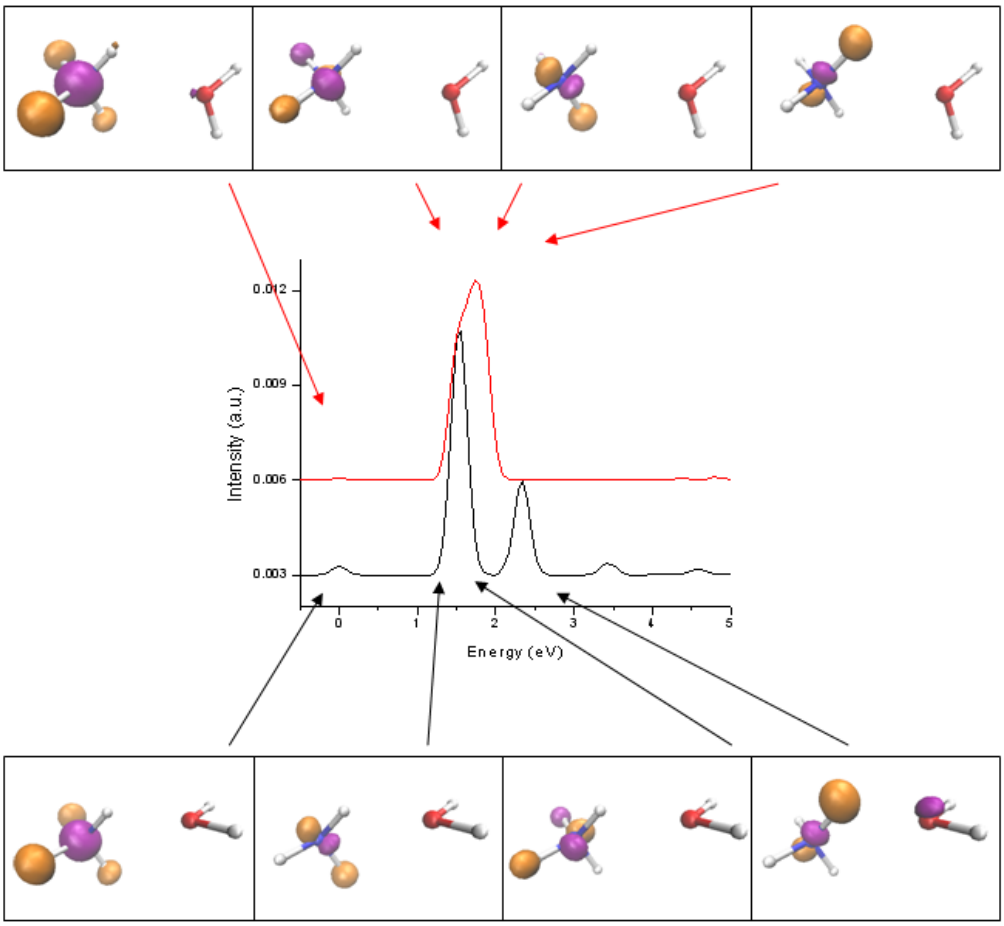

Figure 7. The calculated spectra of bare ammonium and water. Top panel with the red spectrum: water at the edge of ammonium. Lower panel with the black spectrum: water at the corner of ammonium, with oxygen on water acting as H-acceptor. The nitrogen-oxygen distance for both cases are the same, d=2.80 Å. Arrows indicate the resonance the connected isosurface belongs to.

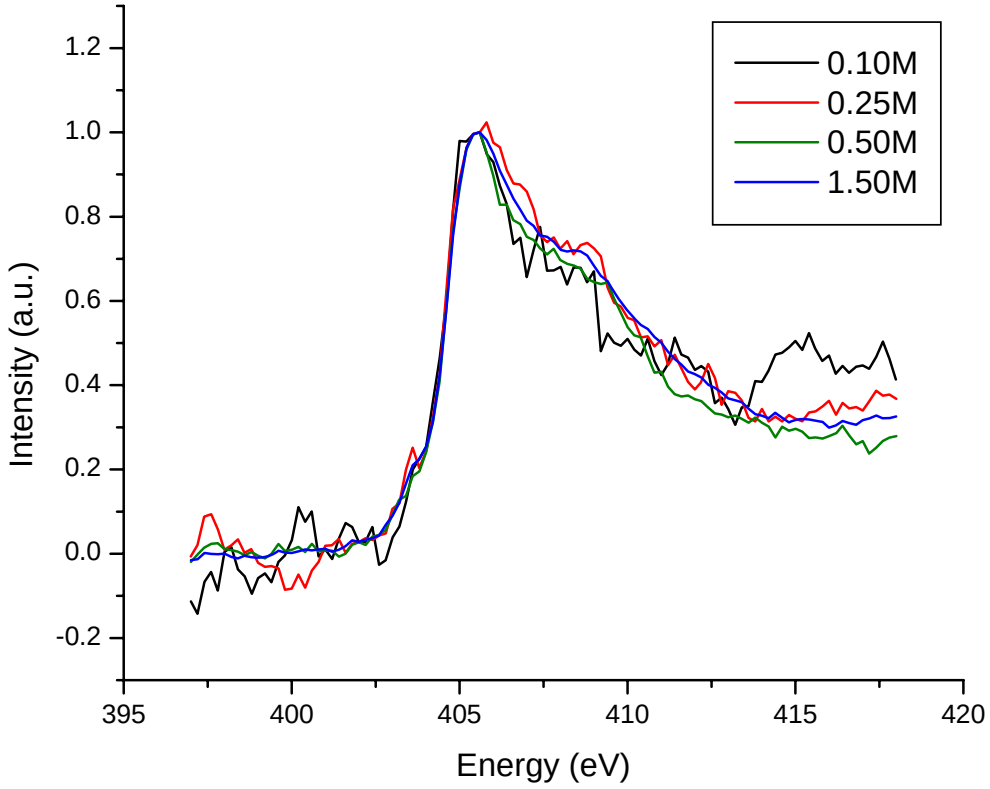

Figure 8. Nitrogen K-absorption edge spectra for ammonium sulfate at various concentrations. All spectra are peak normalized at 405.6 eV

Guanidinium Chloride

Figure 9 shows nitrogen K-edge core level spectra of GdmCl at concentrations ranging from 0.5 to 6.0M; spectra are normalized to the peak heights of the first resonance at 401.9 eV for clearer viewing of the electronic structure change at higher photon energy. The overall spectral shape is characterized by two resonances at 401.9 and 404.7 eV, denoted A and B, followed by a broader feature C centered near 410 eV. As the concentration increases, peak B shifts to lower energy with higher intensity. Peak C is too broad to ascertain exactly how the spectral shape varies with concentration; therefore the analysis will focused on peaks A and B.

To interpret the measured NEXAFS spectra, we employ the XCH procedure described above. The Gdm^+ carbon-carbon pair correlation function calculated from the MD trajectory is shown in Figure 10; the peak at 3.9Å indicates a significant tendency for the Gdm^+ ions to form self-associated contact ion pairs (CIP), i.e. Gdm_2^{2+}, since 3.9Å is larger than the van der Waals contact distance but not large enough for placing one water between the ions. The spatial distribution functions shown in Figure 11 further indicate stacking of pairs of Gdm^+ ions in solution. There is a clear trend for water to accept hydrogen bonds from the hydrogen atom on Gdm^+. The preferential orientations for water permit simultaneous interaction with hydrogens from two different amine groups while the counter ions (Cl^-) are in competition for the same acceptor sites. There is no

recognizable hydration shell around the Gdm^+ ion, and its hydrophobic "face" introduces a large void on top if it does not bind with another Gdm^+. This observation is consistent with previous MD results.[10]

To evaluate the stability of this counterintuitive cation-cation pairing, the classical potential of mean force (PMF) was calculated using equation (1) again. As shown in Figure 12, the computed PMF for two Gdm^+ ions has a well-defined CIP minimum at 3.9Å and a barrier of 0.53 kcal/mol towards the free pair region where $r > 8.0$ Å. In contrast, the PMF for the geometrically similar nitrate/nitrate ion pair calculated by the same technique for the same concentration of sodium nitrate solution exhibits the conventional electrostatic repulsive potential, with no attractive behavior evident at short distance.

It is interesting that our potential well is much shallower compared with the PMF previously calculated from Monte Carlo simulations[9]; the CIP is stabilized by 6.73 kcal/mol for the TIP3P water model with a dissociation barrier of 6.26 kcal/mol. There are several differences between the two studies. First, the MC simulations were performed on a single Gdm pair without any counter ions, while in our calculation a realistic solution of 1.8M GdmCl was modeled. Therefore, in the MC study, the Gdm^+ pair is stabilized purely by the strong in-plane hydrogen bond network without the competition of chlorides. Second, Maigret *et al.* constrained the two Gdm^+ ions to remain in parallel planes and kept the ions rigid, whereas we allow free motion, constrained only by molecular configuration and the thermal conditions. The unrealistically rigid structure along with the staggered configuration used in Ref. 7 minimizes the electrostatic and steric repulsion, also optimizes the quadrupole-quadrupole interactions, resulting in a deeper well compared to our PMF, presented in Figure 12. The previous MD studies[8,10] reported a similar carbon-carbon radial distribution function, and would therefore yield a similar PMF curve like ours even though they use both a different water model and force field parameters; hence the different dissociation barriers are a results of the fundamental differences between Monte Carlo and MD simulations.

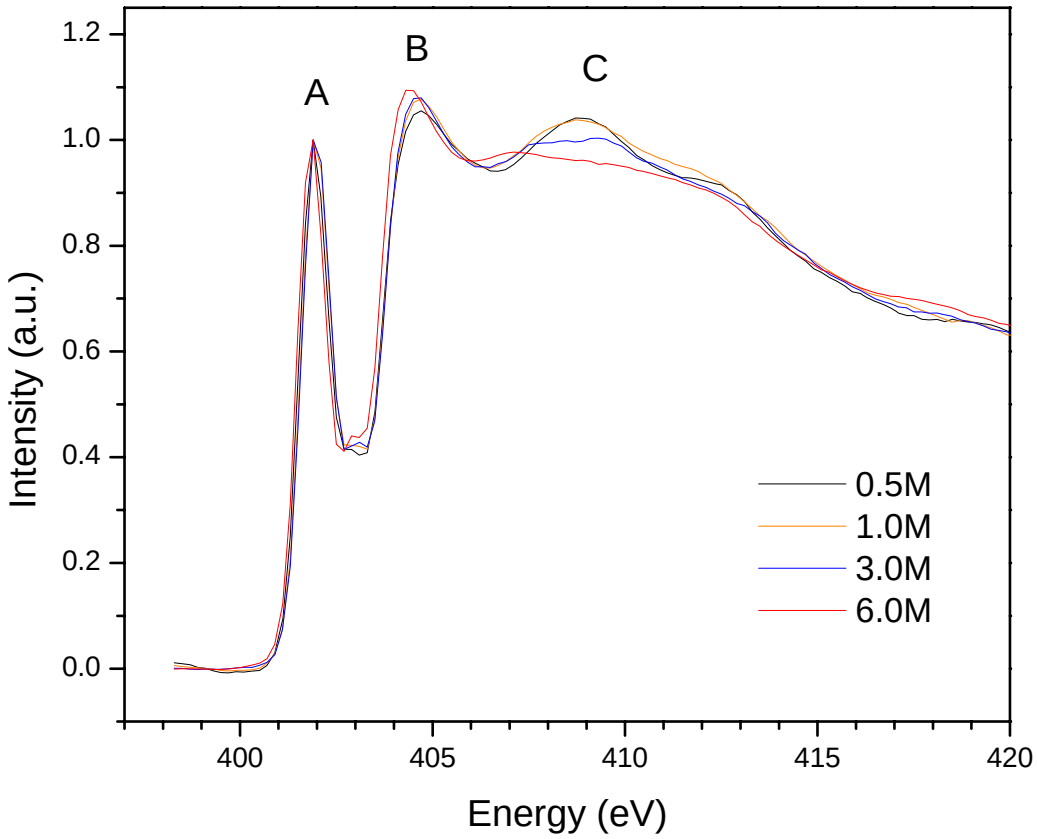

Figure 9. Measured nitrogen K-absorption edge spectra of aqueous guanidinium chloride solutions for various concentrations. A, B, and C mark the major groups of core level resonances.

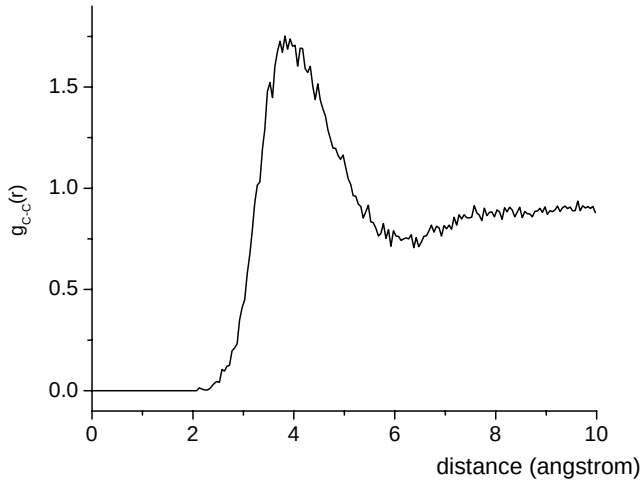

Figure 10. The carbon-carbon radial distribution function $g_{CC}(r)$

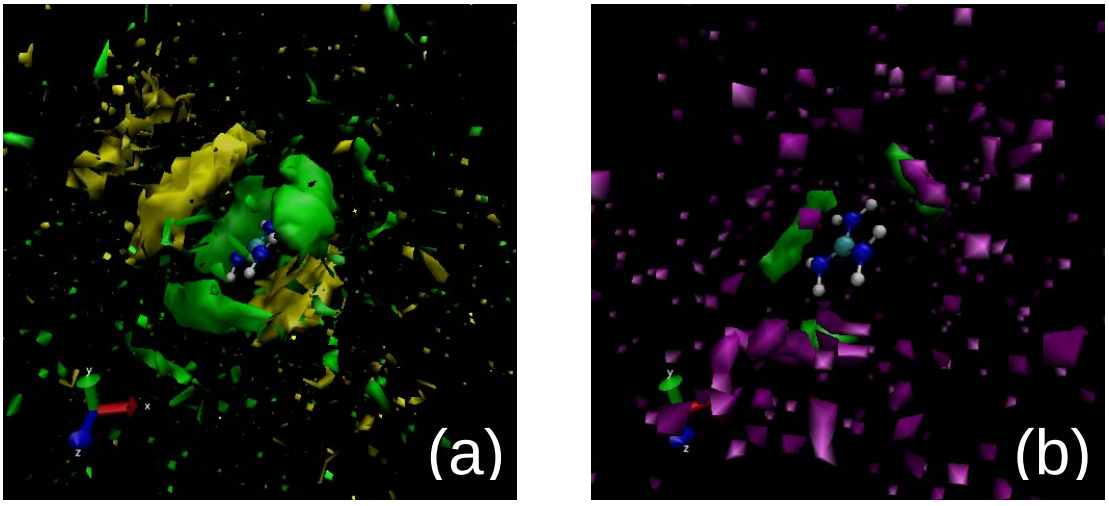

Figure 11. (a) Calculated spatial distribution function of carbon (yellow) and water (green) around the Gdm^+ ion, demonstrating cation-cation stacked pairing. (b) Same spatial distribution function showing chlorine (purple) and water (green) distribution.

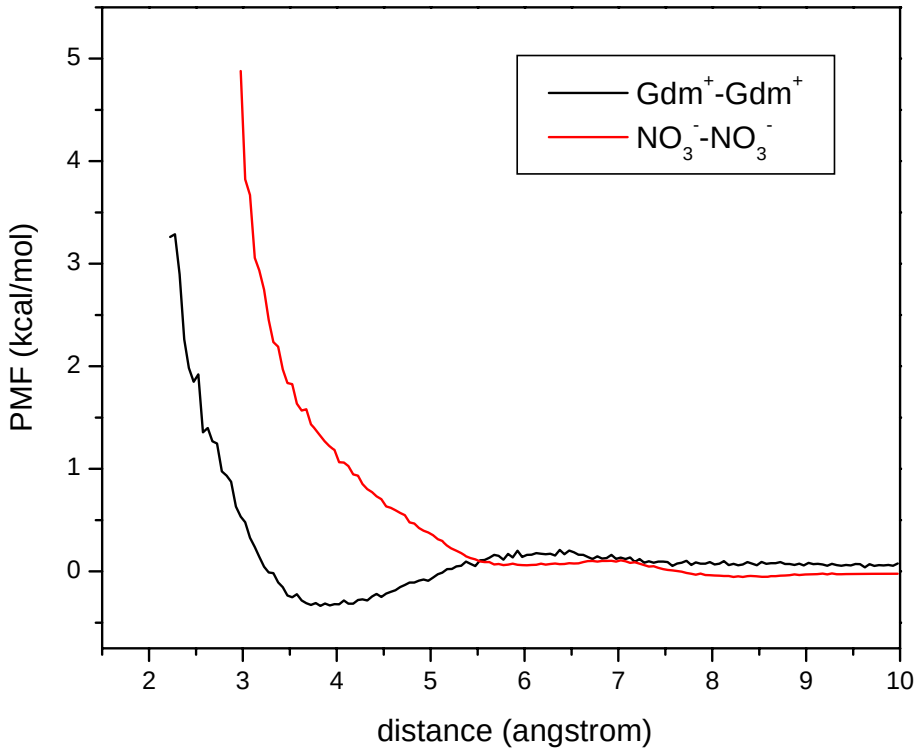

Figure 12. Potential of mean force for guanidinium ion pairs (black), compared with that for the structurally similar, but independently solvated nitrate ion pairs (red) in water along the C---C (N---N) distance coordinate.

To illustrate the spectral signatures of this cation-cation pairing, Figure 13 presents calculated NEXAFS spectra of stacked and free pairs of Gdm^+ ion in water, along with the experiment results. The Gdm^+ pair spectrum was calculated with the XCH method from 100 snapshots randomly choosen from the trajectory file under the carbon-carbon distance constraints: 3.7 to 3.9 Å for the stacked pair and 10.0 to 10.5 Å for the free pair. Each MD snapshot produces six spectra from the excitation of the six different nitrogens on the Gdm^+ pair. The simulated spectra show similar resonance peaks A, B and C, as observed in the experiment, but with smaller spacing between the features. This results from the underestimation of water band gaps by DFT. A typical simulated spectrum with the corresponding isosurfaces is shown in Figure 14, wherein the excited nitrogen is marked by an asterisk. As seen from the isosurface, peak A is composed of two peaks: A1 at 401.91 eV and A2 at 402.04 eV. Peak A1 (LUMO) represents a transition from the 1s orbital to a localized sσ* state with mixture of π character on other atoms, whereas peak A2 (LUMO+1) comprises a transition to a pure π* state, with 3-7 times higher oscillator strength than that of A1, depending on the molecular configurations. Interestingly, the ground state calculation showed that the LUMO of ground state Gdm^+ is a pure π* state and a $s\sigma^*(NH_2)$ state as LUMO+1, which is the opposite ordering observed in the core-excited state. Figure.15 further demonstrates this orbital reversal by displaying the isosurfaces of ground state and core-excited bare Gdm^+ (without waters). When an electron is excited from nitrogen core level, the effective nuclear charge increases and nitrogen becomes oxygen-like, lowering the orbital energies. Because σ orbitals penetrate closer to the nucleus, their energy will decrease more than that of the π state, leading to the orbital reversal.

This core excitation-induced orbital reversal is also found in similar nitrogen-containing delocalized systems, like aniline ($C_6H_5NH_2$), for which *ab initio* calculations revealed $\sigma^*(NH_2)$ character for the aniline LUMO.[29,30] With their higher experimental resolution, Duflot *et al.* suggested 3s Rydberg orbital with $\sigma^*(NH_2)$ character.[31] There have been some debates on assignments of the LUMO+1: the EICVOM model[30] revealed π* character whereas others showed a different level mixing of 3p Rydberg orbital, $\sigma^*(NH_2)$ and π*.[29,31,32] However, if the amine group is replaced by a nitro group ($-NO_2$) the N 1s spectrum would be dominated by the strong $N1s \rightarrow \pi^*_{NO}$ transition (LUMO) and there is no orbital reversal, due to the unsaturated character of the nitro group.

To test the validity of orbital reversal phenomenon, we employ a similar DFT-SCF method called maximum overlap method (MOM) to compute the excited state energies and their corresponding isosurfaces. MOM works by choosing orbital occupancies that maximize the overlap of new occupied orbitals with the set previously occupied. The convergence speed and exactitude of MOM explicitly depend on the initial guess of orbitals, so we design a series of calculation incorporates a two-way approach from ground state to core-hole excited state, for which the "flow chart" is shown in Figure 16. It starts with ground state (GS) calculation. Q-chem has five options for generating an initial starting point for SCF and those can be selected using *scf_guess* rem variable (rem is a Latin for "thing", global options for Q-chem jobs are stored in an array called the rem array and the parameters in the array are called the rem variables). For ground state calculation we use a superposition of atomic densities (SAD) to generate the density matrix for the entire molecule and store the MO coefficients in a *save* directory for future

use. The next step is to switch one of the nitrogens on Gdm^+ to oxygen in order to generate a localized core-hole, marked as GS-O. The MOM can be controlled by *rem* variable "*mom_start*", which specifies the SCF iteration on which the MOM procedure is first enabled. To help maintain an initial configuration it should be set to start on the first cycle. On the other hand, if MOM is to be used to aid convergence, an SCF without MOM should be run to determine when the SCF will start oscillating. MOM should be set to start just before the onset of oscillations to avoid maintaining an initial configuration that may be far from the converged one. Here we want to keep the initial configuration, so *mom_start* is set to 1. The *scf_guess* is set to "*read*" so the MO coefficients from a previous job can be read in; every calculation in the flow chart except the GS calculation is configured to read the MO information from the previous calculation, and employs MOM from the beginning of SCF procedure. After the GS-O calculation, it can go either to the "XPS-O" calculation, which simulates the charged excited system corresponding to an X-ray ionization process (XPS), keeping the replaced oxygen but remove one electron from the core state, or another choice, "XPS-N" calculation, which is basically the same as XPS-O but switching the oxygen back to nitrogen. The orbital occupancies can be manipulated using the *$occupied* section (works for RHF and UHF only); the MOM is then invoked to preserve this orbital occupancy. The molecular orbitals at the end of XPS calculation will form input orbitals for the final XAS calculation (XAS-N, the nitrogen has to be switched back if from an XPS-O calculation). Note that when Q-chem writes out the orbitals from the XPS run, the original state which had the core hole is not occupied anymore. Instead, Q-chem orders this state as the first available empty level, even though its eigenvalue is much lower then any of the valence states. Therefore, when doing the XAS-N calculation, the extra electron should not be put into this first available empty state, otherwise the system would simply relax back to the ground state. Instead, the electron should be added to the next higher energy empty state, which is the actual LUMO of the molecule. Tuning the iterative subspace size "*diis_subspace_size*" can help the system to converge; the default value is 15, but it can be set to 10 or 5 if one encounters oscillations in the energy, or finds non-convergence.

Figure 17 shows the isosurfaces of LUMO and LUMO+1 of the MOM serial unrestricted Kohn-Sham SCF calculation using PBE as the exchange-correlation energy functional. In PW(Plane Wave)SCF, we used the same type of energy functional, thus it yields the same results for the GS calculation: LUMO is the delocalized π^* and LUMO+1 would be $s\sigma^*(NH_2)$. Then the sequential calculation is followed by the GS-O calculation. The drop in energy when replacing nitrogen with oxygen leads to the localized $s\sigma^*(OH_2)$ serving as LUMO and π^* as LUMO+1. After the GS-O calculation, it can go to either the XPS-O or XPS-N route, and then merge back to the XAS calculation. The two XAS results from these two paths don't converge: the LUMO from XPS-O path is $s\sigma^*(NH_2)$ and $p\sigma^*(NH_2)$ is LUMO+1; on the other hand, the LUMO from XPS-N path is the delocalized π^* and $s\sigma^*(NH_2)$ acts as LUMO+1. They all inherit the orbital from the XPS calculation they came from. The ΔE showed in Figures 17 and 18 represents the total energy difference in between the XAS state and ground state, i.e., the 1s→LUMO resonance energy. The ΔE from the XPS-O path (401.97 eV) matches well with the PWSCF calculation on bare Gdm^+ (402.5 eV), but the ΔE from XPS-N path was too high, and with a different LUMO character. Thus we may encounter the problem on MOM that

the orbital relaxation is slower than the energy convergence during the XPS-N route. Setting a smaller convergence threshold will fix this problem. The 1s→LUMO resonance energy from the XPS-O path is in good agreement with PWSCF calculation and adopts the same LUMO feature; LUMO+1 doesn't match, probably because it's not the state the system put the electron into.

Therefore, the MOM procedure is somehow comparable with PWSCF; we can test how other exchange-correlation functionals would affect the SCF results. Figure 18 displays the results from the same serial calculation but using hybrid HF-DFT SCF with B3LYP exchange-correlation functionals. The first interesting fact is that the ground state orbitals are reversed, from those of PBE-ground state. The GS-O, XPS-O, and XPS-N calculations all share the same molecular orbital characters with the same type of calculation using PBE. The XAS calculations from both routes converge to $\Delta E = 402.71$ eV and the same LUMO, LUMO+1 feature as XAS (from the XPS-O route, using PBE) predicts: $s\sigma^*(NH_2)$ as LUMO and $p\sigma^*(NH_2)$ as LUMO+1. Since with B3LYP the LUMO of the ground state is $s\sigma^*(NH_2)$, there is no orbital reversal, as shown in PWSCF and MOM with the PBE functional. Nevertheless, the two most common exchange-correlation functionals (PBE and B3LYP) showed the same orbital character for the LUMO, matching the PWSCF results. The MOM predicts LUMO+1 to be $p\sigma^*(NH_2)$; with its local p character, one can imagine it would produce a strong resonance. The first peak in the experimental spectra at 401.9 eV is strong but the transition linewidth is too narrow to be considered as a σ^* transition; thus, the MOM prediction on LUMO+1 is suspicious. The same MOM calculation is carried out with a pure Hartree-Fock SCF calculation, for which the results are shown in Figure 19. The LUMO of ground state is $s\sigma^*(NH_2)$ and a higher order mixture of $s\sigma^*(NH_2)$/ $p\sigma^*(NH_2)$ state serves as LUMO+1. For all different SCF methods we've tested, their GS-O calculations all exhibit the same orbital character of LUMO and LUMO+1, so as the XPS-O calculations, showing the dominating effect of orbital energy drop by replacing the nitrogen with oxygen. The XAS calculations converge such that the mixture state would become the LUMO and the corresponding $\Delta E = 403.70$ eV is too high due to the fact that HF doesn't account for electron correlation energy.

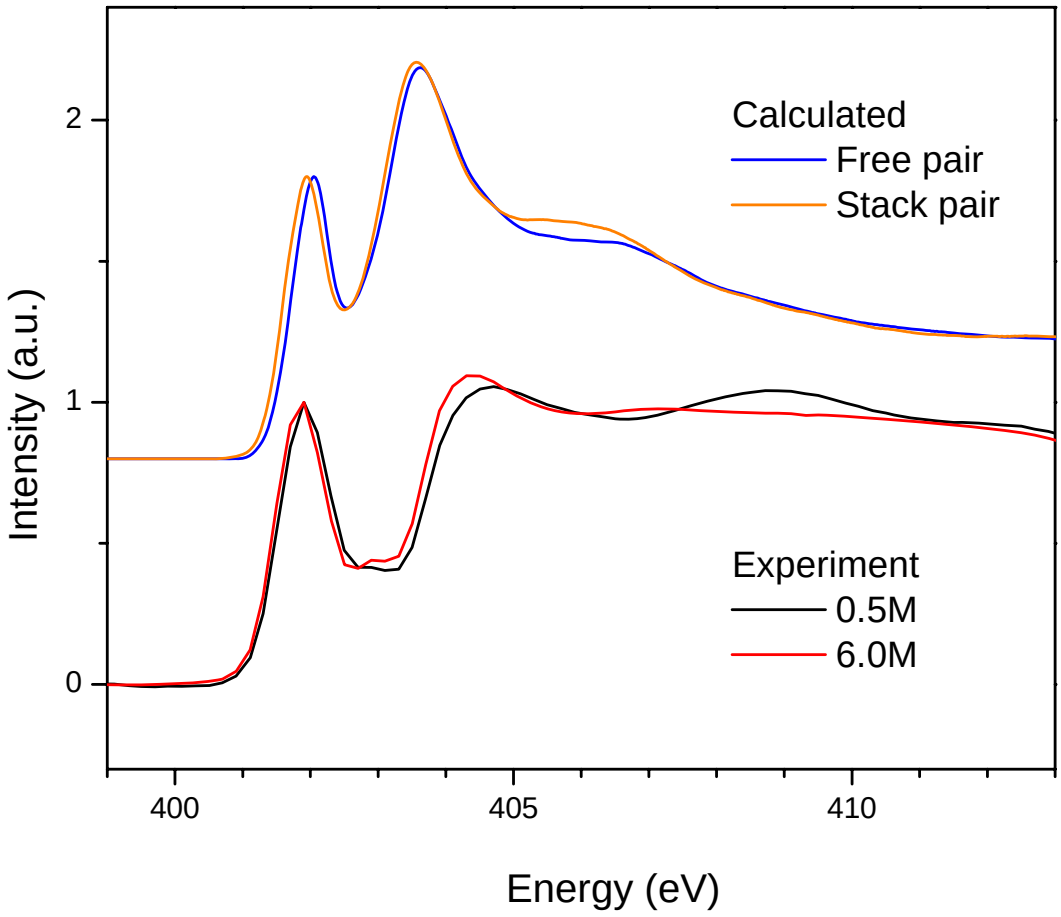

Figure 13. Upper: Calculated nitrogen K-edge spectra for free and stacked Gdm^+ pairs. Each spectrum represents the average of 100 individual spectra. Lower: experimental nitrogen K-edge spectra for the lowest and highest concentrations: 0.5M and 6.0M solutions. All spectra have been normalized with the peak heights of the first resonance.

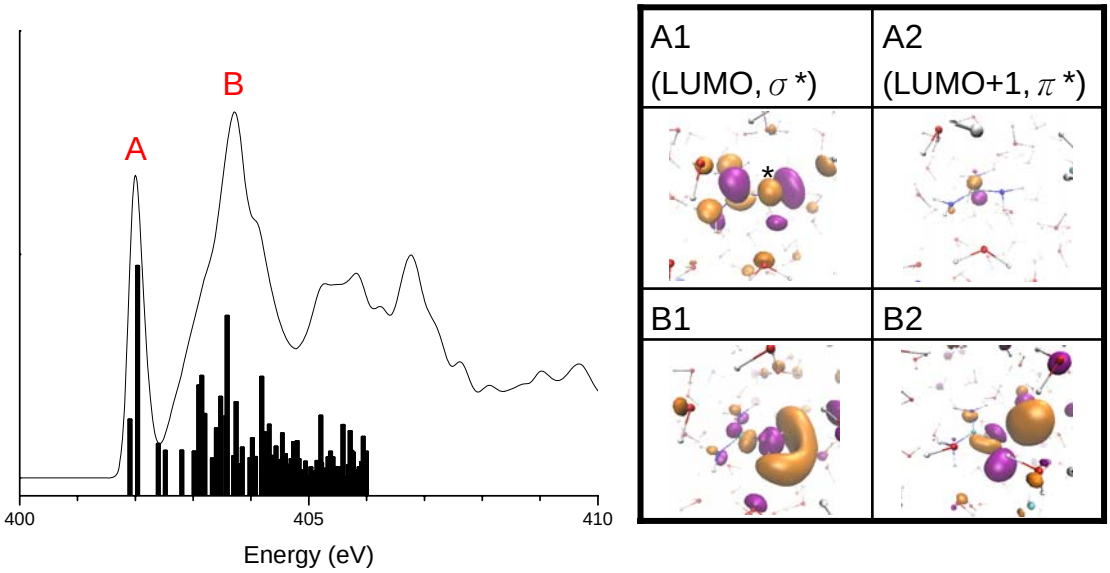

Figure 14. Single snapshot spectra with stick spectra and associated states (15% isosurface) for free Gdm^+ pair. Peak A comprises two transitions, A1 (1s→sσ*(NH_2), 401.91 eV) and A2 (1s→π*, 402.04 eV). Lower panel shows the strongest transitions B1 (403.10 eV) and B2 (403.59 eV) in Peak B group.

Ground state		
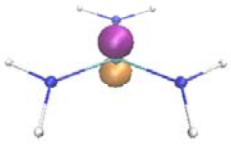	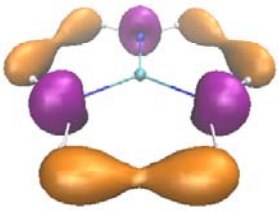	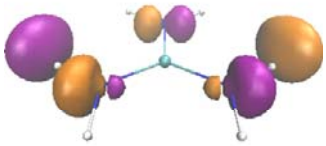
LUMO	LUMO+1	LUMO+2
Core-excited state		
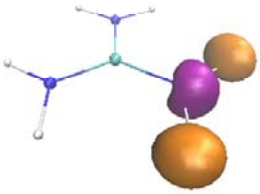	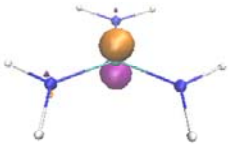	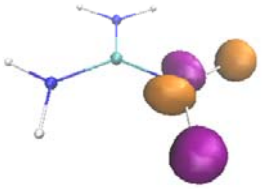
LUMO	LUMO+1	LUMO+2

Figure 15. Comparison of the unoccupied states for ground state and core-excited isolated Gdm^+ ion.

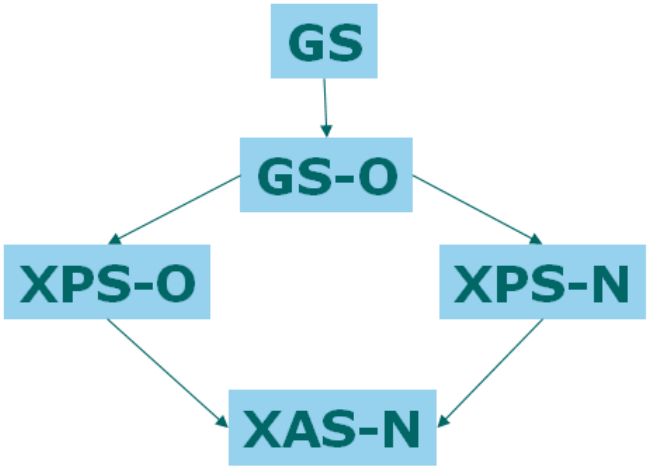

Figure 16. Flow chart for using the maximum overlap method to calculate SCF nitrogen

core-hole excited states for guanidinium, or more generally speaking, symmetrical nitrogen-containing molecule. GS: ground state. GS-O: replace one of the nitrogen with oxygen in order to create a localized hole. XPS-O: keep the oxygen and remove one 1s electron. XPS-N: replace the nitrogen back and also remove one 1s electron. XAS-N: keep the core hole and put the electron into LUMO, ideally the electronic structure of XAS states from both routes will converge.

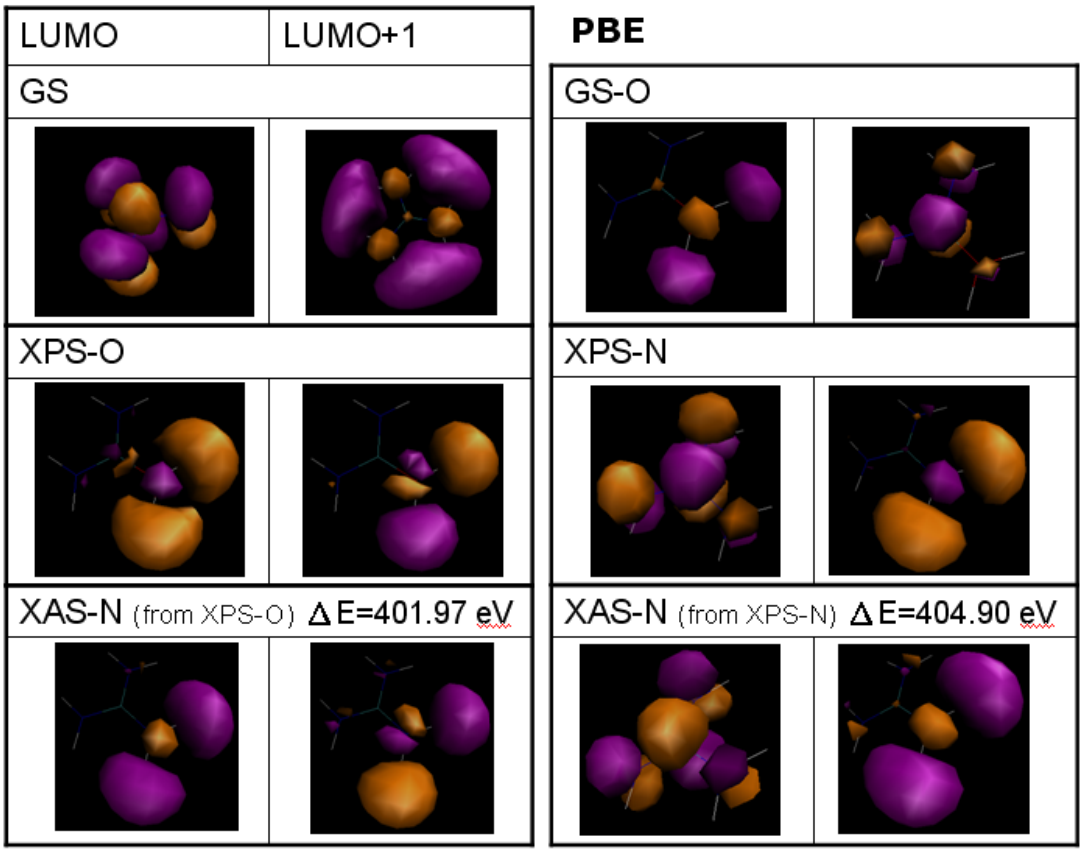

Figure 17. The isosurfaces for LUMO and LUMO+1 states of isolated guanidinium in the MOM sequential calculations by the Kohn-Sham SCF method using the PBE form of the generalized gradient approximation to the exchange-correlation potential. ΔE indicates the energy difference in between the core-excitation state and the ground state.

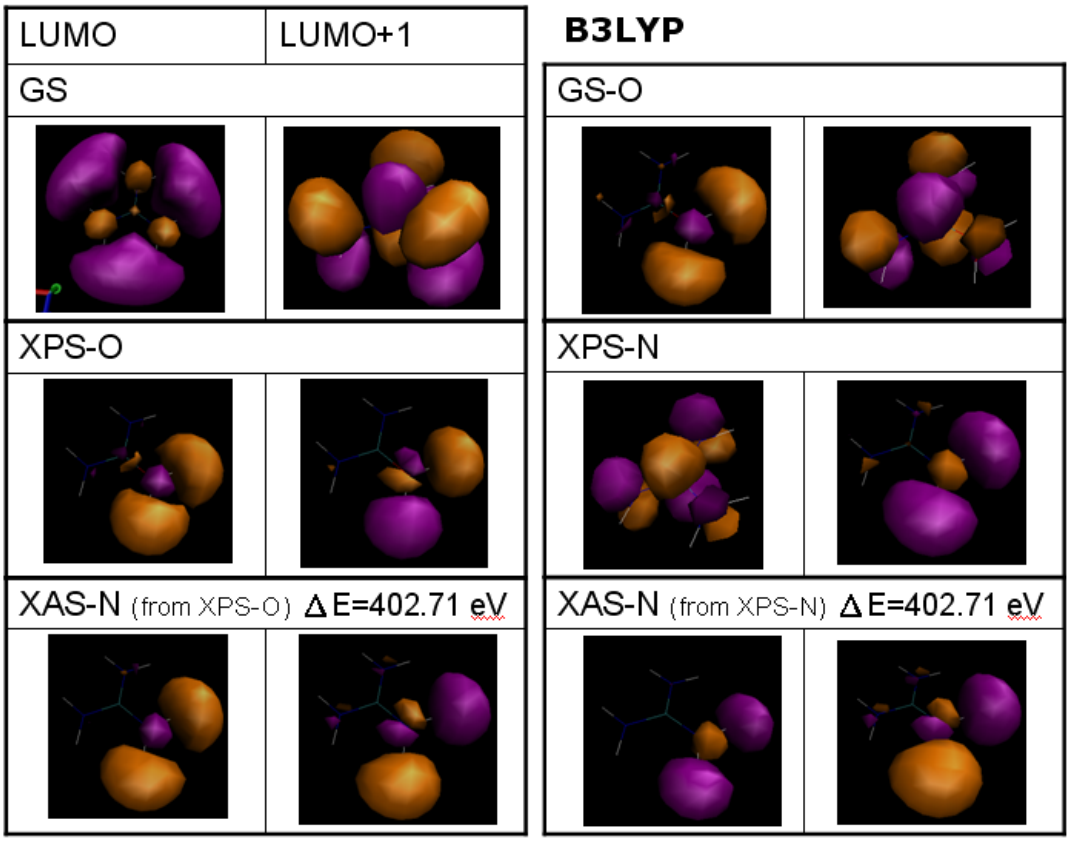

Figure 18. The isosurfaces for LUMO and LUMO+1 states of isolated guanidinium in the MOM sequential calculations with the hybrid HF-DFT SCF method using B3LYP as the exchange-correlation functional.

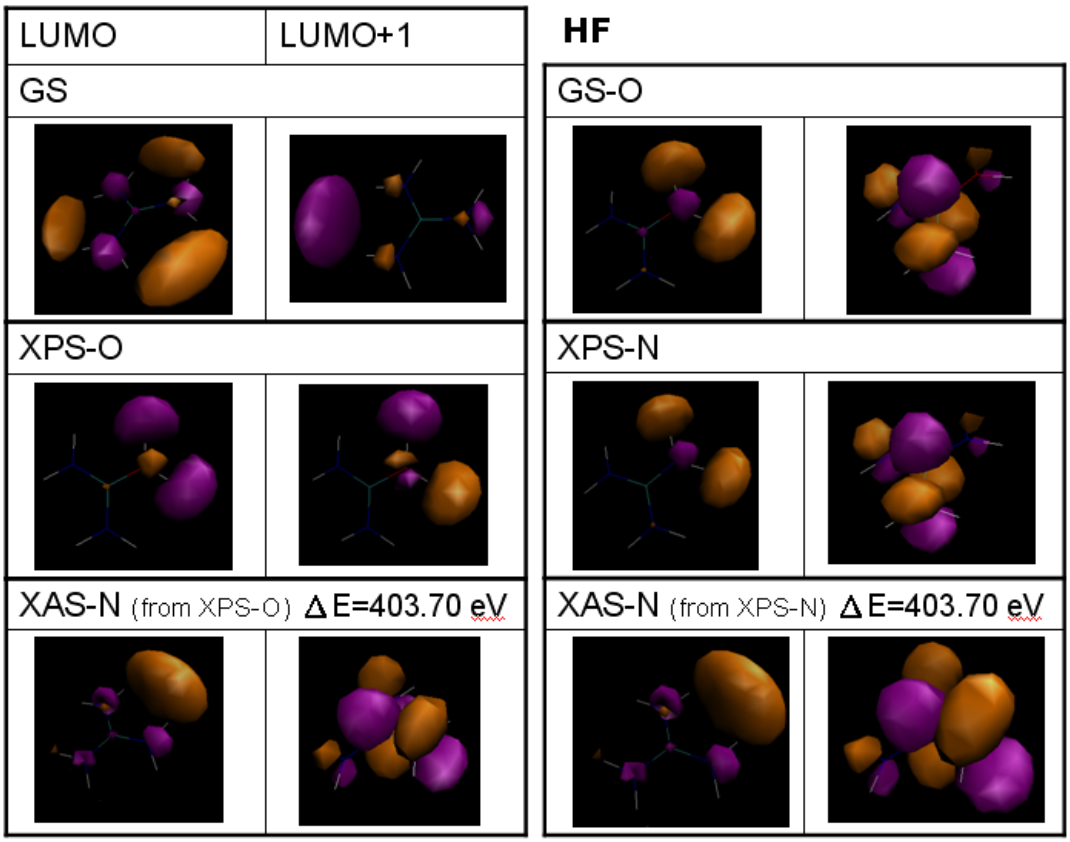

Figure 19. The isosurfaces for LUMO and LUMO+1 states of isolated guanidinium in the MOM sequential calculations using the Hartree-Fock SCF method.

In addressing the role of water in the unoccupied molecular-orbital electronic structure, it is useful to examine the projected density of states (DOS) of water and Gdm^+ (Figure 20). The first peak of the H_2O DOS matches the energy of resonance A1, while the first peak of Gdm^+ DOS matches that of resonance A2. A2 is also the state that has the highest Gdm^+ DOS and the only state with a Gdm^+ DOS higher than that of H_2O, makes it the strongest transition, as observed in our spectra. Peak B reveals a large number of resonances from the mixing of water excited states. Figure 14 displays the isosurfaces of the two strongest resonances in the peak B group — B1 at 403.10 eV and B2 at 403.59 eV. B1 represents the transition from the 1s orbital to a localized sσ* state mixing with π* character on other atoms. It is similar to A1 but with higher H_2O DOS, i.e., a more diffuse state. The B2 feature originates from the LUMO+2 state of bare Gdm^+ (pσ*(NH_2), see Figure 15) which interacts with water states.

For both peaks A and B, the trend of spectral redshift from free to stacked pairs, matches with the experimental observation of a redshift when moving from lower to higher concentrations. The redshift in peak A can be explained by state mixing between the components of the Gdm^+ pair: as the two Gdm^+ ions approach closely, the two π systems interact with each other and create a more delocalized charge distribution, thus stabilizing the π* state, which is the major component of peak A. For peak B, the σ system interacts more weakly with the other Gdm^+ ion, so the observed redshift must be related to the surrounding solvation environment. Figure 20 demonstrates that peak B is

mainly composed of water-rich states, so that it will be sensitive to the water-water interactions. When two solvated Gdm^+ ions associate, they release water molecules from their own solvation shells, and the water hydrogen-bond network becomes extended, again stabilizing the final states. This results in the redshift of peak B in the calculated spectra, moving from free to stacked pairs. In our experiments, the same trend of spectral redshift of peaks A and B is observed when moving from low to high concentrations; therefore, we reach the conclusion that as concentration increases, there is a higher probability for contact ion pairing between Gdm^+ ions. If no contact ion pairs form, the electronic structure of the Gdm^+ ions will not be expected to vary so much with concentration.

The association of two weakly hydrated (chaotropic) Gdm^+ ions represents a remarkable ion-specific effect and it is in accord with the Law of Matching Water Affinities. Since Gdm^+ corresponds to the side chain of arginine, which is protonated at biological pH, Hence, a similar pairing between Gdm^+ ion and arginine side chains of proteins could exist. It is believed that there are two principal mechanisms for ion-induced protein unfolding: direct interaction of the ion with some parts of the protein or modification of the solvating water structure. The direct interaction model has been indicated as having a primary relevance in protein destabilization by Gdm^+ salts[14,33] but the temperature-excursion IR study by Scott *et al.* also showed a substantial restructuring of the water H-bond network upon addition of GdmCl.[34] Our technique probes both the direct interaction and the change on the solvation environment, but cannot easily separate the relative contribution of the two mechanisms.

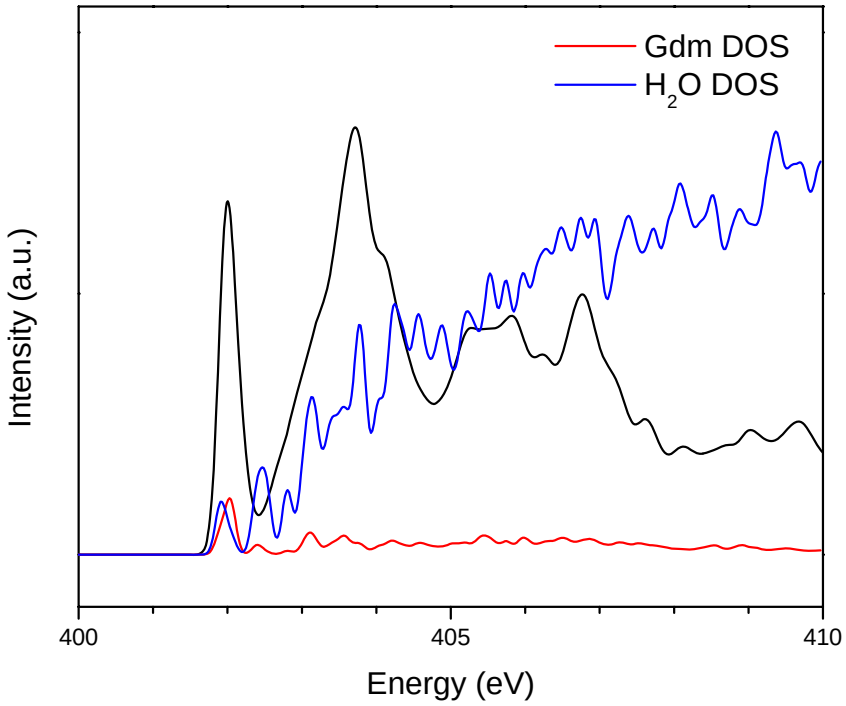

Figure 20. Sample snapshot spectrum of solvated guanidinium (the same one showing in Figure 14) with corresponding projected Gdm^+ and water density of states.

To further support this interpretation of the observed spectral shifts, we examine calculated spectra of GdmCl in crystalling form. The crystal structure data were taken from Haas *et al.*[35] GdmCl crystallizes in the orthorhombic system with space group *Pbca*. The crystal structure consists of chloride ions coordinated by three different Gdm^+ ions, two of which are coplanar. The third Gdm^+ ion is nearly perpendicular to this plane. Figure 21 depicts the atomic arrangement around Gdm^+ in the crystal: Each Gdm^+ coordinates to three chloride ions, with two of these chloride ions associating onto another Gdm^+ which is coplanar with the original one, and the same unit is repeated, forming a chain-like structure. As shown in Figure 21, the three lower Gdm^+ ions are in the same plane and the planar Gdm^+—Cl^-—Gdm^+—Cl^- structure is repeated along x-axis. The top chloride ion coordinated to N1 and N2 is different, binding with two other Gdm^+ ions and neither of which is in the same plane displayed in Figure 21. From symmetry considerations, if the crystal were perfect, N1 and N2 would be equivalent, but there is actually a small variation in the chloride-nitrogen distances. The average N1-(top chloride) distance is 3.27Å, while 3.36 Å is found for N2-(top chloride) distance. Therefore, there are three different types of nitrogen atoms in the crystal, N1, N2 and N3. The corresponding calculated spectra are shown in Figure 22, along with the spectra of bare Gdm^+ and solvated free Gdm^+ pair taken from Figure 13. The overall spectral shape of N1 and N2 spectra are similar, but with a shift on the first peak resulting from the same 1s → LUMO ($s\sigma^*(NH_2)$, π^* mixed state) and 1s → LUMO+1 (π^*) resonances described earlier. Since N1 has a smaller distance to the N2-shared chloride (3.27Å) compared to that of N2 (3.36 Å), N1 experiences stronger interaction with chloride. This preferential interaction stabilizes the bonding orbitals and shifts the anti-bonding orbitals to higher energy, resulting in the blue shift of the first peak in the N1 spectrum, compared with that of N2. The N3 spectrum exhibits unique features: an even lower energy peak A and strong resonances at 403.4 eV, which is roughly the same energy as peak B in the spectrum of the solvated free Gdm^+ pair. Being a nitrogen coordinated by two chlorides that associate with other Gdm^+ ions in the same plane, the LUMO and LUMO+1 of N3 are delocalized states extending through the chain-like structure shown in the bottom of Figure 21. This delocalization shifts the resonance to a lower energy, as explained above. The strong resonance at 403.4 eV originates from the 1s → LUMO+2 state of bare Gdm^+ ($p\sigma^*(NH_2)$) also extends throughout the Gdm^+-Cl^- chain, lowering the energy. In comparison, the spectrum of bare Gdm^+ exhibits no delocalization, and peak A and B are then blue shifted compared to the solvated free pair.

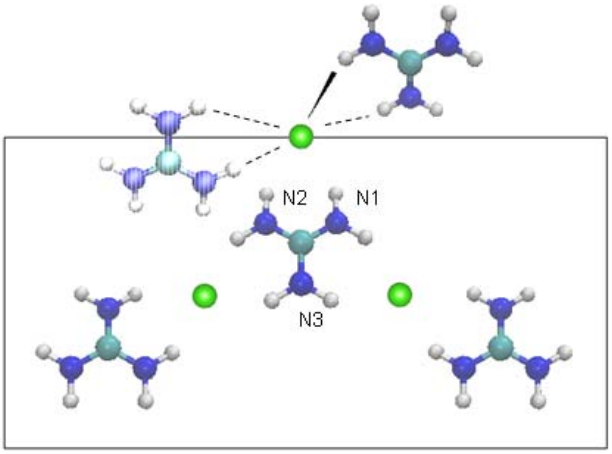

Figure 21. Arrangement of the guanidinium and chloride ions in the crystal. The three lower guanidinium ions and three chloride ions (green) are in the same plane, the top chloride coordinates with the top two guanidinium ions, which are not in the same plane.

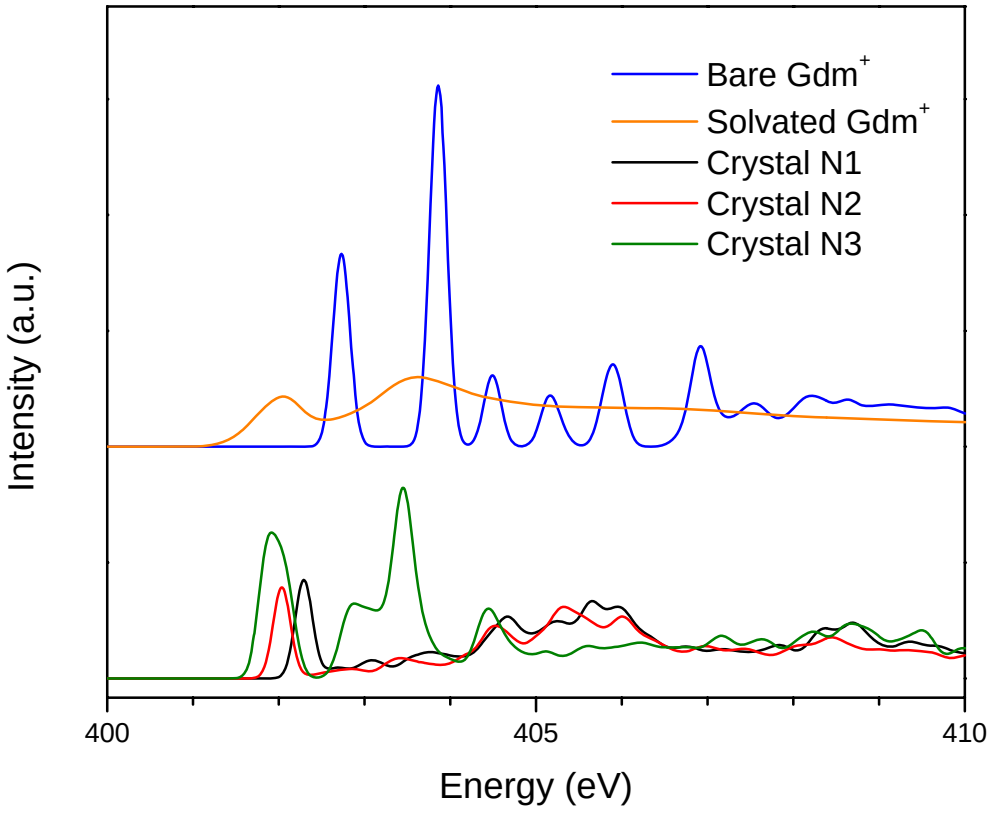

Figure 22. Calculated spectra due to individual nitrogen atom excitation in crystalline guanidinium chloride, compared with calculated spectra of an isolated guanidinium ion and a solvated guanidinium free pair. All spectra are processed with energy alignment but without intensity normalization.

3.5 Conclusions and Future Work

We have measured the nitrogen K-edge NEXAFS spectra of aqueous ammonium chloride and ammonium sulfate at various concentrations and observed spectral fingerprints with sensitivity to concentration that match with calculations. Electronic structure analysis reveals that the observed increase in intensity of the shoulder peak with increasing concentrations reflects symmetry breaking induced by pairing of ammonium and chloride at the tetrahedral corner site, i.e. it acts as a direct probe of interaction between ammonium and anions. The similar study of guanidinium chloride solutions shows that the first group of K-shell resonances are dominated by the π^* feature and are red-shifted due to π^* delocalized system mixing at high concentrations. The second group of resonances reflects interactions with the water hydrogen bonding network, and reveals an increasing tendency to form like-charged guanidinium-guanidinium contact pairs with increasing concentration. The results presented here demonstrate the sensitivity of our XAS experiments and associated XCH electronic structure analysis for probing such weak cation-cation interactions. The overcoming of repulsive Coulomb forces between two cations to form a stable contact pair in water further supports the Law of Matching Water Affinities and perhaps indicates a related mechanism for protein unfolding induced by guanidinium salts. Future studies will focus on the association of guanidinium with polypeptide systems and clarification of this mechanisms.

3.6 References

[1] Hofmeister, F. *Arch Exp Pathol Pharmakol* **1888**, *24*, 247-260.
[2] Berg, J. M; Tymoczko, J. L.; Stryer, L. *Biochemistry*; W. H. Freeman: New York, 2002.
[3] Collins, K. D. *Biophys J.* **1997**, *72*, 65-76.
[4] Collins, K. D. *Methods* **2004**, *34*, 300-311.
[5] Svedberg, T. *Nature* **1937**, *139*, 1051-1062.
[6] Dempsey, C. E.; Piggot, T. J.; Mason, P. E. *Biochemistry* **2005**, *44*, 775-781.
[7] No. K. T.; Nam, K. Y.; Scheraga, H. A. *J. Am. Chem. Soc.* **1997**, *119*, 12917-12922.
[8] Vondrasek, J.; Mason, P. E.; Heyda, J.; Collins, K. D.; Jungwirth, P. *J. Phys. Chem. B* **2009**, *113*, 9041−9045.
[9] Boudon, S.; Wipff, G.; Maigret, B. *J. Phys. Chem.* **1990**, *94*, 6056-6061.
[10] Mason, P. E.; Neilson, G. W.; Enderby, J. E.; Saboungi, M. L.; Dempsey, C. E.; MacKerell, A. D., Jr.; Brady, J. W. *J. Am. Chem.Soc.*, **2004**, *126*, 11462–11470.
[11] Soetens, J. C.; Millot, C.; Chipot, C.; Jansen, G.; Angyan, J. G.; Maigret, B. *J. Phys. Chem. B* **1997**, *101*, 10910-10917.
[12] Vazdar, M.; Vymetal, J.; Heyda, J.; Vondrasek, J.; Jungwirth, P. *J. Phys. Chem A* **2011**, *115*, 11193-11201.
[13] Weiss, A. K. H.; Hofer, T. S.; Randolf, B. R.; Rode, B. M. *Phys. Chem. Chem. Phys.* **2012**, *14*, 7012-7027.
[14] Hunger, J.; Niedermayer, S.; Buchner, R.; Hefter, G. *J. Phys. Chem. B* **2010**, *114*, 13617-13627.
[15] Kubickova, A.; Krizek, T.; Coufal, P.; Wernersson, E.; Heyda, J.; Jungwirth, P. *J. Phys. Chem. Lett.* **2011**, *2*, 1387-1389.

[16] Mason, P. E.; Neilson, G. W.; Dempsey, C. E.; Barnes, A. C.; Cruickshank, J. M. *PNAS* **2003**, *100*, 4557-4561.
[17] Wilson, K. R.; Rude, B. S.; Smith, J.; Cappa, C. D.; Co, D. T.; Schaller, R. D.; Larsson, M.; Catalano, T.; Saykally, R. J. *Rev. Sci. Instrum.* **2004**, *75*, 725-736.
[18] Aziz, E. F.; Zimina, A.; Freiwald, M.; Eisebitt, S.; Eberhardt, W. *J. Chem. Phys.* **2006**, *124*, 114502.
[19] Uejio, J. S.; Schwartz, C. P.; Duffin, A. M.; Drisdell, W. S.; Cohen, R. C.; Saykally, R. J. *PNAS* **2008**, *105*, 6809-6812.
[20] Prendergast, D.; Galli, G. *Physical Review Letters* **2006**, *96*, 215502.
[21] Schwartz, C. P.; Uejio, J. S.; Saykally, R. J.; Prendergast, D. *J. Chem. Phys.* **2009**, *130*, 184109-184120.
[22] Uejio, J. S.; Schwartz, C. P.; Saykally, R. J.; Prendergast, D. *Chem. Phys. Lett.* **2008**, *467*, 195-199.
[23] Giannozzi, P. *et al. Journal of Physics. Condensed matter* **2009**, *21*, 395502.
[24] Perdew, J. P.; Burke, K.; Ernzerhof, M. *Phys. Rev. Lett.* **1996**, *77*, 3865-3868.
[25] England, A. H.; Duffin, A. M.; Schwartz, C. P.; Uejio, J. S.; Prendergast, D.; Saykally, R. J. *Chem. Phys. Letters* **2011**, *514*, 187-195.
[26] Gilbert, A. T. B.; Besley, N. A.; Gill, P. M. W. *J. Phys.Chem. A* **2008**, *112*, 13164-13171.
[27] Besley, N. A.; Gillbert, A. T. B.; Gill, P. M. W. *J. Chem. Phys.* **2009**, *130*, 124308.
[28] Shao, Y. *et. al.* Phys. Chem. Chem. Phys. 2006, 8, 3172-3191.
[29] Plashkevych, O.; Yang, L.; Vahtras, O.; Agren, H.; Pettersson, L. G. M. *Chem. Phys.* **1997**, *222*, 125-137.
[30] Guerra, A. C. O.; Ferreira, G. B.; Machado, S. P.; Turci, C. C. *Int. J. Quantum Chem.* **2008**, *108*, 2340-2357.
[31] Duflot, D.; Flament, J. P.; Giuliani, A.; Heinesch, J.; Grogna, M.; Hubin-Franskin, M. J. *Phys. Rev. A* **2007**, *75*, 052719.
[32] Turci, C. C.; Urquhart, S. G.; Hitchcock, A. P. *Can. J. Chem.* **1996**, *74*, 851-869.
[33] (a) Pace, C. N. *Methods Enzymol.* **1986**, *131*, 266-280. (b) Mason, P. E.; Neilson, G. W.; Dempsy, C. E.; Barnes, A. C.; Cruickshank, J. M. *Proc. Acad. Acad. Sci. U.S.A.* **2003**, *100*, 4557-4561. (c) Timasheff, S. N. *Biochemistry* **1992**, *31*, 9857-9864. (d) O'Brien, E.P.; Dima, R. I.; Brooks, B.; Thirumalai, D. *J. Am. Chem. Soc.* **2007**, *129*, 7346-7353. (e) Mountain, R. D.; Thirumalai, D. *J. Phys. Chem. B* **2004**, *108*, 19711-19716.
[34] Scott, J. N.; Nucci, N. V.; Vanderkooi, J. M. *J. Phys. Chem. A* **2008**, *112*, 10939-10948.
[35] Haas, D. J.; Harris, D. R.; Mills, H. H. *Acta Cryst*. **1965**, *19*, 676-679.

Chapter 4 : Exploring New Directions in NEXAFS – Seeking Surface Sensitivity

4.1 Introduction

The characterization of chemical environments on liquid surfaces is an important subject essential to diverse fields, including biology, catalysis, energy conversion, and atmospheric chemistry. The combination of XAS and liquid microjets allows convenient introduction of volatile liquid samples into high vacuum and provides a clean, continuously replenished liquid surface for direct interrogation of the molecular scale structure. Previously, our group has presented total ion yield (TIY) and total electron yield (TEY) x-ray absorption spectroscopy (XAS) measurements and calculations on liquid and gas phase water.[1,2] In contrast to TEY-XAS, which is a bulk probe, TIY-XAS is often thought to be more sensitive to the electronic structure of the surface because of the shallow escape depth (<5 Å) of ions from the condensed phases.[3] However, the observed TIY-XAS spectrum of water is nearly identical to the TEY-XAS spectrum, resulting from large contributions from x-ray induced electron stimulated desorption of ions, i.e., the electrons from the bulk liquid ionize the surface molecules and the vapor phase around the jet and thereby generate ions that being detected. Therefore, the TIY spectrum of highly volatile liquids does not generally provide unique information about the liquid surface. Although clear differences were observed in the EXAFS oscillations between measured liquid-phase TEY and TIY spectra for water,[4] the influence of having a significant vapor phase and x-ray induced ion desorption contribution to the EXAFS spectrum need to be considered before definitive conclusions can be drawn regarding the application of TIY for enhanced surface sensitivity measurements of condensed phases. The previous studies[1,2] focus on the detailed microscopic structure of liquid water surface. Instead of focusing on the solvent, in this chapter, I revisit the possibility of achieving surface sensitivity of TIY detection relative to TEY by studying surface active salt solutions (potassium thiocyanate and potassium acetate)[5] compared with potassium carbonate, which has lower surface affinity.

Novel detection methods were explored to eliminate vapor interferences for solutions with higher vapor pressure. Previously measured liquid phase XAS spectra of hexane were similar to the gas phase spectrum, demonstrating the unsuitability of traditional TEY method with hexane (or other higher vapor pressure liquids). In this chapter, I introduce the new "downstream" detection method, which measures the electrical current from positive ions impinging on a conducting target placed downstream of the jet after all excited electrons from the jet are collected with the biasing electrode. A related new detection scheme is called "upstream" detection, wherein a metal capillary is used to generate the microjets, and a wire is attached onto the metal tip itself (i.e. before the liquid jet,) to measure the back conduction of the positive ions, thereby avoiding the need to place a collecting electrode in the downstream path of the jet. These two detection methods not only provide new capabilities for obtaining pure liquid phase signals, but also may permit enhanced surface sensitivity, since the metal tip is in direct contact with the liquid and the probing depth could possibly be manipulated by changing the bias

voltage.

4.2 Experimental Methods

Downstream and Upstream Detection

The same liquid jet XAS endstation set-up[6] was used as previously described for ion-pairing study in Chapter 3. Liquid sample was loaded into the syringe pumps (Teledyne-Isco) and flowed through a 30 μm fused silica capillary to generate the liquid microjet. It was then intersected by the x-ray beam at Beamline 8.0.1 at the Advanced Light Source at Lawrence Berkeley National Laboratory. The biased copper electrode used for TEY detection was kept in its original place, but for preliminary trials of downstream detection, a piece of aluminum foil was introduced downstream of the microjet to collect the positive ions remaining in the jet. This foil was placed in front of the liquid nitrogen trap, collecting the liquid ~3 feet downstream from the jet tip, as shown in Figure 1. The foil was taped onto a plastic plate to keep it electronically isolated from the chamber, and mounted on an adjustable rod. A simple alligator clip was used to connect the foil to an electrical feedthrough. The signal was amplified by a current amplifier (model DDPCA-300, with a low-pass filter to improve the signal-to-noise ratio.) and then sent to the beamline data collection computers. Compared to the TEY signal, the current output from downstream detection is inverted and requires the opposite polarity setting on the voltage to frequency controller. All scans were normalized to the I-zero current measured from the beamline gold mesh detector. Subsequent modifications of downstream detection include changing the target material first to a copper plate and then a copper cup to ensure that all the charged liquid could be captured. We also incorporated flexible AC/DC heater taping onto the back of the target to avoid liquid freezing. Note that for water scans, a millimolar NaCl is added to the solution to suppress the intrinsic electrokinetic current.

A similar detection method transcending freezing and jet positioning issues, the "upstream" detection method, was also developed and tested. Instead of the typical fused silica capillaries, a metal capillary (50 μm, purchased from New Objective) was used to create the microjet. A wire was wrapped around this metal capillary, and connected to a picoammeter. The TEY-detecting electrode is still in place with a normal positive bias voltage (2.1kV), and the signal from the metal tip is proportional to back conduction of the ionized molecules after the X-ray absorption processes. With this setup, the TEY and upstream signal can be measured simultaneously. n-Nonane and n-Decane solutions were measured, and both on-jet and off-jet signal were collected.

TEY vs. TIY Detection – Surface Sensitivity Test

Electrons or ions emitted from a material by photon or electron excitation probe different regions of a sample, determined by the relative escape depths of these particles.[7] TEY measurements are dominated by a secondary electron cascade which escapes into vacuum from an average depth of 20 Å, thereby probing many mono-layers (bulk probe). In contrast, ions desorb directly from the interface so TIY detection is generally thought to provide a measure of the electronic structure of the outermost surface layer (1-5 Å).[8] Ions are produced by populating repulsive final states or depopulating bonding molecular orbitals via Auger decay. Desorption from the surface is then mediated by a Coulomb

explosion mechanism. This phenomenon, generally known as direct photon stimulated ion desorption (PSID), has been extensively characterized for monolayer adsorbates as well as condensed-phase systems.[9] A bias voltage of +312 V is used for TEY detection and -312 V is used for TIY detection. Potassium thiocyanate, potassium carbonate and potassium acetate with quoted purity >99% were purchased from Sigma-Aldrich and used without further purification. Various concentrated solutions were prepared with Millipore water (18 MΩ). All presented spectra are normalized to the beamline I-zero current, and then peak-normalized to the first potassium L-edge resonance at 295.1 eV. The ideal normalization to the potassium resonances would be area normalization – integration of the area under the two L-edge resonances should be the same. However, the weak signal and drift in the baseline in TIY spectra make area normalization problematic

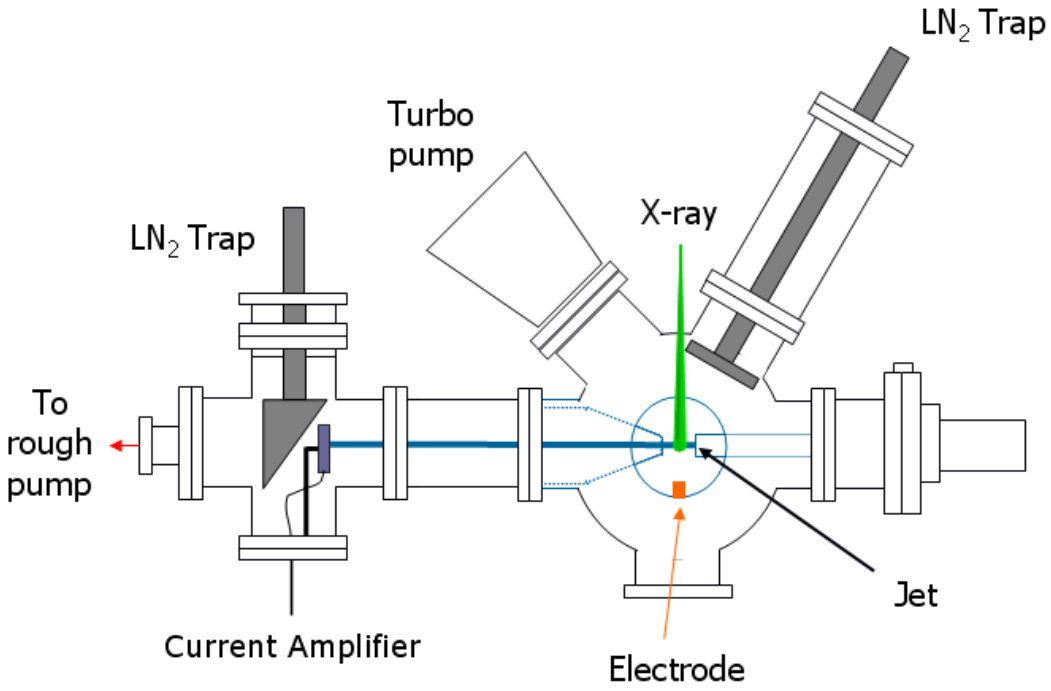

Figure 1. Experimental diagram of the modified liquid jet XAS endstation with downstream detection. A piece of aluminum foil placed downstream of the jet measured the positive current as a function of x-ray energy, collecting the liquid-phase only signal. The foil is taped on a plastic place to ensure electronic isolation from the chamber.

4.3 Results and Discussion

Downstream and Upstream Detection

A nanoampere positive current was measured by the downstream current detection of a water liquid microjet. The small current is due to the long distance between the jet tip and the foil target, plus the instability of the jet. Oxygen K-edge spectra were recorded

for water and compared with TEY results to determine if this downstream detection could be a viable probe of pure liquid-phase signal (without gas phase contamination). Figure 2 displays the on-jet TEY (top), initial trial of downstream detection using a foil target (middle) and the following downstream trial spectra with a copper target (bottom). The original TEY detection for water produces spectra with good signal-to-noise ratio, but still have vapor signal contribution evidenced by the small feature at 536 eV. Downstream detection with a foil target resulted in a similar on-jet spectra without interference from vapor signal at 536 eV, although noisier, while the off-jet spectra showed no significant signal, evidencing a highly selective probe for obtaining pure liquid signal. The later trials using copper targets resulted in similar spectra to those measured from aluminum foil. Thus the signal was not sensitive to the target material or the surface flatness.

There are two major drawbacks with the downstream detection. First, some jets spray more so the plate can't capture all the liquid. This was addressed by using a copper cup as the target; however, the copper cup failed due to the second drawback: liquid freezing on the target. With this setup the current could be measured only in the first ~40 minutes after pumping down the chamber, and even shorter for the copper target because of the smaller specific heat. To deal with freezing issue, we taped a flexible AC heater onto the back of the aluminum foil and a thermocouple on the foil so that the real-time temperature could be monitored. Figure 3 shows the resulting spectra taken under different temperature settings. The spectral shape was hard to discern for lower temperature scan (15℃); when moving to higher temperature, the pre-edge features at 532.5 eV and higher energy resonances could be recognized, but with a poor signal-to-noise ratio possibly due to pickup from AC flowing through the heater. We've also tried DC heating but it turns out that the liquid sample would form a layer on the target, resulting in loss of signal. Therefore, a new detection scheme called "upstream" detection was designed to avoid the jet freezing issue and at the same time obtain pure-liquid phase spectrum by measuring the back-conduction using a metal capillary.

As can be seen in Figure 4, the background gas-phase signal is greatly reduced in the upstream-detected spectra compared with the TEY off-jet spectra. But unlike the downstream detection which totally eliminates the gas phase signal, there is still a small vapor contribution in the upstream off-jet scan. However, the signal-to-noise ratio was better for the on-jet upstream detection relative to downstream detection because there were no jet-freezing problems or alignment issues. The closely matching on-jet data and strong signal from upstream detection encouraged us to test the upstream detection on the long-chain hydrocarbon systems, for which the liquid phase spectra collected in earlier runs using TEY appeared identical to gas phase spectra. Snce with upstream detection, the liquid sample is in direct contact with the metal tip, the spectra collected should be dominated by the liquid phase signal.

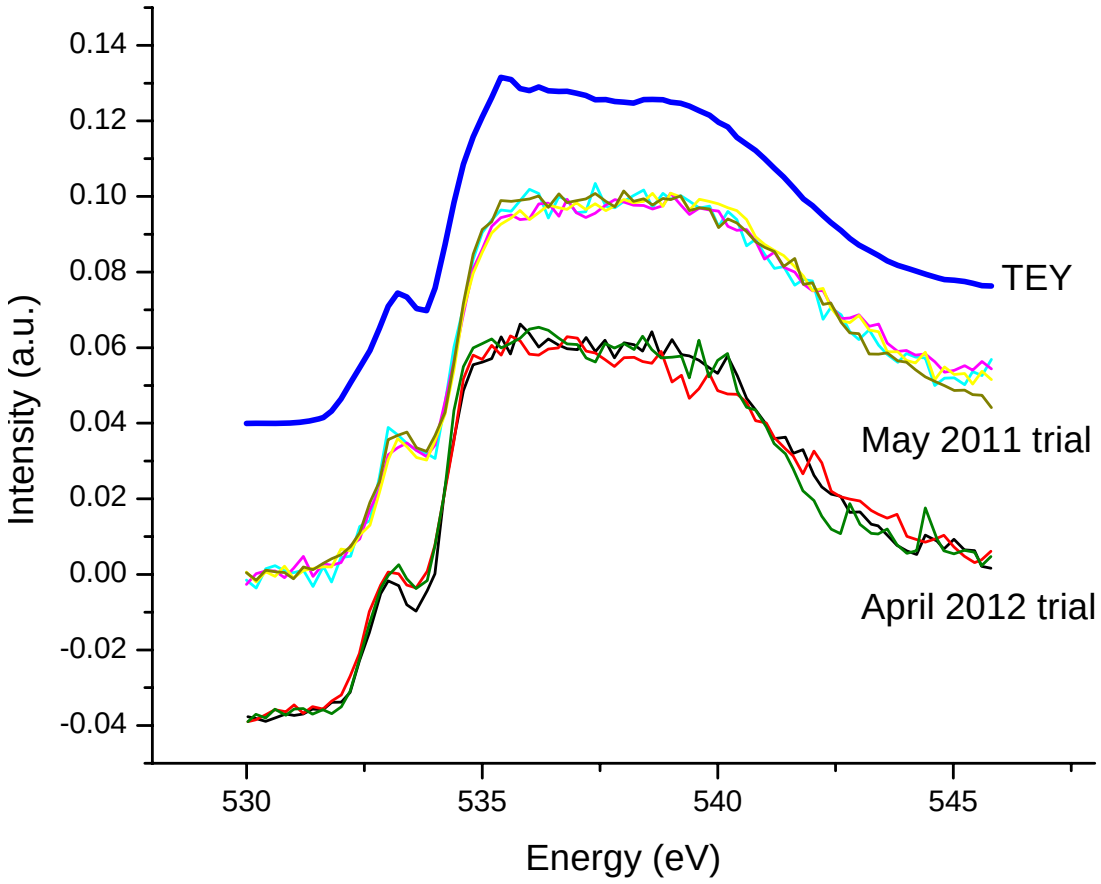

Figure 2. On-jet oxygen K-edge spectra of millimolar NaCl in water measured by TEY (top), by downstream detection with an aluminum foil target (middle, data from May 2011), and downstream detection with a copper plate target (bottom, data from April 2012). All spectra are single scans and area normalized.

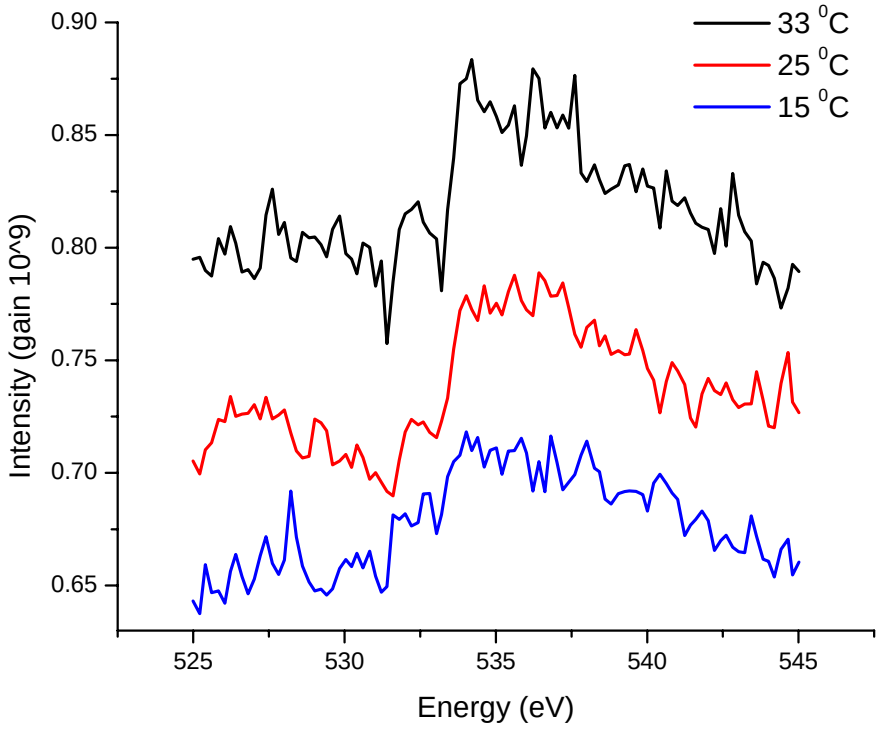

Figure 3. On-jet oxygen K-edge spectra of millimolar NaCl in water measured by downstream detection with a flexible sheet of AC heaters attached on the back of the aluminum foil target in order to avoid jet freezing on the target. The temperatures are measured by a thermocouple placed on the foil.

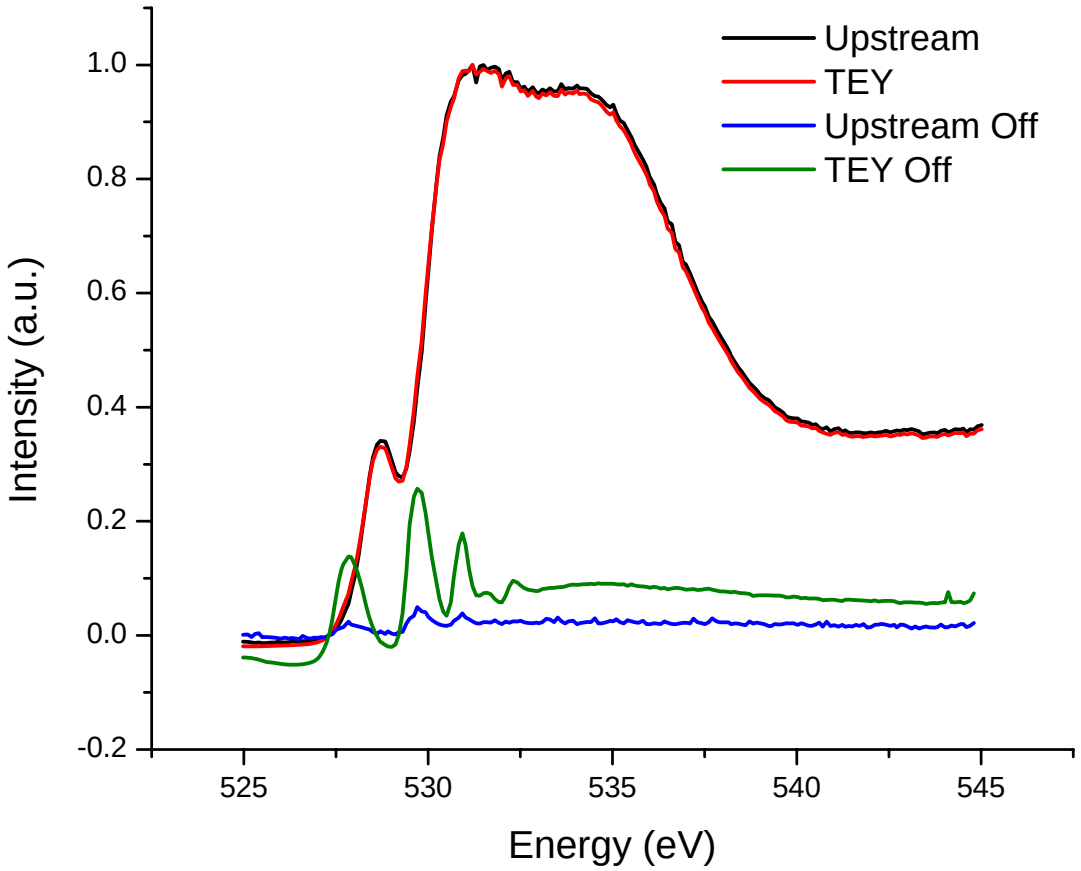

Figure 4. Comparison of on-jet and off-jet oxygen K-edge spectra of water (with milimolar NaCl) for TEY and upstream detection. The upstream signals are measured from back-conduction onto the metal capillary used for generating liquid jets. Upstream and TEY on-jet spectra (black and red, respectively) are peak normalized at 531.2 eV, whereas the off-jet data shown (blue and green) are the raw data, showing different levels of gas phase signal contribution.

Figure 5 presents spectra of TEY and upstream-detected nonane at the carbon K-edge. In the upstream on-jet spectrum, there are sharp resonances at 285.0 and 285.7 eV, respectively, marked as resonances A and B. These are then followed by a broad group of resonances centered at 290 eV (peak C in Figure 5) with a lower energy side shoulder at 287.5 eV. The TEY on-jet spectrum showed a broader pre-edge feature for both A and B but a narrower peak C (Figure 5(a)). Comparison between the TEY on-jet and TEY off-jet data further exhibits the sensitivity of peak C for different phases: TEY off-jet spectra showed clear reduction of the peak width of feature C, as shown in Figure 5(b). Also peak C in the upstream on-jet spectrum is significantly broader than in both the TEY and the TEY off-jet spectra, indicating the reduced gas phase signal in the upstream detection. However, the upstream on-jet and off-jet spectra appear to be similar and the raw signals were of the same order of magnitude, which implies that either the upstream detection method can't eliminate the gas phase signal contribution or the intrinsic issue of the hydrocarbon jet.

There are some new concerns when measuring liquid hydrocarbon molecules; first, instabilities arise in the jet due to the build up of charges induced by either the x-rays or electrokinetic charge separation. This results in a Coulomb explosion in the jet, breaking up the stream into smaller droplets. Thus, there is a high vapor pressure "cloud" around the liquid jet even though the vapor pressure of both nonane and decane are lower than that of water. When collecting data on the long-chain hydrocarbon system, we were unable to use the typical 2.1 kV bias that has usually been used for TEY detection because of electrical breakdown in the high pressure environment. Note that it's only the jet surroundings affected by the vapor cloud, so the current in the nearby electrode was overloading although the chamber ion-gauge still read low pressure ($\sim 2 \times 10^{-4}$ torr). Therefore, we used a 10V internal bias from the picoammeter instead of the 2.1 kV battery box. With this small bias, when taking an off-jet spectrum the electrons ejected from the vapor are essentially free. There is a chance that some electrons travel back to the liquid jet and generate a signal that can be measured from upstream detection, resulting in gas-phase signal interferences. The sharpness of resonances A and B in upstream on-jet spectra relative to TEY on-jet spectra created more ambiguity about whether or not the upstream detection actually probes the liquid-only signal, since it exceeds the scale of a typical line width in a solvent system.

The results of same upstream detection tests with decane are shown in Figure 6. The overall spectral shapes are similar to those of nonane, as expected: two pre-edge features A and B, following by C, a broad group of transitions with lower energy shoulder. The broadening of peak C is still observed in the upstream spectrum. Peak C is slightly narrower in the TEY spectrum and still narrower (by 2.1 eV in FWHM) in the TEY off-jet spectrum, indicating a more liquid-like signal with upstream detection. However, the broadening of peaks A and B in the TEY on-jet scan also appeared, albeit with a lesser extent if compare between Figure 5(a) and Figure 6(a), possibly due to the lower vapor pressure of decane.

The significant differences observed in the present study between TEY on-jet and TEY off-jet spectra of long chain hydrocarbons were unexpected, since the previous study by our group showed gas-phase like liquid spectrua (on-jet). Here we observed narrower spectral features A, B and C in both Figure 5(b) and 6(b) and a small red shift of peak C in TEY off-jet spectra relative to the TEY on-jet spectrum. The only experimental change made since the earlier study was in the design of the nozzle. The 50 μm metal jet used here has a larger diameter, and thus lower background electrokinetic current, than observed with the smaller (25 micron diameter). Pt/Ir electron microscope apertures used before. The higher jet velocities obtained with these smaller jets lead to higher electrokinetic charging, resulting in a higher degree of Coulomb explosion, and thus create more sprays of the jet so that there boundary between gas and liquid phases becomes blurred. Also, the metal jet used in this study is grounded, whereas the electron microscope orifices were allowed to float. This might be the reason why we see differences in TEY for on and off-jet spectra with upstream detection, and the different flow profiles might have some effects, too.

Preliminary simulations of the K-shell spectrum were preformed for gaseous nonane using the XCH code introduced in Chapter 3 and are shown in Figure 7, where the "liquid-like" upstream spectrum and TEY off-jet spectrum are also shown for comparison. The simulated spectrum reproduces the peak height and energy of resonances A and B

very well, however, the energy of the center of predicted peak C is 291.4 eV, 1 eV lower than that of the observed upstream spectrum. The shoulder on the lower energy side of peak C was reproduced and red-shifted in the simulated spectrum as well. One of the major weaknesses of DFT in predicting water K-shell spectra- underestimating the water band gap is not a problem here, so no stretching of the energy axis to match the experimental data is needed. The width of predicted peak C is comparable to the TEY off-jet data, showing a gas-like signal. Figure 8 shows the isosurfaces of the center-carbon core-hole excited states with its stick spectrum. Resonance A consists of only one transition: 1s→LUMO, a σ* state. Resonance B actually comprises of two transitions, a strong 1s→ π*-like transition and a much weaker higher-order delocalized σ* transition. Resonance C comprises a number of delocalized transitions, dominated by those having higher π-projections onto the center carbon 1s orbital. These delocalized states would be sensitive to the surrounding environments. Although not very obvious, in nonane and decane spectra (Figure 5(a) and 6(a)), peak C in the TEY on-jet spectrum is red shifted from the upstream detection spectrum. Compared to the calculations, which show that the gas phase signal would occur at lower energy than the observed value, this red shift may result from a higher gas-phase signal contribution in TEY. Detailed calculations and electronic structure analysis on these liquid phase hydrocarbons are necessary for a further understanding of this interesting spectral variation.

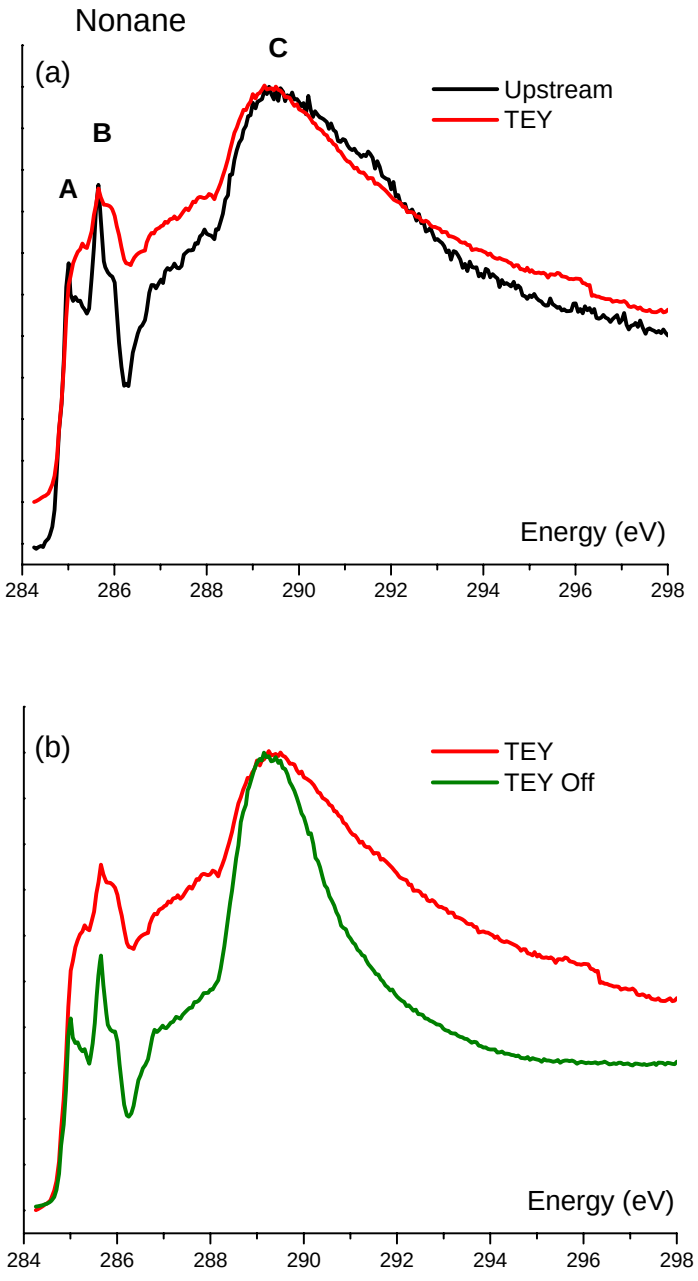

Figure 5. Comparison of on-jet and off-jet carbon K-edge XAS spectra of nonane for TEY and upstream detection. The TEY and upstream data were measured simultaneously with a 10 V internal bias from the picoammeter. The two sharp pre-edge features are labeled as resonances A and B. The higher energy broad band is marked as peak C. All spectra are peak-normalized to the highest point of its peak C.

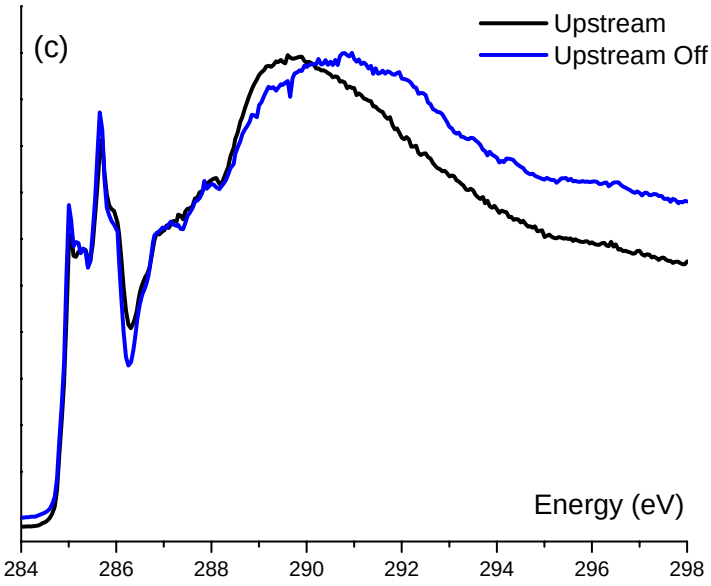

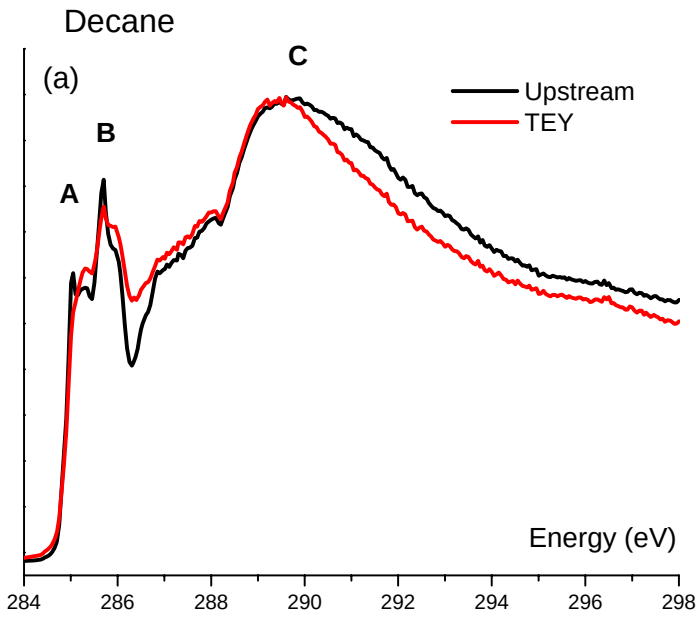

Figure 6. Comparison of on-jet and off-jet carbon K-edge XAS spectra of decane for TEY and upstream detection. The two sharp pre-edge features are labeled as resonances A and B. The higher energy broad band is marked as peak C. All spectra are peak-normalized to the highest point of its peak C.

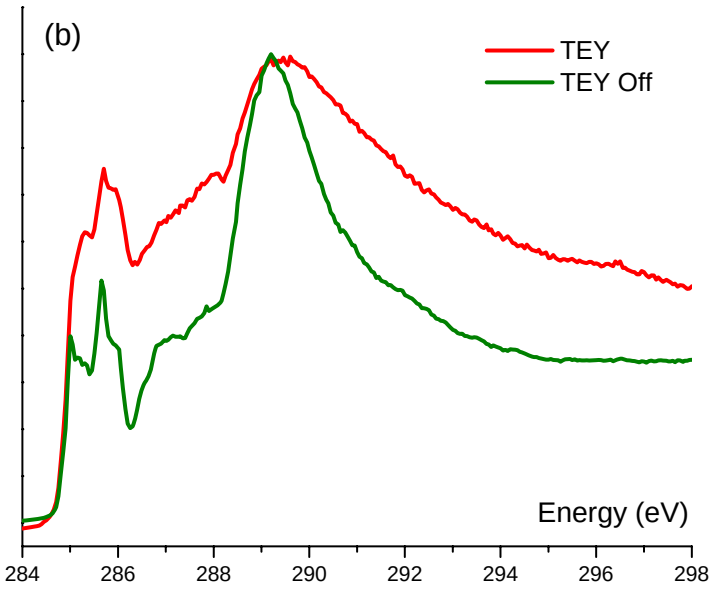
(b)
TEY
TEY Off
Energy (eV)
284
286
288
290
292
294
296
298

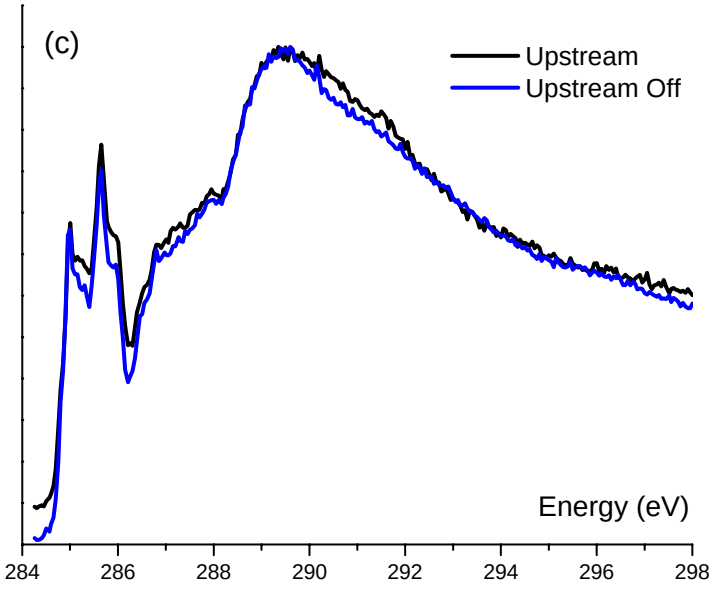
(c)
Upstream
Upstream Off
Energy (eV)
284
286
288
290
292
294
296
298

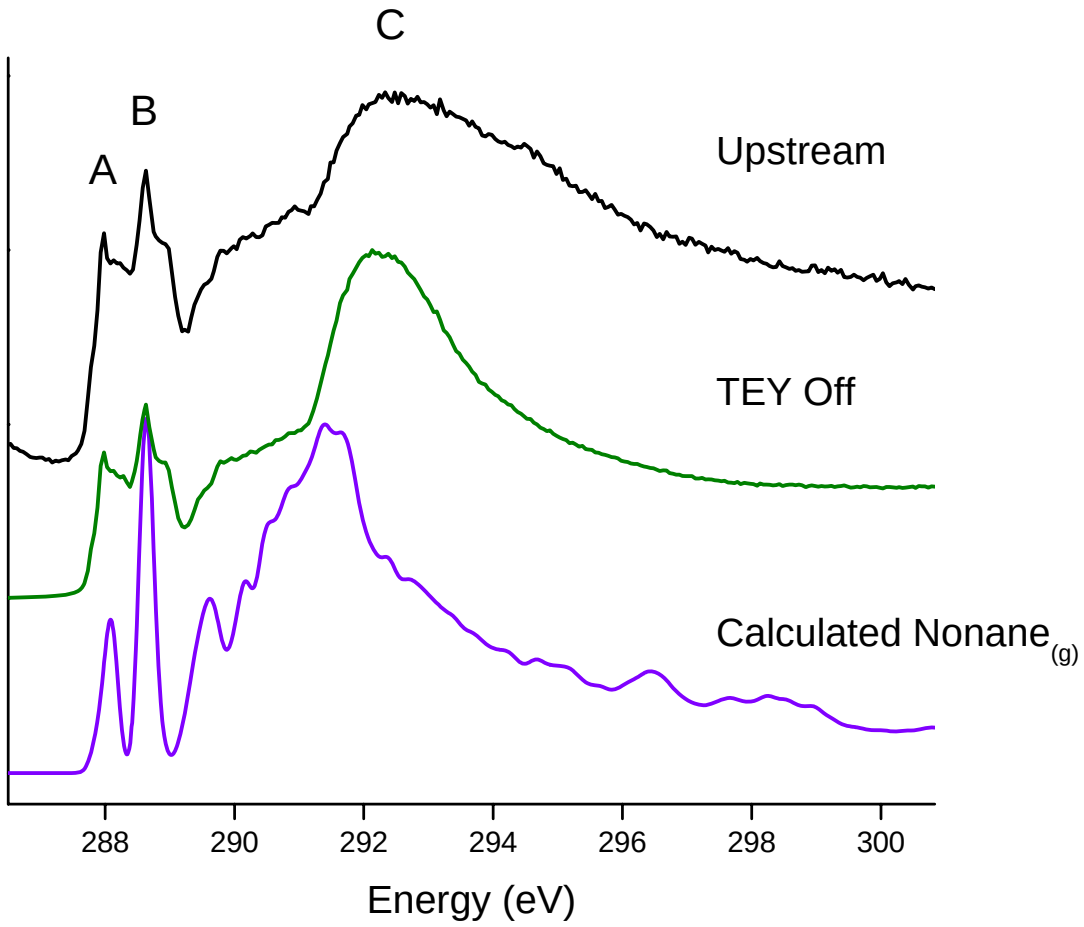

Figure 7. Comparison of calculated gaseous nonane carbon K-edge XAS spectra and experimental spectra measured by upstream detection (on-jet) and the traditional TEY method (off-jet). The calculated spectrum is an average of all nine individual carbon excitation spectra, energy aligned by the atomic alignment scheme discussed previously.[10] All spectra shown are peak normalized to the highest point of its peak C.

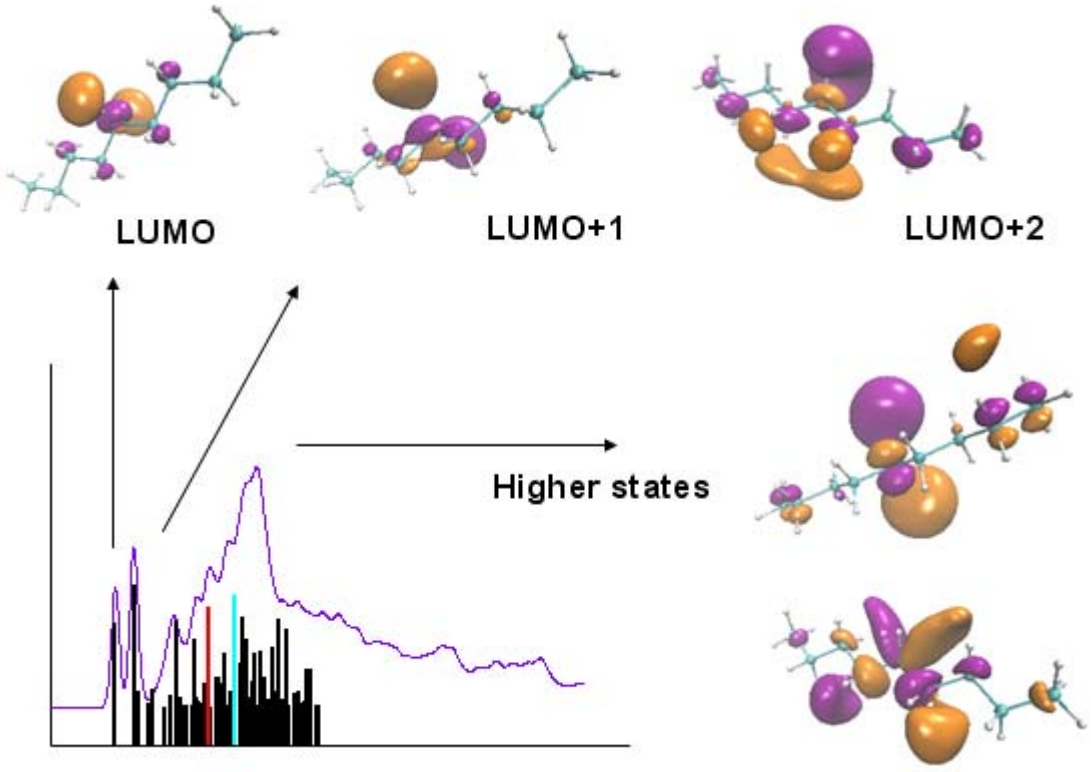

Figure 8. Calculated XAS spectrum of gaseous nonane from excitation of the central carbon (C5) with its corresponding stick spectrum and isosurfaces (15%). The LUMO state (σ*) and LUMO+1 (π*-like) are more localized compared to the higher states. Only two isosurfaces of the strongest resonances in peak C are shown, marked by the red (upper isosurface) and light blue (lower isosurface) sticks.

TEY and TIY Detection – Surface Sensitivity Test

Figure 9 shows the TEY and TIY spectra of 1.25M KSCN solutions at the carbon K-edge and potassium L-edge. The TIY spectrum is noisier due to the lower detected current. Given that the relative escape depths of ions and electrons are very different (< 5 Å and average of 20 Å for ions and electrons, respectively), the liquid volume probed by the TEY is ~50 times larger than that probed by the TIY; as a consequence, the observed difference in the current measured by TEY versus TIY is expected. Instead of area normalization, all spectra were peak normalized to the first resonance at the potassium L-edge at 297.0 eV due to the baseline drift at higher energies in TIY spectra. Since we expect thiocyanate to be enhanced at the interface[5] and potassium to be buried in the bulk[11,12], after normalization to potassium peak, if the TIY detection were more surface selective than TEY, a higher signal for the carbon π* resonance should be observed; otherwise the TIY detection is not really probing the surface. The TIY π* resonance at 287.2 eV actually has a 19.1 % increase in signal relative to the correspondingly normalized TEY signal, indeed evidencing enhanced surface sensitivity for TIY detection. Figure 10 plots the value of area of TIY π* resonance divided by area of TEY π* resonance, named as "TIY/TEY", versus concentrations, Similar data for the carbonate anion and the acetate anion are also shown for comparison. In the case of carbonate,

which is a strongly hydrated and very non-polarizable anion, which we would expect to be depleted from the surface, a lower TIY/TEY value was observed (average of 1.04) relative to that of thiocyanate (average of 1.21). For acetate anion, which has a partition coefficient of 1.30 derived from an air-water surface-bulk partitioning model developed to interpret the effects of ions on the surface tension of water.[11,12] The individual ion partition coefficients are defined as ratio of molar concentration of the ions in the surface and bulk regions. Since Na_2SO_4 is the most surface-excluded salt from their measurements, the ion partition coefficients K_p are defined relative to K_p (Na^+) = K_p (SO_4^{2-}) = 0. Based on their model and calculations, $K_p(SCN^-)$ = 1.64, which is strongly surface-accumulated; whereas $K_p(CO_3^{2-})$ = 0.22, which is modestly excluded from the surface, and acetate is weakly accumulated. Therefore, we would expect the TIY/TEY value for acetate anion to be in between 1.04 (carbonate) and 1.21 (thiocyanate). However, acetate anion yields a TIY/TEY value of 0.82 at lower concentrations, while at higher concentrations the TIY/TEY values are similar to that of carbonate within experimental error. Moreover, there are no trends with concentration dependence, establishing the selectivity of TIY detection for surface species clearly requires further study.

As an alternative way of pursuing surface sensitive detecting scheme, the KSCN solution were run on metal jet with the upstream detection method discussed above and compared with TEY spectrum, after the same normalization procedure the resulting spectra at the same energy range (Carbon K-edge and potassium L-edge) are shown in Figure 11. The intensity of upstream π^* resonance is 19.3% greater than that of TEY, indicating enhanced surface sensitivity in the upstream detection. Further experiments involve testing on potassium carbonate, potassium acetate and application of different bias voltage are needed to verify this sensitivity. Based on the good signal-to-noise ratio of the upstream KSCN data (compared to TIY data), there should be no problems testing with diluted solutions and lower bias voltages.

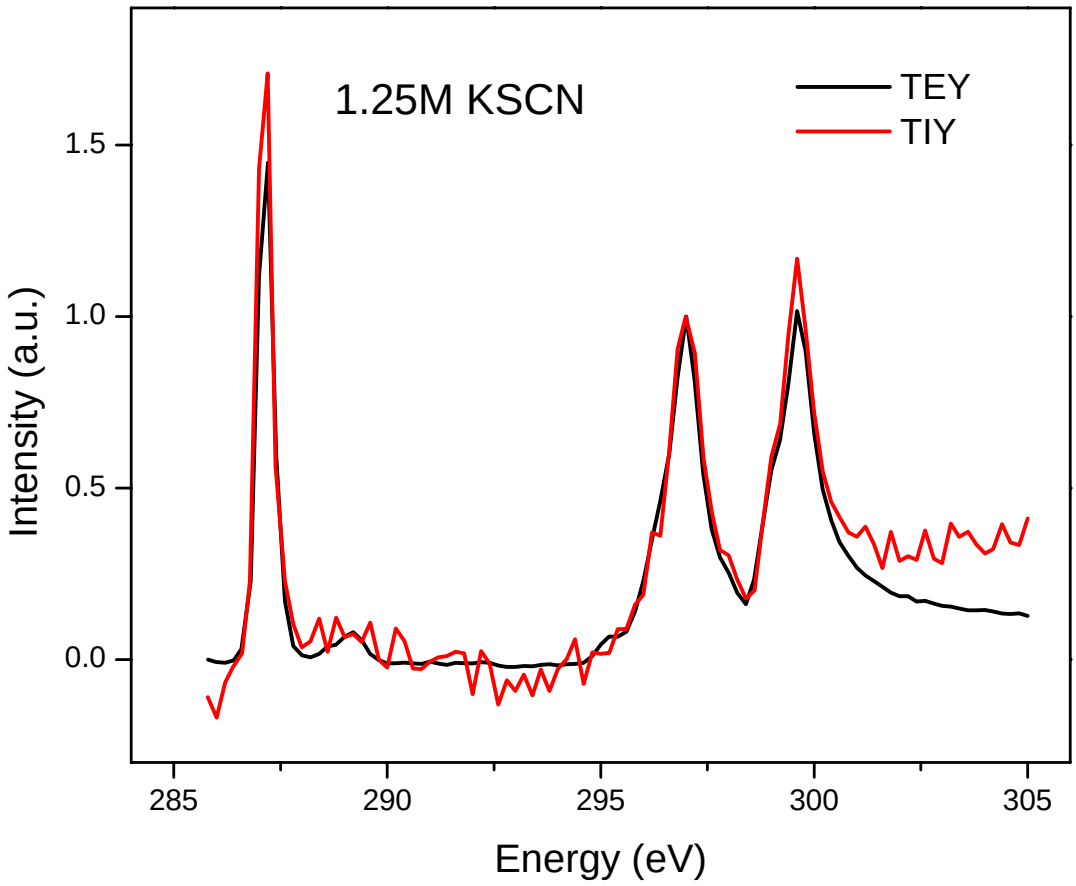

Figure 9. Carbon K-edge and potassium L-edge spectra of 1.25M potassium thiocyanate measured by TEY and TIY. The spectra are peak-normalized at the first potassium resonance at 297 eV, the bulk probe, and then the relative signal intensity of the carbon feature at 287.2 eV reflects the surface sensitivity.

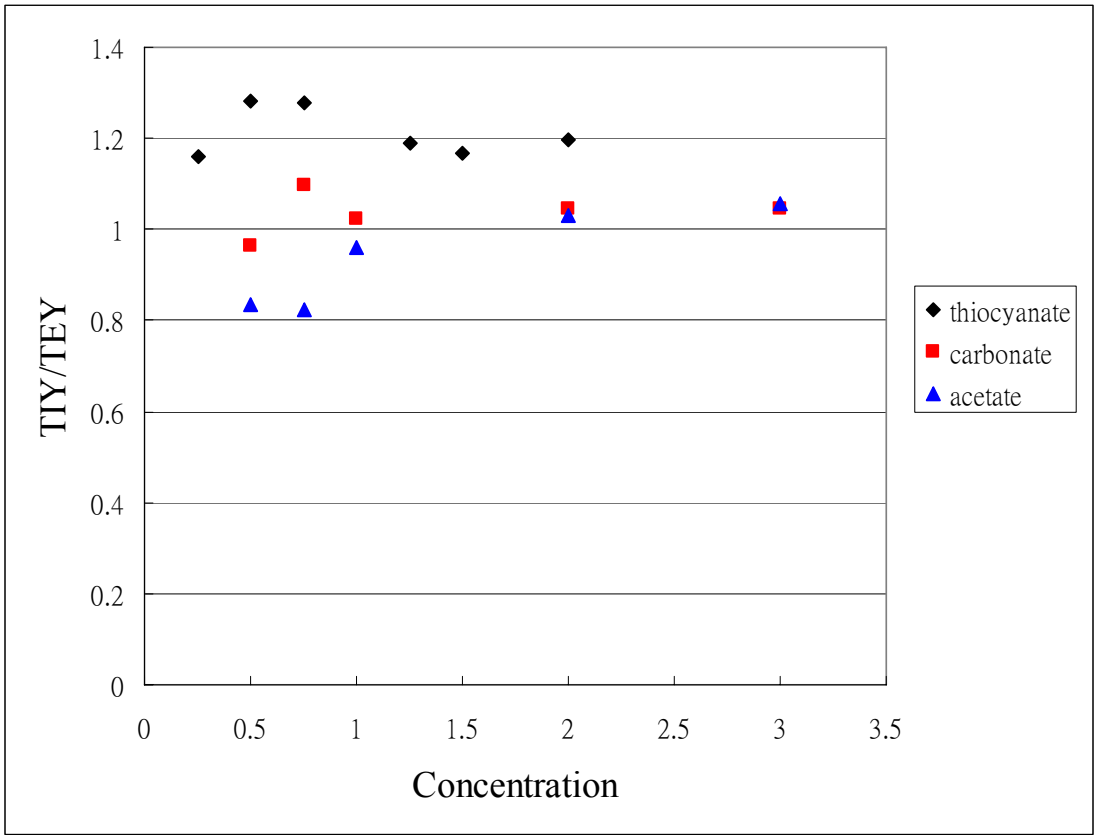

Figure 10. Plot of potassium thiocyanate TIY/TEY (the integrated signal intensity of carbon feature shown in Figure 9 measured by TIY divided by the intensity of the same peak measured by TEY. For a surface-depleted species, this value would be unity) versus concentration. Similar potassium carbonate and potassium acetate data are shown for comparison.

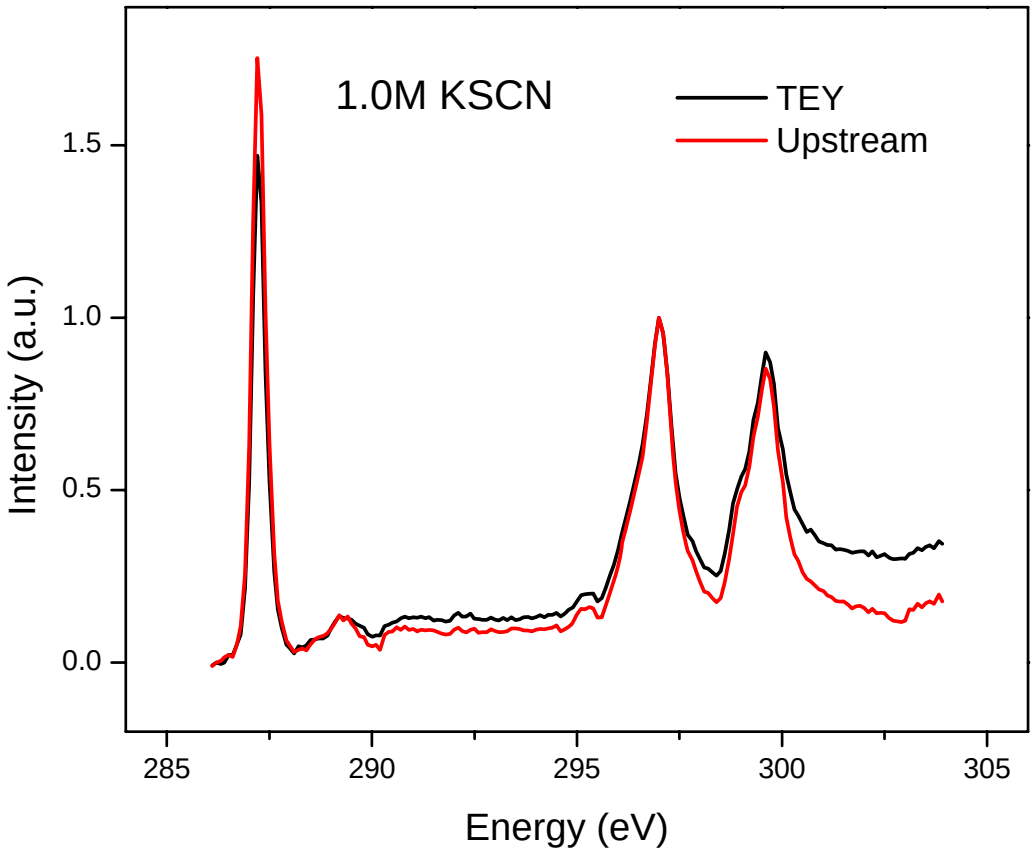

Figure 11. Carbon K-edge and potassium L-edge spectra of 1.0M potassium thiocyanate measured by TEY and upstream detection. The spectra are peak-normalized by the same scheme applied in Figure 9; the higher relative signal intensity of the carbon feature at 287.2 eV reflects the increased surface sensitivity of upstream detection.

4.4 Conclusions and Future Work

XAS spectra of liquid water were measured for the first time via the indirect downstream detection method. By measuring the current generated from the positive ions in the liquid jet, the vapor signal was greatly suppressed. However, the instability of this method due to jet freezing and having residual liquid on the target plate caused problems. Therefore, an alternative detection method – upstream detection was designed to avoid such jet issues. This was achieved by using a metal capillary as the jet nozzle and collecting the positive ion current directly from the capillary. The resulting upstream spectrum of water exhibits less vapor contribution than TEY detection and a signal-to-noise ratio comparable to that of TEY spectrum. Further tests of the upstream detection on long chain liquid hydrocarbons (nonane and decane) showed similar on-jet and off-jet upstream spectra ascribed to Coulomb explosion phenomena resulting from enhanced charge buildup inside these low dielectric liquid jets. But there were nevertheless observable differences in between TEY on-jet and off-jet spectra which were not observed in previous studies by our group. Future development of upstream detection for liquid jet XAS spectroscopy will involves testing with different diameter jets and voltage control on the metal capillary.

The surface sensitivity of the TIY method was tested with thiocyanate, which has been shown to be enhanced in concentration at the liquid water surface. After normalizing to the potassium peak intensity, the TIY carbon resonance intensity relative to the corresponding TEY signal was used as a potential measure of surface sensitivity. This "TIY/TEY" probe can differentiate thiocyanate from relatively surface-depleted acetate and carbonate, but no concentration dependence was observed, possibly due to a high contribution of x-ray induced electron stimulated desorption of ions. Preliminary experiments examining the potential surface sensitivity of upstream detection have shown enhanced carbon signal relative to TEY detection for KSCN solutions; however, further tests for concentration dependence and comparison with other salts are necessary before making a definitive conclusion.

4.5 References

[1] Wilson, K. R.; Cavalleri, M.; Rude, B. S.; Schaller, R. D.; Nilsson, A.; Pettersson, L. G. M.; Goldman, N.; Catalano, T.; Bozek, J. D.; Saykally, R. J. *J. Phys.: Condens. Matter* **2002**, *14*, L221-L226.

[2] Cappa, C. D.; Smith, J. D.; Wilson, K. R.; Saykally, R. J. *J. Phys.: Condens. Matter* **2008**, *20*, 205105.

[3] Stöhr, J. *NEXAFS Spectroscopy*; Springer: Berlin, 1992.

[4] Wilson, K. R.; Schaller, R. D.; Co, D. T.; Saykally, R. J.; Rude, B. S.; Catalano, T.; Bozek, J. D. *J. Chem. Phys.* **2002**, *117*, 7738-7744.

[5] Peterson, P. B.; Saykally, R. J.; Mucha, M.; Jungwirth, P. *J. Phys. Chem. B* **2005**, *109*, 10915-10921.

[6] Wilson, K. R.; Rude, B. S.; Smith, J.; Cappa, C. D.; Co, D. T.; Schaller, R. D.; Larsson, M.; Catalano, T.; Saykally, R. J. *Rev. Sci. Instrum.* **2004**, *75*, 725-736.

[7] Bianconi, A. *Appl. Surf. Sci.* **1980**, *6*, 392.

[8] Seiger, M. T.; Simpson, W. C.; Orlando, T. M. *Phys. Rev.* **1997**, *56*, 4925.

[9] Tolk, M.; Traum, M.; Tully, J. C.; Madley, T. E. *Desorption Induced by Electronic Transitions DIET-I*; Springer: Berlin, 1982.

[10] England, A. H.; Duffin, A. M.; Schwartz, C. P.; Uejio, J. S.; Prendergast, D.; Saykally, R. J. *Chem. Phys. Letters* **2011**, *514*, 187-195.

[11] Pegram, L. M.; Record, M. T. Jr. *J. Phys. Chem. B* **2007**, *111*, 5411-5417

[12] Pegram, L. M.; Record, M. T. Jr. *Chem. Phys. Lett.* **2008**, *467*, 1-8